TECHNISCHE UNIVERSITÄT WIEN

Dissertation

Modeling and simulation of microstructure evolution in low-alloy TRIP-Steels

Submitted for the degree “Doktor der technischen Wissenschaften“ under direction of

Univ.Prof. Dipl.-Ing. Dr.techn. E. Kozeschnik

E308

Institute for Materials Science and Technology

Submitted at TU Wien

Faculty for Mechanical and Industrial Engineering

by

Philipp Retzl

Matr. Nr. 1125432

St. Pöltnerstraße 67

3040 Neulengbach

Austria

Vienna, 28th of February 2025

_____

Personal Signature

This dissertation has been assessed by

Prof. Francisca Caballero

Prof. Ronald Schnitzer

Declaration

I declare in lieu of oath, that I wrote this thesis and performed the associated research myself, using only literature cited in this volume.

(Philipp Retzl)

Vienna, 28th of February 2025

Acknowledgment

First and foremost, I would like to express my deepest gratitude to Prof. Kozeschnik for giving me the opportunity to expand my knowledge in the field of materials science and technology. His guidance, invaluable insights, and unwavering support have played a crucial role in my development as a researcher. I am especially grateful for his patience, constructive feedback, and willingness to always keep his door open whenever I needed advice. Beyond his academic mentorship, I deeply appreciate his kindness and encouragement during difficult moments, always offering reassurance and support when I needed it most.

I would also like to extend my sincere appreciation to my colleagues and fellow researchers a tE308. The stimulating discussions, exchange of ideas, and collaborative spirit made the research process both enriching and enjoyable. Their support and camaraderie created an inspiring environment that helped me navigate challenges and stay motivated.

Beyond everything else, I am deeply grateful to my parents, my sister, and Karina for their unwavering love, patience, and encouragement. Their belief in me has been a constant source of strength, motivating me to persevere through even the most challenging moments. From their emotional support to their unconditional love, they have been my pillars throughout my academic journey

This accomplishment would not have been possible without the support of all these incredible individuals. To each and every one of you: **Thank you!**

Abstract

This thesis employs computational methods to investigate the microstructure evolution of low-alloy TRIP steels, utilizing the MatCalc framework. MatCalc applies mean-field approaches, classical nucleation theory, and predictive interfacial energy models to describe the evolution of precipitates in metallic materials. Additionally, it offers various models to simulate the evolution of microstructural features, such as dislocation density and grain size. The present thesis proposes a method for applying these models to the complex multiphase microstructure of TRIP steels to simulate precipitation kinetics and simultaneous long-range diffusion. The primary focus of this thesis is on the bainitic microstructure, which, in its carbide-free form, provides TRIP-steels with their characteristic combination of high strength and toughness. Despite extensive research, the mechanisms governing bainite formation remain a subject of debate. By combining several modeling and simulation approaches, this study examines some key mechanisms that drive the formation of this microstructure. Special attention is given to the partitioning of carbon from bainite subunits into the surrounding austenite. The simulation results offer valuable insights into the formation and characteristics of the film-like austenite that exists between individual bainite subunits within a sheaf. Furthermore, the study revisits the formation of lower and upper bainite, proposing a potentially new interpretation of the formation mechanism based on computational findings.

Kurzfassung

In dieser Arbeit wird die Mikrostrukturentwicklung von niedriglegierten TRIP-Stählen mithilfe von computergestützten Berechnungsverfahren untersucht, wobei das MatCalc 6-Framework zum Einsatz kommt. MatCalc wendet „mean-field“-Ansätze, die klassische Keimbildungstheorie und prädiktive Grenzflächenenergiemodelle an, um die Entwicklung von Ausscheidungen in metallischen Werkstoffen zu beschreiben. Darüber hinaus bietet es verschiedene Modelle zur Simulation der Entwicklung mikrostruktureller Merkmale, wie Versetzungsdichte und Korngröße. In der vorliegenden Arbeit wird eine Methode zur Anwendung dieser Modelle auf die komplexe mehrphasige Mikrostruktur von TRIP-Stählen zur Simulation der Ausscheidungskinetik vorgestellt. Der Schwerpunkt dieser Arbeit liegt auf der bainitischen Mikrostruktur, die in ihrer karbidfreien Form TRIP-Stählen ihre charakteristische Kombination aus hoher Festigkeit und Zähigkeit verleiht. Trotz umfangreicher Forschung sind die Mechanismen, die die Bainitbildung steuern, nach wie vor zum Teil umstritten. Durch die Kombination mehrerer Modellierungs- und Simulationsansätze untersucht diese Studie die Schlüsselmechanismen, die die Bildung dieser Mikrostruktur antreiben. Besonderes Augenmerk wird auf die Umverteilung von Kohlenstoff aus ferritischen Bainit-Plättchen in den umgebenden Austenit gelegt. Die Simulationsergebnisse bieten wertvolle Einblicke in die Bildung und die Eigenschaften des filmartigen Austenits, der zwischen einzelnen Plättchens innerhalb eines Bainit-Bündels vorhanden ist. Darüber hinaus befasst sich die Studie mit der Bildung von unterem und oberem Bainit und schlägt auf der Grundlage von Simulationsergebnissen eine neue Interpretationsmöglichkeit für den Bildungsmechanismus vor.

Preface

This thesis is submitted in compliance with the requirements for the degree of doctor of technical sciences at the Vienna University of Technology. The doctoral work has been carried out at the Faculty of Mechanical and Industrial Engineering, Institute of Materials Science and Technology, Vienna, Austria. The thesis is divided into two sections. In section A, an introduction to the field of microstructure evolution in TRIP steels and the employed modeling approaches is given. In Section B, the concepts discussed in Section A are reported in detail in the form of three publications, which are:

1. P. Retzl, W. Mayer, D. Krizan, and E. Kozeschnik, Simulation of Carbo-Nitride Precipitation in the Multi-Phase Microstructure of Micro-Alloyed Transformation-Induced Plasticity Steel, *steel Res. Int.*, 92, (2021) 2000197.
2. P. Retzl and E. Kozeschnik, The tale of upper and lower bainite: A computational analysis of concurrent C-diffusion and precipitation, *Scr. Mater.*, 248, (2023), 116146.
3. P. Retzl, E. Kozeschnik, The tale of upper and lower bainite: A computational analysis of concurrent C-diffusion and precipitation. *Scr. Mater.* 248, (2024), 116146.

Apart from these first-author publications, the following papers were published in collaboration with colleagues:

- A. Jacob, B. Schuscha, P. Retzl, Y. V. Shan, and E. Kozeschnik, Thermodynamic Prediction of the Impact of Carbon on Bainite Formation, Including the BCT Transformation, J. Phase Equilibria Diffus., 44, (2023), 729–737.

- A. Jacob, E. Povoden-Karadeniz, P. Retzl, and E. Kozeschnik, Reassessment of low-temperature Gibbs energies of BCC and FCC in steel for T0-temperature evaluation, Calphad Comput. Coupling Phase Diagrams Thermochem., 81, (2023), 102531.

- W. Wei, P. Retzl, E. Kozeschnik, and Erwin Povoden-Karadeniz, A semi-physical α-β model on bainite transformation kinetics and carbon partitioning, Acta Mater., 207, (2021), 116701.

Moreover, the work that was performed throughout the years has been presented at conferences:

- P. Retzl, E. Kozeschnik, Simulation study of carbide formation and dissolution in upper/lower bainite, oral presentation at “THERMEC ’2023”, Vienna, Austria, 07.2023
- A. Jacob, P. Retzl, E. Kozeschnik, Reassessment of low-temperature Gibbs energies for T0-temperature evaluation, Poster Presentation at “Calphad XLIX International Conference on Computer Coupling of Phase Diagrams and Thermochemistry”, Stockholm, Sweden., 05.2022
- P. Retzl, E. Kozeschnik, Modelling the influence of initial grain size and particle stimulated nucleation on recrystallization kinetics in hot deformed steel, oral presentation at “Euromat 2019”, Stockholm, Sweden, 09.2019

“The purpose of computing is insight,

not numbers.”

-Richard Wesley Hamming

Table of Contents

Section A

1. Introduction

Ever since mankind discovered metallic materials there has been a strong demand to improve the properties of materials. This is especially true for iron carbon alloys called steel. Due to the complex nature of the phase transformations occurring during the production and heat treatments of steel, there was plenty of room for improvement over thousands of years. These finally lead to modern steel products, which often exhibit a carefully adjusted microstructure consisting of a mixture of different phases on length scales spanning over several orders of magnitude. One group of steels that is able to combine high strength and ductility due to its complex microstructure is so-called transformation-induced plasticity (TRIP) steel, which will be investigated in this thesis. It gets its excellent mechanical properties from the deformation-induced transformation of austenite into martensite. This effect is designated as TRIP effect [1]–[5].

Although we have come a long way to achieve this sophisticated level of steel production, there are still a lot of unanswered questions. Often, the exact mechanisms of phase transformations or how and why they are influenced by temperature and chemical composition are still not understood to a degree that allows for meaningful predictions. To further improve the properties of steel and the efficiency of production plants, more insight and better descriptions in the form of suitable modeling approaches are crucial.

One of the least understood phenomena in modern steelmaking is the bainite transformation. During bainite formation, austenite decomposes into a mixture of ferritic platelets and carbides. However, adding sufficient amounts of carbide-suppressing elements like Si or Al can effectively inhibit the process of carbide formation. As a result, a certain fraction of austenite remains after the bainite transformation is complete. The corresponding microstructure is called carbide-free bainite and is often employed in TRIP steels to obtain sufficiently stabilized austenite for the TRIP effect.

While bainite was already discovered in 1930 by Davenport and Bain, there is still an ongoing debate about the mechanisms that govern its formation [6]–[8]. Modern TRIP steels employ advanced alloying concepts where the mechanical properties of the multi-phase microstructure are further enhanced by the addition of micro-alloying elements, which lead to precipitation strengthening and grain refinement [5]. In order to get more insight and a

better understanding of the complex interplay of phase transformations, carbon partitioning during bainite formation, and precipitation kinetics in TRIP steels, this thesis will present simulation and modeling approaches that are capable of shedding some light on the aforementioned topics. It is hoped that this will be a small step toward computational methods that can help improve the properties and production routes of steel.

The following section gives an overview of TRIP steels, a detailed description of bainitic microstructures and the applied simulation methods, and a short description of some examples that were published in the papers collected in section B.

2. Theoretical Background

This work focuses on the description of complex microstructures present in TRIP steels with the help of mean-field or finite difference scheme models. In order to do sound and meaningful simulations, it is important to understand the subject of the calculations, in this case, TRIP steels, as well as the applied models. Only by knowing the details of the described microstructure and the underlying assumptions of the computational models is it possible to understand the predictive power, potential future applications, and the limitations of the simulations. Therefore, in this chapter, a short introduction to TRIP steels and bainitic microstructures, which are often required for the TRIP-effect, is given. Afterwards, an overview of the applied simulation methods is provided, which are described in detail in the scientific papers in "Section B."

2.1 TRIP steel

Transformation induced plasticity (=TRIP) steels are defined by the transformation of retained austenite to martensite during plastic deformation. Since martensite has higher strength than austenite and this transformation takes first place in regions of high strain, it can effectively shift deformation to other not yet transformed regions of the sample. This mechanism results in a stabilization and delay of necking and enables TRIP steel to simultaneously provide relatively high strength and ductility. [1][9][10][11]

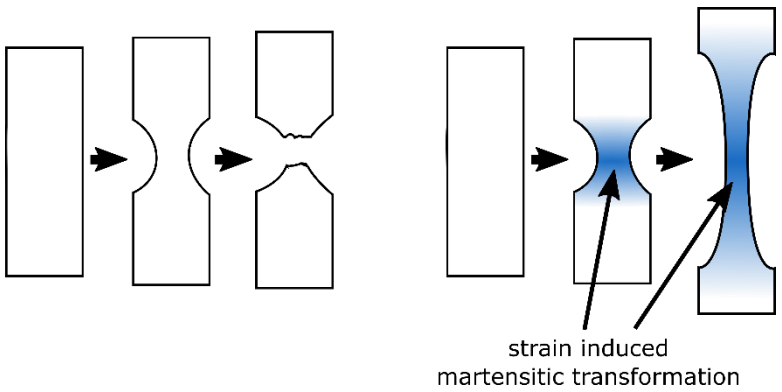

a) Standard - Steel b) TRIP - Steel

Figure 1: Illustration of the different deformation behavior of a) a steel without TRIP effect and b) a sample with TRIP effect

To enable the TRIP effect, a certain amount of austenite must be enriched with carbon to such an extent that it is stabilized down to room temperature. This means that its martensite start

temperature should be low enough to guarantee that a sufficient amount of austenite remains after final cooling. There exist empirical equations to describe how alloying elements and especially carbon influence the martensite start temperature. Another possible way to calculate the martensite start temperature depending on composition is the so called T_0 concept. T_0 represents the specific temperature at which the parent phase (austenite) and the product phase (ferrite) have the same free energy while maintaining an identical chemical composition. As a result, a phase transformation without element partitioning can only take place below this temperature. The transformation from austenite to ferrite occurs through shear deformation and a change in molar volume, requiring a certain amount of mechanical energy to initiate the process. This additional mechanical energy is often chosen as 400 J/mol when calculating the bainite start temperature and between 1200 and 1700 J/mol for martensite start temperatures [12]. Figure 2 shows a comparison of empirical equations from different references and the T_0 approach.

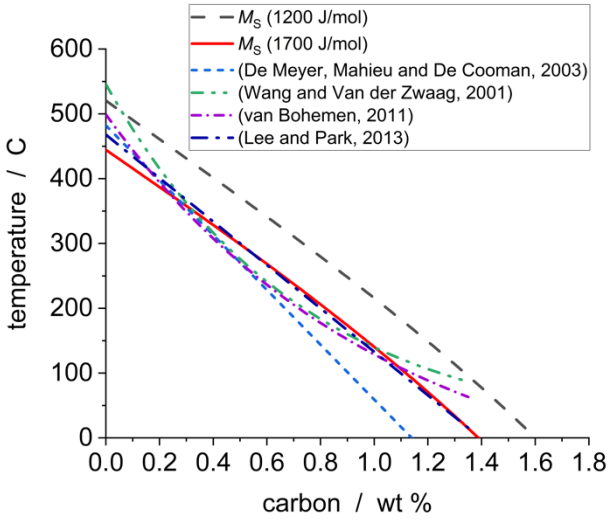

Figure 2: Comparison of M_S-temperatures calculated via the T_0-concept and empirical equations from literature (Composition: 1.5 wt% Si, 1.5 wt% Mn, balance Fe). The grain size for the equation from Lee and Park, 2013, is chosen as 50 µm; Empirical equations from references [13]–[16]**; plot from Paper II** [12]

With a given martensite start temperature M_S and suitable parametrisation, the Koistinen-Marburger equation can be used to describe the remaining austenite fraction at any given temperature T_c below the martensite start temperature. It is written as

$$V_y = \exp\big(-k \cdot (M_S - T_c)\big), \tag{1}$$

with V_y being the volume fraction of austenite, T_c the current temperature and k being a fitting parameter [17].

For steels with a typical carbon content for low alloyed TRIP steels of approximately 0.1 to 0.3 weight-percent, there are two important steps in the heat treatment to enrich the austenite

sufficiently with carbon. In the first step, a certain amount of equiaxed ferrite is formed to increase the carbon content in the remaining austenite to around 0.4 weight-percent. This step can either be realized by intercritical annealing in the two-phase region to transform a ferritic/pearlitic microstructure into an austenititic/ferritic one, if the steel was already cooled down to room temperature, for example during cold-rolling. Or this microstructure can be obtained by directly cooling to the two-phase region after hot-rolling in the austenitic region and holding there for long enough time to obtain the desired amount of ferrite.

For both routes, the final production step is the same. The steel is cooled to a temperature where bainite transformation can occur. Often, the sample is held isothermally at a certain temperature to obtain mechanical properties optimized for its application, but it is also possible and sometimes necessary in industrial applications to continuously cool through the temperature region where bainite forms. The exact temperature path during the bainite transformation has a strong impact on the properties of the final product and, therefore, detailed knowledge of the processes occurring during heat treatment is crucial for further optimizations or to enable the production of TRIP steels on an industrial scale where restrictions concerning cooling rates, holding times or temperature homogeneity across the sample may apply.

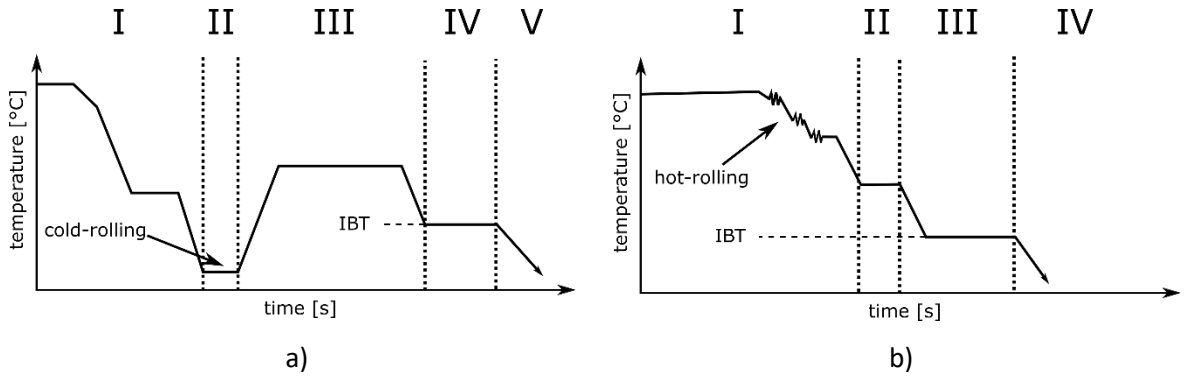

Figure 3: Two typical processing routes for TRIP steels a) cold-rolled route: Area I: casting and cooling to RT to obtain a ferritic/pearlitic microstructure; Area II: cold rolling; Area III: intercritical annealing to obtain a mixture of ferrite and austenite with desired carbon content in austenite; Area IV: Isothermal bainite transformation (=IBT) to produce bainite and austenite with sufficient carbon content to be stable down to RT; Area V: final cooling to RT, some formation of martensite may occur b) hot-rolled route: Area I: casting and hot-rolling; Area II: short isothermal holding to obtain an austenitic/ferritic microstructure with desired carbon content in austenite; Area III: Isothermal bainite transformation (=IBT) to produce bainite and austenite with sufficient carbon content to be stable down to RT; Area IV: final cooling to RT, some formation of martensite may occur

Careful composition selection is crucial for the production of TRIP steel. Besides carbon, the main alloying elements for this type of steel are Mn, Si and Al. Mn is necessary to slow down the formation of pearlite during the cooling to the isothermal bainite transformation (IBT) temperature. Si and Al are crucial to suppress carbide formation during the bainite transformation to ensure that carbide

free bainite forms. Furthermore, the addition of micro-alloying elements such as Ti, Nb and V helps to reduce the grain size during hot-rolling processes, which in turn influences the kinetics of the ferrite and bainite transformations. These precipitates can also contribute to the strength of the final product via precipitation hardening. The evolution of Nb and V carbo-nitrides is simulated and discussed for a cold-rolled TRIP Steel in detail in Paper I of section B. A detailed description of the effects of these and other alloying elements for the production of TRIP steels can be found in chapter 8 of Reference [18].

Another key aspect of TRIP steel production is the choice of a suitable temperature control for the bainite transformation. The transformation temperature has a major impact on the emerging bainitic microstructure. In particular, the amount and geometry of retained austenite, which is critical to the TRIP effect, is controlled by temperature. In most cases, a temperature in the range of 300 to 500 °C and holding times sufficiently long to finish the transformation are chosen. The exact thermomechanical treatment heavily depends on the alloying concept, desired mechanical properties, and restrictions concerning the industrial production process. In order to better understand the pivotal bainitic microstructure, which is not yet fully comprehended in terms of the microstructural mechanisms behind its formation, the next chapter provides an overview of the key aspects of bainite.

2.2 Bainite

Bainite is a microstructure in steel that consists of needle- or plate-like ferritic parts that are called subunits. Subunits nucleate either at grain boundaries or autocatalytically at other subunits. A conglomerate of subunits with the same orientation is called a bainite sheaf. After or during the formation of these subunits, carbon is partitioned into the surrounding austenite. There, either carbides form, which would result in “classic” bainite, or the austenite remains stable because it is highly enriched in carbon and carbide formation is suppressed by additions of Si or Al. The latter microstructure is denoted as carbide-free bainite. Austenite that is located between subunits of one sheaf often has the morphology of a thin film and is, therefore, referred to as film-like austenite, whereas larger untransformed areas between separate sheaves are denoted as blocky austenite. Figure 4 illustrates this microstructure schematically. The carbon content and morphology of the different austenite areas in this microstructure govern the TRIP-effect described in Chapter “2.1 TRIP steel”. Martensite, which forms early on from blocky retained austenite under strain, can negatively impact mechanical properties. In contrast, films of retained austenite, stabilized by higher carbon content and geometry, can enhance toughness through a more pronounced TRIP effect [19]–[24]. Since these film-like retained austenite features are crucial in many TRIP steels, understanding how temperature and composition affect them is vital.

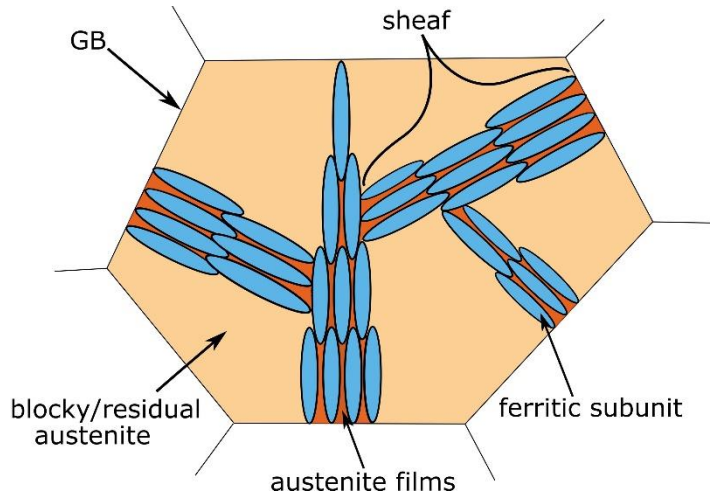

Figure 4: Schematic illustration of a carbide-free bainitic microstructure consisting of ferritic subunits, which build up sheaves, film-like austenite, and areas of blocky/residual (=untransformed) austenite. Size scale is not accurate since austenite films are often some orders of magnitude smaller than blocky austenite areas. GB denotes austenite grain boundaries. [12]

Although extensive research has been conducted in the field of bainitic microstructures in recent decades, some mechanisms that lead to its formation are still controversially discussed. Especially the question of whether the growth of the subunits is governed by a displacive or diffusive mechanism is still a topic of ongoing debate [8][7][25]. For the modeling and simulation approaches

in this work, a displacive mechanism in accordance with the concept of bainite formation as described in Ref. [26] is assumed.

In addition to bainite with carbides between subunits and carbide-free bainite, there is another important distinction between bainitic microstructures, which is determined by the existence of carbides within the ferritic subunits. According to the assumption that subunits grow via a displacive mechanism, i.e., with the speed of sound, they are initially supersaturated in carbon due to the significantly lower solubility of carbon in ferrite compared to austenite [1]. If this excess carbon can diffuse into the surrounding austenite before carbides form within the ferritic subunits, the resulting microstructure is classified as upper bainite. In contrast, if carbide precipitates form within the ferrite, the microstructure is termed lower bainite [27][26][28][7][29]. On further heat treatment, carbon, which is not bound in the form of carbides within the subunits, will eventually partition into the surrounding austenite. If carbide formation in austenite is suppressed, the transformation is finished at this point, and the final microstructure is “carbide-free” bainite. Otherwise, carbides form between the subunits, leading to a classic bainitic microstructure.

Figure 5 illustrates the described steps that lead to one of the two microstructures. In the case of carbide-free bainite, the last step is sufficiently suppressed and, therefore, does not occur in timespans usually applied for the production of TRIP-assisted steels. The competition between carbon long-range diffusion and carbide precipitation, which controls the observed microstructure, is investigated with computational methods in Paper III of section B [30].

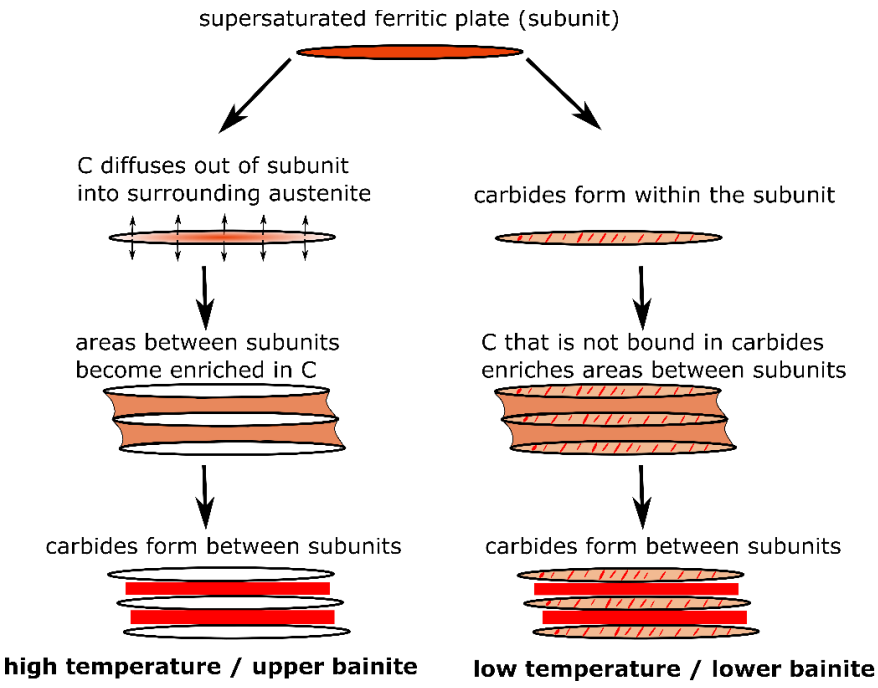

Figure 5: Schematic illustration of the microstructural steps that lead to the formation of either upper or lower bainite. Last step is suppressed in carbide-free bainite.

3. Simulation

This section gives an overview of the applied simulation and modeling methods. All simulations were carried out with the thermokinetic simulation package MatCalc [31]. The specific version of the software that was employed is reported in the individual papers in section B.

The simulation studies of this thesis focus on two microstructural phenomena that play a major role during the production of TRIP steels. One is precipitation kinetics and the other the long-range diffusion of carbon in bainite. These two aspects are briefly described in the next two chapters.

3.1 Precipitation kinetics

Precipitation kinetic simulations in MatCalc rely on a mean-field approach. A crucial part of every simulation approach for the evolution of precipitates is the nucleation model. MatCalc utilizes the classical nucleation theory (=CNT) approach. For a nucleation event to happen, there needs to be a sufficiently large driving force to compensate for the additional interface that inevitably has to be formed between the precipitate and the parent matrix. This fundamental condition can be described by the equation,

$$\Delta G_{\mathrm{nucl}} = \frac{4}{3}\pi\rho^3.\Delta G_{\mathrm{vol}} + 4\pi\rho^2.\Delta G_{\mathrm{surf}} \tag{2}$$

with , ΔG_{nucl} being the free energy of nucleus formation, ΔG_{vol} the specific volume free energy change, ΔG_{surf} the interfacial energy and ρ the radius of the nucleus. If the derivative is formed and set to zero, the critical radius r^* and the critical nucleation energy G^* are obtained as,

$$r^* = -\frac{2\Delta G_{\mathrm{surf}}}{\Delta G_{\mathrm{vol}}}, \tag{3}$$

and

$$G^* = \frac{16\pi}{3}\frac{(\Delta G_{\mathrm{surf}})^3}{(\Delta G_{\mathrm{vol}})^2}. \tag{4}$$

With these quantities on hand, the steady state nucleation rate J_{ss} can be calculated by the relation,

$$J_{\mathrm{ss}} = NZ\beta^* \exp\left(-\frac{G^*}{k_{\mathrm{b}}T}\right). \tag{5}$$

In these equations, N is the number of potential nucleation sites, Z is the Zeldovich factor, $\beta^*$is the atomic attachment rate, k_b is the Boltzmann constant, and T is the absolute temperature in Kelvin. To calculate the interface energies for this approach, the generalized nearest-neighbor broken-bond model [32][33] is used.

To describe the growth of the precipitates once they nucleated, MatCalc uses an approach developed by Kozeschnik et al. [34] based on the "Thermodynamic Extremal Principle". Details of the application of this approach for the growth of precipitates in a multicomponent environment can be found in the references [35]–[38].

Time integration of the applied equations is achieved using the Kampmann-Wagner approach. In this approach, the precipitation distribution is divided into discrete size classes for precipitates of identical radius and chemical composition. The comprehensive mathematical description and detailed analysis of the mean-field modeling approach outlined above can be found in the work of Kozeschnik et al. [36].

To apply the methodology summarized above, a crucial input is thermodynamic data about the investigated system. Thermodynamic calculations in MatCalc employ the Calphad (Calculation of Phase Diagrams) approach [39], which assumes that phase boundary locations result from stability competition between two or more phases. Initially, thermodynamic models for all constituent unary and binary systems are derived, with model types selected to match the physical and thermodynamic properties of the phases. The Gibbs energy of a phase in a binary system can be expressed by:

$$G_\mathrm{m}^\Phi = \sum_{i=\mathrm{A,B}} x_i G_i^{\Phi,0} + RT \sum_{i=\mathrm{A,B}} x_i \, ln x_i + \sum_v x_\mathrm{A} x_\mathrm{B} \, L_v \, (x_\mathrm{A} - x_\mathrm{B})^v + G_\mathrm{EX}^\mathrm{magn} + G_\mathrm{EX}^\mathrm{SRO} + \cdots . \quad (6)$$

The first term on the right-hand side of the equation represents the reference state, with x_i being the mole fraction of component i, and $G_i^{\Phi,0}$, the Gibbs energy of pure component i with structure Φ. The second term is the ideal mixing term, and the third one is the excess Gibbs energy of mixing, with L_v being the interaction coefficients and v the power of the polynomial series. These polynomials are called Redlich-Kister polynomials and are a practical way to describe the interactions in thermodynamic systems. Generally, these model parameters are optimized to best fit the available experimental data. Additionally other excess energy terms can be considered, for example contributions from magnetism $G_\mathrm{EX}^\mathrm{magn}$ and short range ordering $G_\mathrm{EX}^\mathrm{SRO}$.

Ordered intermetallic phases are described by different sublattice models, such as the compound energy model and the bond energy model. These models express the Gibbs energy as a function of

sublattice species concentrations and temperature. The Gibbs energy of a binary intermetallic phase described by a two-sublattice compound energy model, $(A,B)_{\mathrm{p}}:(A,B)_{\mathrm{q}}$, can be written as:

$$\begin{aligned} G_{\mathrm{m}}^{\Phi} = & \sum_{i=\mathrm{A,B}} \sum_{j=\mathrm{A,B}} y_i^I y_j^{II} G_{i:j}^{\Phi} \\ & + RT \left(\frac{p}{p+q} \sum_{i=\mathrm{A,B}} y_i^I \ln y_i^I + \frac{q}{p+q} \sum_{i=\mathrm{A,B}} y_i^{II} \ln y_i^{II} \right) \\ & + \sum_{j=\mathrm{A,B}} y_{\mathrm{A}}^I y_{\mathrm{B}}^I y_j^{II} \left(y_{\mathrm{A}}^I - y_{\mathrm{B}}^I \right)^v L_{\mathrm{A,B}:j}^v \\ & + \sum_{j=\mathrm{A,B}} y_i^I y_{\mathrm{A}}^{II} y_{\mathrm{B}}^{II} \left(y_{\mathrm{A}}^{II} - y_{\mathrm{B}}^{II} \right)^v L_{i:\mathrm{A,B}}^v + y_{\mathrm{A}}^I y_{\mathrm{B}}^I y_{\mathrm{A}}^{II} y_{\mathrm{B}}^{II} L_{\mathrm{A,B:A,B}} + G_{\mathrm{EX}}^{\mathrm{magn}} + G_{\mathrm{EX}}^{\mathrm{SRO}} + \cdots . \end{aligned} \tag{7}$$

In this equation, y_i^I and y_i^{II} represent the species concentrations of component i in the sublattices I and II. The first term on the right-hand side denotes the reference state, comprising the mechanical mixture of the pure compounds A, $A_{\mathrm{p}}B_{\mathrm{q}}$, $B_{\mathrm{p}}A_{\mathrm{q}}$, and B. $G_{i:j}^{\Phi}$ is the Gibbs energy of the stoichiometric compound $i_{\mathrm{p}}j_{\mathrm{q}}$ with the structure Φ. The values of $G_{i:j}^{\Phi}$ can either be determined by experiment or by "ab initio" simulations.

Once thermodynamic descriptions for all constituent binaries are established, preliminary descriptions for ternaries can be obtained by extrapolating the binary model parameters. Ternary interaction model parameters refine the description of ternary systems if reliable experimental data is available. The same strategy can be extended to multi-component systems.

3.2 Cell diffusion

To simulate the long-range diffusion of carbon within bainitic microstructures with simultaneous precipitation of carbides, the cell simulation module of MatCalc was employed. It utilizes a finite differences scheme to calculate transient multi-component diffusion profiles [40]. A significant benefit of this numerical cell diffusion approach, compared to analytical methods, is its ability to determine C diffusivity in each cell as a function of current chemical composition, dislocation density, and other microstructural properties. This method also allows for the examination of various geometric configurations involving multiple bainitic subunits.

The most significant feature of this simulation approach is the capability to perform a full precipitation kinetics and microstructure evolution calculation for each cell. This makes it possible to examine the concurrent long-range diffusion of C and the precipitation kinetics of carbides within the ferritic platelet. The latter aspect is utilized in Paper III to investigate the formation of upper and lower bainite. Figure 6 illustrates schematically how the diffusion problem is discretized and that each cell is coupled to the MatCalc precipitation kinetics engine.

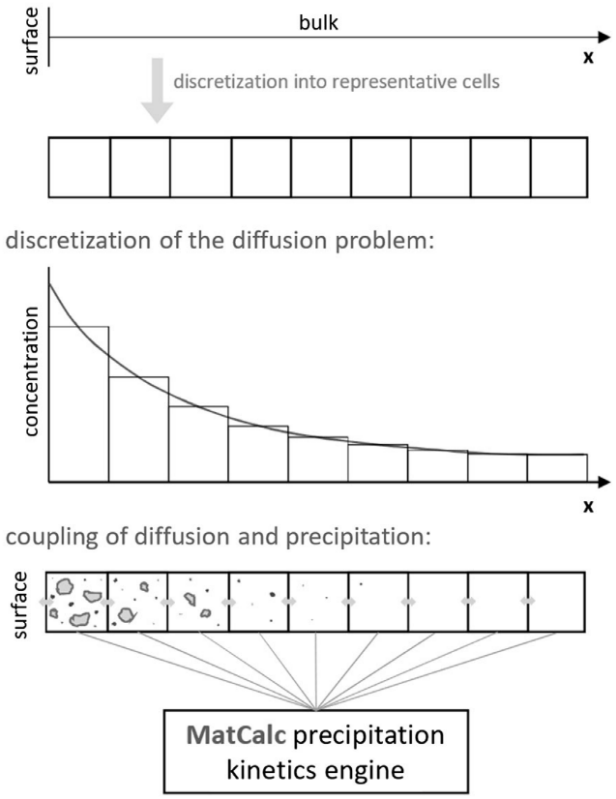

Figure 6: Schematic overview of the discretization steps for the cell-based diffusion model used in MatCalc. [40]

For the simulations in this work, a planar 1-D geometrical setup is applied. The partitioning of carbon between the cells can be calculated according to Fick's law of diffusion as follows:

$$\left[1+\frac{D_{i,i+1}\Delta t}{(\Delta x)^2}+\frac{D_{i,i-1}\Delta t}{(\Delta x)^2}\right]c_i^{t+}-\frac{\Delta t}{(\Delta x)^2}\left[D_{i,i+1}c_{i+1}^{t+}+D_{i,i-1}c_{i-1}^{t+}\right]=c_i^t, \tag{8}$$

where c_i^t is the carbon content of cell i at the time t, and c_i^{t+} at the time $t+\Delta t$. $D_{i,i+1}$ is the mean diffusion coefficient of the cells i and $i+1$ and $D_{i,i-1}$ is the mean diffusion coefficient of the cells i and $i-1$. Therefore, for *N* cells, a linear equations system of *N* equations in *N* variables is obtained, which can be solved numerically.

At phase boundaries, an additional flux J, which is a result of a difference in chemical potentials, must be taken into account. It can be calculated by,

$$J=\frac{Dc}{R_{\mathrm{g}}T}\frac{\partial \mu}{dx}, \tag{9}$$

with D being the diffusion coefficient, c the concentration, x a 1D planar spatial coordinate and $R_{\mathrm{g}}$the gas constant. Accordingly if a phase boundary exists between the cells i and $i+1$, the flux $J_{i,i+1}$ can be written in discretized form as,

$$J_{i,i+1}=-\frac{D_{i,i+1}c_{i,i+1}}{R_{\mathrm{g}}T}\frac{\mu_i-\mu_{i+1}}{|x_i-x_{i+1}|}, \tag{10}$$

where $D_{i,i+1}$ and $c_{i,i+1}$ are the arithmetic mean values of diffusion and carbon concentration of the cells i and $i+1$, $c_{i,i+1}$. Finally the gradient in concentration for cell i can be calculated with

$$\Delta c_i=\frac{J_{i,i+1}A_{i,i+1}}{V_i}\Delta t, \tag{11}$$

with $A_{i,i+1}$ being the area between cells i and $i+1$ and V_i being the volume of cell i. In a 1D simulation, the factor $A_{i,i+1}/V_i$ can be reduced to a division by the thickness of the cell.

The difference in concentration, Δc_i that is caused by the flux $J_{i,i+1}$ is then added to equation 8 on the right-hand side if applicable, i.e., there exists a phase boundary and, therefore, a difference in chemical potential. Diffusion coefficients are calculated for each individual cell according to the standard procedure of MatCalc. A detailed description of this approach and some other use cases of this model can be found in the References [41] and [42].

The impact of dislocation density and other factors that may influence the diffusion coefficients of carbon (C) are discussed in detail in Paper II.

Figure 7 shows an example of the output of this approach from Paper II. It illustrates the evolution of the carbon concentration profile of a 0.4 C - 1.5 Mn - 1.5 Si wt% steel if, at first, one bainite subunit is

present and, at a certain time, a second one is added to investigate the resulting thickness and carbon content of the emerging austenite film.

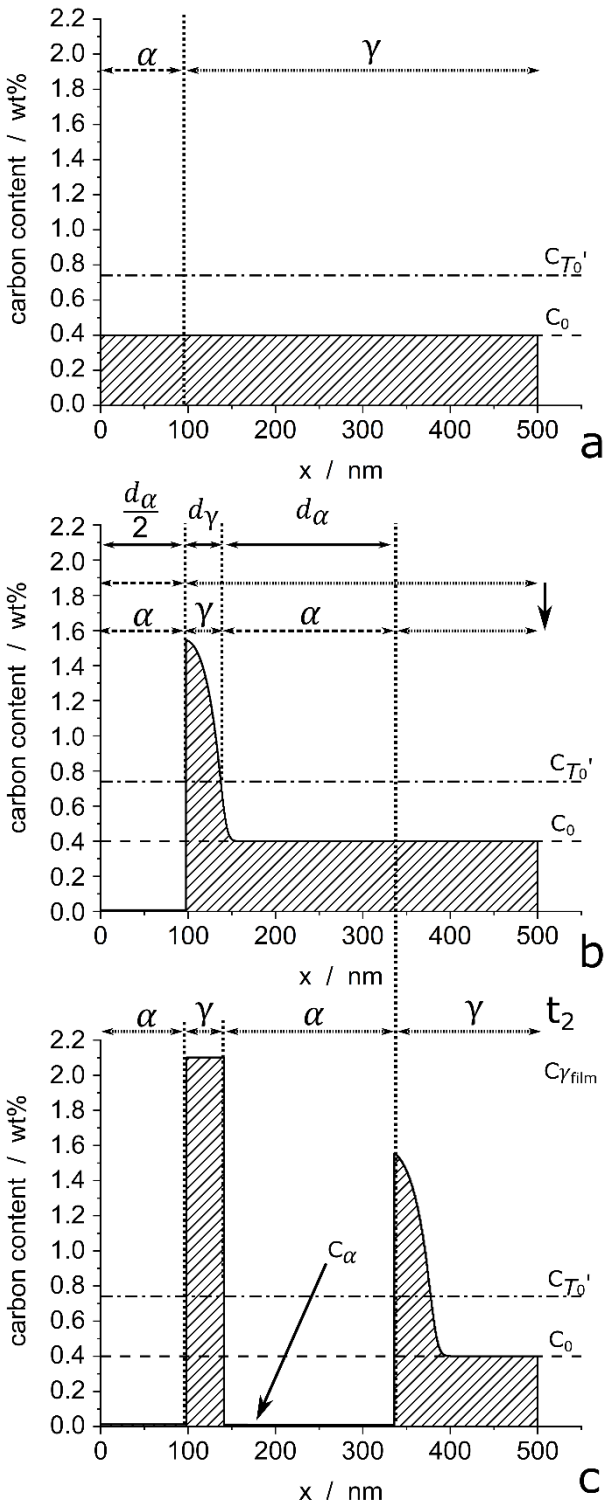

Figure 7: Scheme of the simulation steps for a cell diffusion calculation. a: t_0, initial state with nominal C-content, C_0, in all cells; b: t_1, carbon profile after decarburization of the ferritic bainite platelet (=subunit), another bainite platelet is inserted into the simulation; c: t_2, second bainite subunit has reached its equilibrium C-content; thickness of the austenite film d_γ, thickness of a bainite subunit d_α. C_α is the C-content of the ferritic subunits in equilibrium (~0.02) [12]

As mentioned above, this cell-diffusion approach not only allows to do a full precipitation kinetics simulation for each cell but also to utilize the microstructure models available in MatCalc. One of these models allows to consider the trapping of elements at defects in our simulations. Since a lot of dislocations exist in bainitic microstructures, there are a lot of potential traps for carbon atoms. This effect becomes even more relevant as transformation temperatures decrease and, therefore, has to be taken into account if so called “nano-scale” bainite, which forms at around 200 °C and below [43][44], should be simulated. The same effect is observed in martensite, where up to 0.2 wt% of carbon can be trapped at 200 °C [45]. This was confirmed by X-ray and atom probe measurements [43][46].

The carbon that is trapped at dislocations inside the subunits is unavailable for diffusion into the surrounding austenite and, therefore, this effect can have a big impact on the overall evolution of bainitic microstructures.

To incorporate this effect into the simulation approaches presented in this thesis, the model developed by Svoboda et al. [47][48][49][50] is utilized and will be described briefly in the next section.

The molar concentration c_i of trapped element i on traps k can be expressed by,

$$c_i = c_{\mathrm{L}i} + \sum_k c_{\mathrm{T}ki}, \tag{12}$$

where the indices $\mathrm{L}i$ denote the lattice (free) part of element i, and $\mathrm{T}ki$ the trapped atoms of species i on trap k.

To obtain the fraction of occupancy of all lattice positions $y_{\mathrm{L}i}$ by an element i, the product of the molar concentration c_{Li} and the volume of one mole of lattice positions V_{L} can be calculated with

$$y_{\mathrm{L}i} = c_{\mathrm{L}i} V_{\mathrm{L}}. \tag{13}$$

In a similar manner, the fraction of occupancy of element i on traps k,

$$y_{\mathrm{T}ki} = c_{\mathrm{T}ki} V_{\mathrm{T}k}, \tag{14}$$

is the product of the molar concentration of element i on traps of type k c_{Tki} with the volume of one mole of trap positions $V_{\mathrm{T}k}$.

The inverse molar volume of the system Ω can be derived from mass balance as

$$\frac{1}{\Omega} = \frac{1}{V_{\mathrm{L}}} + \sum_k \frac{1}{V_{\mathrm{T}k}}. \tag{15}$$

The molar volume of trapping sites is given by,

$$V_{\mathrm{T}k} = \frac{1}{Z_k c_k}, \tag{16}$$

where c_k is the molar concentration of trapping sources and Z_k is the coordination number of trap k.

For the case of dislocations, c_k becomes c_{disl} and can be written as,

$$c_{\mathrm{disl}} = \pi \rho a^2, \tag{17}$$

with ρ being the dislocation density and a the dislocation core radius.

Finally, the change in Gibbs Energy due to the trapping of elements i on traps of a certain type k can be calculated by

$$\begin{aligned} G = G_0 + R_{\mathrm{g}}T \Bigg(& \frac{\Omega}{V_{\mathrm{L}}} \left(\sum_i y_{\mathrm{L}i} \ln y_{\mathrm{L}i} + \left(1 - \sum_i y_{\mathrm{L}i}\right) \ln \left(1 - \sum_i y_{\mathrm{L}i}\right) \right) \\ & + \sum_k \frac{\Omega}{V_{\mathrm{T}k}} \left(\sum_i y_{\mathrm{T}ki} \ln y_{\mathrm{L}i} + \left(1 - \sum_i y_{\mathrm{T}ki}\right) \ln \left(1 - \sum_i y_{\mathrm{T}ki}\right) \right) \Bigg) \\ & - \sum_k \sum_i \frac{\Omega}{V_{\mathrm{T}k}} y_{\mathrm{T}ki} \Delta E_{ik}. \end{aligned} \tag{18}$$

To determine the equilibrium state for an element j on a trap l, we set $\dot{G} = 0$ and obtain,

$$\frac{y_{\mathrm{L}j}}{1 - \sum_i y_{\mathrm{L}i}} \frac{1 - \sum_k \sum_i y_{\mathrm{T}ki}}{y_{\mathrm{T}lj}} = \exp\left(\frac{\Delta E_{lj}}{R_{\mathrm{g}}T}\right). \tag{19}$$

The results that can be obtained through the careful combination of the above-described modeling approaches with empirical and experimental input, will be shown in the next chapter.

4. Application/Examples

By combining the models and simulation approaches described in the previous section, simulation studies have been carried out to improve our understanding of carbon partitioning during bainite formation. Some selected examples of these simulations, published in the papers collected in section B, are presented and discussed here.

As already mentioned in Chapter "2.2 Bainite", the properties of the film-like austenite that forms during the bainite formation have a major impact on the mechanical properties of TRIP steels. Therefore, one of the simulation studies focused on investigating how transformation temperature and initial carbon content influence the film thickness and the carbon content of these microstructural features. To achieve this, the cell diffusion approach described in chapter "3.2 Cell diffusion" was utilized.

At the start of each simulation, a number of cells equivalent to half the thickness of a bainite subunit are set to have ferrite as their matrix phase on the left side of the simulation box. The simulation is then run until a certain time, where, based on an empirical approach described in Paper II [12], a second ferritic subunit is inserted into the simulation box. The time when this is done, t_{nsu}, is given by the empirical equation,

$$t_{\mathrm{nsu}} = 23 \exp^{-0.014*T}, \tag{20}$$

where *T* is the temperature in °C. It is inserted at the position where the carbon content in austenite first falls below the value given by the T_0' concept (see chapter 2.1 TRIP steel). Figure 8 shows how this position d_i and, therefore, the resulting film thickness changes depending on the current carbon profile.

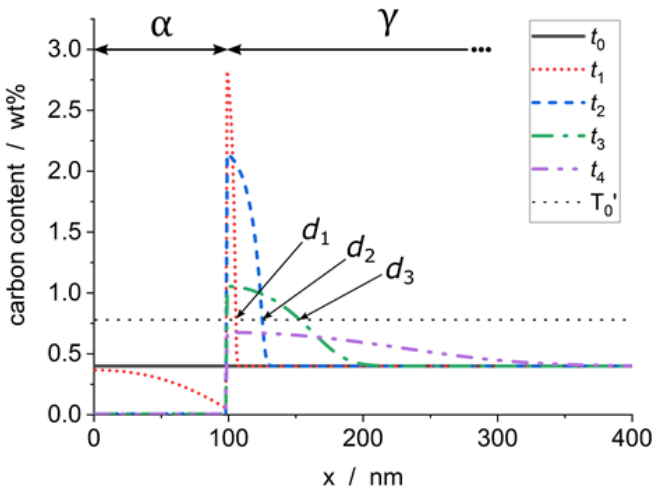

Figure 8: Calculated evolution of C-concentration profiles in the vicinity of a subunit. The locations of the critical carbon content (horizontal dashed line), d_i, correspond to the simulation times, t_i. While the predicted film thickness increases from t_0 to t_3, it decreases afterwards and, eventually, reaches zero again after longer simulation times. [12]

Then, the calculation is continued until the carbon inside the second subunit is fully ejected into its surroundings. An illustration of this procedure is shown in Figure 9. The resulting thickness and carbon content of the film-like austenite for a 1.5 Mn - 1.5 Si wt% steel with either 0.2 or 0.4 wt% of carbon is shown in Figure 9.

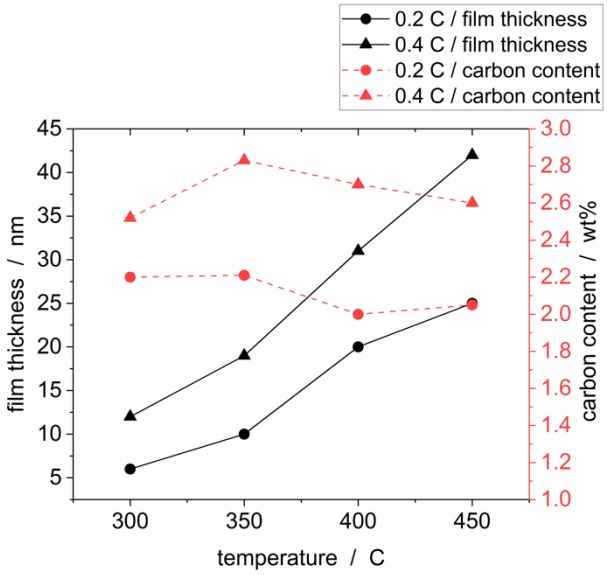

Figure 9: Predicted austenite film thickness and C-concentration within the austenite films for 0.2 wt% and 0.4 wt% matrix carbon concentration, respectively. [12]

For both carbon concentrations, the film thickness increases with increasing temperature. Due to the higher initial carbon content, the films in the alloy with 0.4 wt% carbon are thicker. The carbon

concentration of the austenite films shows a dependence on the initial carbon content but hardly any temperature dependence. It must be mentioned, however, that these concentration values only apply immediately after the nucleation of the adjacent subunits. Depending on the temperature and geometry of the entire bainite bundle, the carbon from the film can diffuse out over time. Therefore, measured values could deviate significantly from the values predicted here, especially at higher bainite transformation temperatures.

The lack of comprehensive data in the existing literature makes it difficult to validate these results. Data from reference [38] indicate a carbon content of approximately 1.8-2.2 wt% in austenite films for an alloy with a composition of 0.39 wt% C, 4.09 wt% Ni and 2.05 wt% Si at a transformation temperature of 400°C. With an initial carbon content of 0.4 wt%, our current model predicts a carbon content of around 2.6 wt% in the films. As mentioned above, our model predicts the carbon content at the moment where the films are first formed, whereas experimental setups measure the carbon concentration in films that have been present for a longer time and have, therefore, already exchanged carbon with the surrounding blocky austenite regions, resulting in slightly lower values compared to our simulation.

This effect should be less relevant at lower temperatures. Therefore, a simulation study at a transformation temperature of 200 °C was conducted. While the aforementioned effect may be less pronounced at this temperature, another effect comes into play that has to be considered. This effect is the trapping of carbon at defects. The high dislocation density within the bainite subunits provides a large number of traps for carbon atoms, which in turn are not available for diffusion. This effect is confirmed by X-ray and atom probe measurements [43], [46]. It is accounted for in the simulations by the trapping model described in chapter “3.2 Cell diffusion”. There are two main input parameters for this model. The coordination number c and the trapping enthalpy ΔE. They are choosen according to Mayer et al. [51] as $\Delta \mathrm{E} = \ 75000 - \ 20 * \mathrm{T}\ [\mathrm{J/mol}]$, and $c = A/T^2$, with the parameter A being 10^6.

In order to be as close as possible to the specific case investigated, the position and thickness of the first subunit in this simulation are approximated from the atom probe measurements in ref. [44]. The position of the second subunit is chosen according to the approach described in this section beforehand, while its thickness is also chosen according to the atom probe measurements from literature. The dislocation density is assumed to be $3 \cdot 10^{15}$ m^{-2}, as measured for this steel in the temperature range of 200 to 350°C by Caballero et al. [52].

Figure 10 shows the resulting carbon profiles from the simulation setup described in the section above. The results without the consideration of trapping (black dashed line) overestimate the

thickness and the carbon concentration in the film-like austenite region between the two subunits. This is due to the very small amount of remaining carbon inside the subunits, which is close to zero. In contrast, both the film thickness and the predicted carbon content of the film are well represented when trapping is taken into account (black line).

At transformation temperatures of 200°C, the formation of lower bainite is expected [27]. This means that carbides are formed in the subunits. As these are carbon sinks, they influence the carbon partitioning process. Extensive TEM (Transmission Electron Microscopy) studies have found no carbides in similar steels, as reported by Caballero and Bhadeshia [43]. Other studies suggest that small amounts of carbides or carbon clusters may be present [52], but in this case, they should have a rather small influence on the overall carbon partitioning and be negligible due to their low phase fraction. It is likely that, in other alloys or with other heat treatments, the influence of carbides may be relevant. In a further simulation study described in paper III, the formation characteristics of lower and upper bainite were investigated. This was done by combining the precipitation kinetics and cell diffusion capabilities of MatCalc, as described earlier in section “3.2 Cell diffusion”.

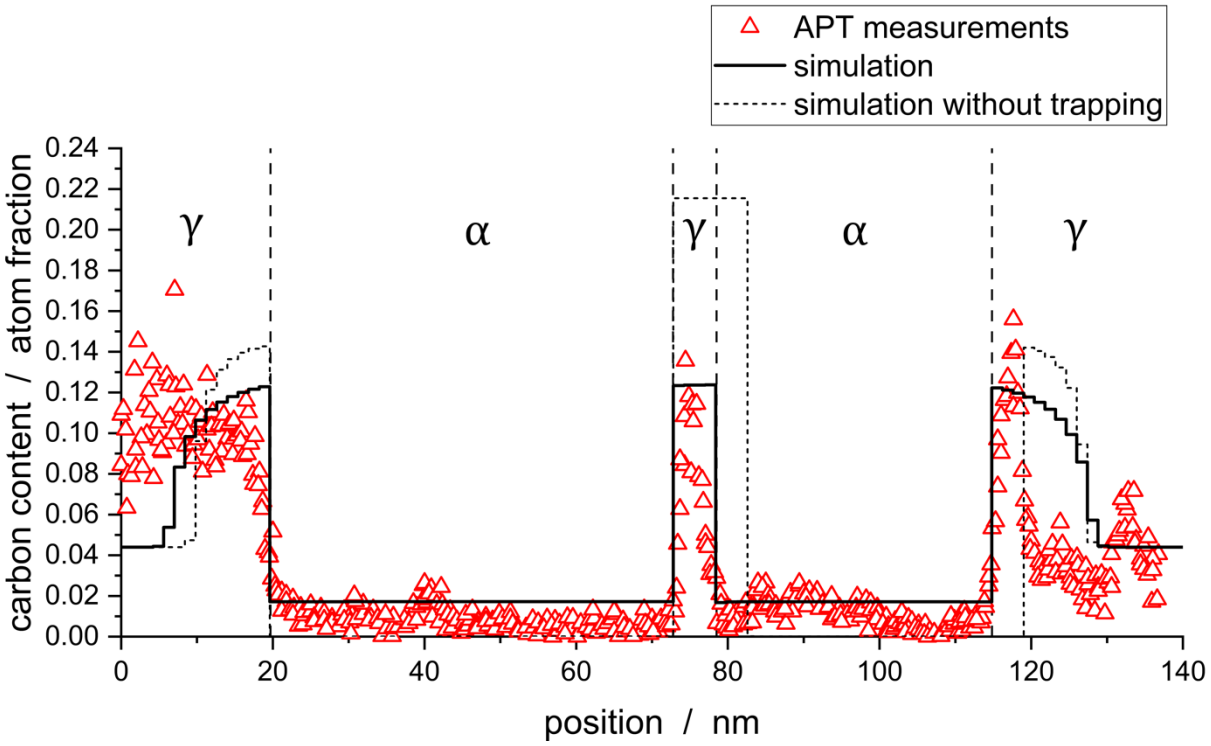

Figure 10: Simulation of bainite formation at 200 °C, with and without trapping taken into account [12]**. APT measurements from ref.** [44]**.**

As shown in Figure 5, the formation of either upper or lower bainite is determined by a competition between carbon diffusion from the ferritic subunit into the surrounding austenite and carbide precipitation within the subunits. Existing models in the literature describing these simultaneous

processes are based on a separate description of carbon repartitioning and precipitation [53][54]. In the approach presented here, a direct coupling of diffusion and precipitation kinetics is used. This is achieved by utilizing the MatCalc ability to directly link a complete precipitation kinetics calculation to each cell in the cell diffusion module. The numerical approach to cell diffusion simulation does not require the same simplifications as an analytical solution and, therefore, allows the dependence of diffusivity on carbon concentration, dislocation density (pipe diffusion), chemical potential and trapping on defects to be taken into account. A detailed description of this approach is reported in Paper III.

The model outlined in the previous section is used to study two alloys containing 0.05 wt% and 0.45 wt% carbon over a temperature range of 300 to 500 °C. The simulations are carried out for durations of up to 3000 seconds. The selected carbon concentrations are chosen based on the expected microstructural outcomes: At high temperatures and low carbon content (0.05 wt%), an upper bainite structure is anticipated, while, at lower temperatures and higher carbon content (0.45 wt%), a lower bainite structure, characterized by carbides within the ferritic subunits, is expected [54].

During the simulation studies, a previously undescribed behavior became apparent. The presence of carbides in the subunits is normally used to distinguish between the two microstructures. However, in our simulations, there was no clear dividing line observable between the upper and lower bainite. Even for a relatively high temperature of 500 °C and 0.05 wt% of carbon, rapid nucleation of carbides was observed. The evacuation of carbon into the surrounding austenite was by orders of magnitude too slow to completely prohibit the formation of cementite (or transition carbide) precipitates due to their high driving force for nucleation in a ferritic matrix. This phenomenon of an initial burst of carbide nucleation was observed for all temperatures and for both investigated alloys. However, after a certain time, the carbon concentration in the subunit decreases to a level where the carbides dissolve again. The carbon finally partitions into the austenite, although with a significant delay because it is temporarily bound in the carbides. The timescale where this happens varies heavily depending on carbon content in the alloy and temperature and ranges from below 0.01 to more than 3000 seconds. The time it takes for the two alloys at different temperatures to reach a maximum phase fraction of carbides and the time necessary for them to dissolve again are summarized in Figure 11.

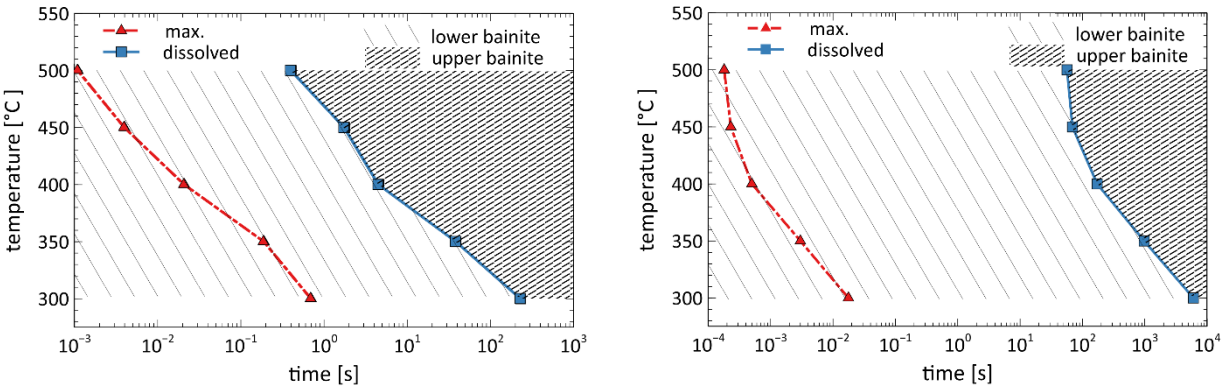

Figure 11: Simulation results for the time until the maximum phase fraction of carbides is observed within the ferritic bainite subunits (red triangles) and time until all carbides are dissolved (blue squares) as a function of temperature for C content of 0.05 wt% (a) and 0,45 wt% (b). Differently, shaded areas indicate if upper or lower bainite will be observed. [30]

These results suggest that there is no sharp boundary between upper and lower bainite. Rather, a characteristic amount of carbides is likely to form in all cases initially within the subunit. Depending on the carbon content and temperature, these carbides will dissolve again. Since this process takes only fractions of a second at low carbon content and high temperatures, and bainite transformations usually require timescales several orders of magnitude longer for complete transformation, only upper bainite is detected in experimental studies. If the dissolution time of the carbides is longer than the transformation time or the holding time at the transformation temperature, lower bainite will be observed. This means that, depending on when an observer looks at the microstructure, either upper or lower bainite is diagnosed. In contrast to Figure 5, which shows the classical evolution of a bainitic microstructure leading to either upper or lower bainite, Figure 12 illustrates the mechanism predicted by our simulations.

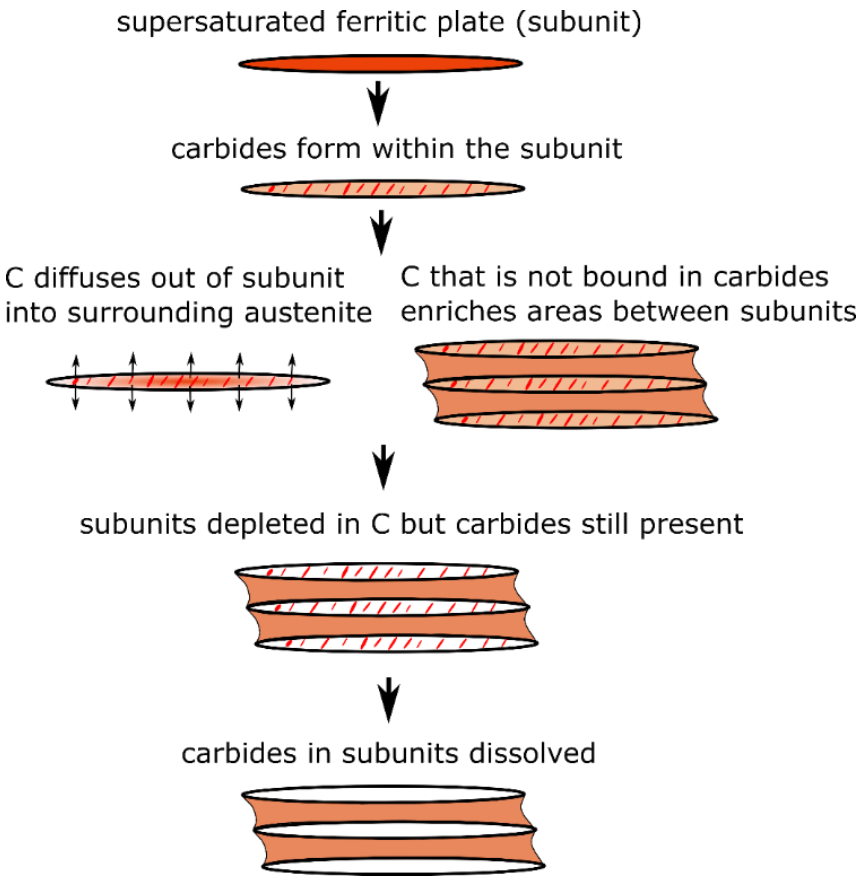

Figure 12: Schematic illustration of the mechanism leading to the formation of upper or lower bainite as suggested by the modeling approach described in Paper III [30].

Observing rapid formation and dissolution of carbides at elevated temperatures is challenging due to the short timescales and small structural dimensions involved. However, under high carbon low temperature conditions, carbide dissolution can be observed if the bainite is tempered for a significant period beyond the required transformation time. According to our simulations, this process would show its onset with the appearance of carbide-free regions at the edges of subunits. An experimental study [29] confirmed carbide-free zones, particularly in subunits located at the periphery of sheaves. This resembles our simulation setup where a single subunit is surrounded by austenite with no neighboring subunits in close proximity. Further experimental evidence is needed to confirm or rule out the suggested mechanism.

5. Summary and Outlook

In this thesis, simulation approaches were developed, which provide insights into the formation and evolution mechanisms of different microstructural aspects of trip steel. For simulations, the MatCalc framework was utilized. This software package employs a variety of (mostly) mean-field models to simulate precipitation kinetics with simultaneous long-range diffusion as well as the evolution of the microstructure of metallic materials.

In Paper I, an efficient and practical approach to calculate the evolution of different precipitates in the complex microstructure of TRIP steels was developed, and the simulations showed good agreement with experimental results. To investigate the complex mechanism of the bainite transformation in TRIP steels, in Papers II & III, the mean-field models of MatCalc were combined with its cell-diffusion module, some semi-empirical relations, as well as experimental input data. Especially, the redistribution behaviour of carbon during the formation of bainitic subunits was investigated. This approach is capable of taking into account a range of microstructural parameters, such as the dislocation density, subunit thickness, trapping of carbon, etc., to allow for meaningful investigations of their influence. The presented models can be readily adapted to more complex systems with more alloying elements or a variety of different precipitates. The results concerning film thickness and carbon content of austenite films can be used to optimize heat treatments, while the novel suggested mechanism that leads to the formation of upper or lower bainite, might inspire the setup of future experiments to see if the predictions of the simulations hold true.

6. References

[1] B. C. De Cooman, “Structure-properties relationship in TRIP steels containing carbide-free bainite,” *Curr. Opin. Solid State Mater. Sci.*, vol. 8, no. 3–4, pp. 285–303, 2004.

[2] D. Krizan, K. Spiradek-Hahn, and A. Pichler, “Relationship between microstructure and mechanical properties in Nb–V microalloyed TRIP steel,” *Mater. Sci. Technol.*, vol. 31, no. 6, pp. 661–668, 2015.

[3] S. Traint, A. Pichler, R. Sierlinger, H. Pauli, and E. A. Werner, “Low-alloyed TRIP-Steels with Optimized Strength, Forming and Welding Properties,” *steel Res. Int.*, vol. 77, no. 9–10, pp. 641–649, Sep. 2006.

[4] M. B. and A. P. D. Krizan, S. Traint, R. Sierlinger, H. Pauli, “Customer oriented development and optimization of cold rolled intercritically annealed multiphase TRIP sheet steels,” in *Proc. 2nd Int. Conf. on ‘Steels in cars and trucks,’* 2008, pp. 26–33.

[5] M. Soleimani, A. Kalhor, and H. Mirzadeh, “Transformation-induced plasticity (TRIP) in advanced steels: A review,” *Mater. Sci. Eng. A*, vol. 795, no. August, p. 140023, 2020.

[6] E. S. Davenport and E. C. Bain, *Transformation of austenite at constant subcritical temperatures*. American Institute of Mining and Metallurgical Engineers, 1930.

[7] L. C. D. Fielding, “The Bainite Controversy,” *Mater. Sci. Technol.*, vol. 29, no. 4, pp. 383–399, 2013.

[8] R. F. Hehemann, K. R. Kinsman, and H. I. Aaronson, “A debate on the bainite reaction,” *Metall. Trans.*, vol. 3, no. 5, pp. 1077–1094, 1972.

[9] W. Bleck, X. Guo, and Y. Ma, “The TRIP Effect and Its Application in Cold Formable Sheet Steels,” *Steel Res. Int.*, vol. 88, no. 10, pp. 35–45, 2017.

[10] F. D. Fischer, G. Reisner, E. Werner, K. Tanaka, G. Cailletaud, and T. Antretter, “New view on transformation induced plasticity (TRIP),” *Int. J. Plast.*, vol. 16, no. 7, pp. 723–748, 2000.

[11] D. Krizan, “TRIP STEELS: ADVANCED HIGH STRENGTH MULTIPHASE STEELS FOR AUTOMOTIVE APPLICATIONS,” Oct. 2006.

[12] P. Retzl, S. Zamberger, and E. Kozeschnik, “Computational analysis of austenite film thickness and C-redistribution in carbide-free bainite,” *Mater. Res. Express*, vol. 8, no. 7, 2021.

[13] S. M. C. van Bohemen, “Bainite and martensite start temperature calculated with exponential carbon dependence,” *Mater. Sci. Technol.*, vol. 28, no. 4, pp. 487–495, 2011.

[14] S. J. Lee and K. S. Park, “Prediction of martensite start temperature in alloy steels with different grain sizes,” *Metall. Mater. Trans. A Phys. Metall. Mater. Sci.*, vol. 44, no. 8, pp. 3423–3427, 2013.

[15] J. Wang and S. Van der Zwaag, “Stabilization mechanisms of retained austenite in transformation-induced plasticity steel,” *Metall. Mater. Trans. A Phys. Metall. Mater. Sci.*, vol. 32, no. 6, pp. 1527–1539, 2001.

[16] M. De Meyer, J. Mahieu, and B. C. De Cooman, “Empirical microstructure prediction method for combined intercritical annealing and bainitic transformation of TRIP steel,” *Mater. Sci. Technol.*, vol. 18, no. 10, pp. 1121–1132, 2003.

[17] D. Koistinen and R. Marburger, “A general equation prescribing the extent of the austenite-martensite transformation in pure iron-carbon alloys and plain carbon steels*,” *Acta Metall.*,

no. 7, pp. 59–60, 1959.

[18] K. Sugimoto and M. Mukherjee, *TRIP aided and complex phase steels*. Elsevier Ltd, 2016.

[19] K. Sugimoto, M. Misu, M. Kobayashi, and H. Shirasawa, “Effects of Second Phase Morphology on RetainedAustenite Morphology and Tensile Properties in a TRIP-aided Dual-phase Steel Sheet.,” *ISIJ Int.*, vol. 33, no. 7, pp. 775–782, 1993.

[20] M. Y. Sherif, C. G. Mateo, T. Sourmail, and H. K. D. H. Bhadeshia, “Stability of retained austenite in TRIP-assisted steels,” *Mater. Sci. Technol.*, vol. 20, no. 3, pp. 319–322, 2004.

[21] X. D. Wang, B. X. Huang, Y. H. Rong, and L. Wang, “Microstructures and stability of retained austenite in TRIP steels,” *Mater. Sci. Eng. A*, vol. 438–440, no. SPEC. ISS., pp. 300–305, 2006.

[22] T. George, E. R. Parker, and R. O. Ritchie, “Susceptibility to hydrogen attack of a thick-section 3Cr–1 Mo–1 Ni pressure-vessel steel-role of cooling rate,” *Mater. Sci. Technol.*, vol. 1, no. 3, pp. 198–208, 2014.

[23] R. M. Horn and R. O. Ritchie, “Mechanisms of tempered martensite embrittlement in low alloy steels,” *Metall. Trans. A*, vol. 9, no. 8, pp. 1039–1053, 1978.

[24] H. K. D. H. Bhadeshia and D. V. Edmonds, “Bainite in silicon steels: new composition–property approach Part 2,” *Met. Sci.*, vol. 17, no. 9, pp. 420–425, 1983.

[25] Z. G. Yang and H. S. Fang, “An overview on bainite formation in steels,” *Curr. Opin. Solid State Mater. Sci.*, vol. 9, no. 6, pp. 277–286, 2005.

[26] H. K. D. H. Bhadeshia, *BAINITE IN STEELS*, 3rd ed. 2015.

[27] M. Takahashi and H. K. D. H. Bhadeshia, “Model for transition from upper to lower bainite,” *Mater. Sci. Technol.*, vol. 6, no. 7, pp. 592–603, 1990.

[28] G. Spanos, H. S. Fang, and H. I. Aaronson, “A mechanism for the formation of lower bainite,” *Metall. Trans. A*, vol. 21, no. 6, pp. 1381–1390, 1990.

[29] S. A. Sajjadi and S. M. Zebarjad, “Isothermal transformation of austenite to bainite in high carbon steels,” *J. Mater. Process. Technol.*, vol. 189, no. 1–3, pp. 107–113, 2007.

[30] P. Retzl and E. Kozeschnik, “The tale of upper and lower bainite: A computational analysis of concurrent C-diffusion and precipitation,” *Scr. Mater.*, vol. 248, no. November 2023, p. 116146, 2024.

[31] E. Kozeschnik, “Mean-Field Microstructure Kinetics Modeling,” *Encycl. Mater. Met. Alloy.*, vol. 4, pp. 521–526, 2021.

[32] B. Sonderegger and E. Kozeschnik, “Generalized nearest-neighbor broken-bond analysis of randomly oriented coherent interfaces in multicomponent Fcc and Bcc structures,” *Metall. Mater. Trans. A Phys. Metall. Mater. Sci.*, vol. 40, no. 3, pp. 499–510, 2009.

[33] B. Sonderegger and E. Kozeschnik, “Size dependence of the interfacial energy in the generalized nearest-neighbor broken-bond approach,” *Scr. Mater.*, vol. 60, no. 8, pp. 635–638, 2009.

[34] E. Kozeschnik, J. Svoboda, P. Fratzl, and D. F. Fischer, “Modelling of kinetics in multi-component multi-phase systems with spherical precipitates I: Theory,” *Mater. Sci. Eng. A*, vol. 385, no. 1–2, pp. 157–65, 2004.

[35] S. Georg, “Simulation of Precipitation in Steel Simulation of Precipitation in Steel,” *PhD. Diss.*, 2017.

[36] E. Kozeschnik, *Modeling Solid-State Precipitation*. New York: Momentum Press, 2013.

[37] J. Svoboda, F. D. Fischer, P. Fratzl, and E. Kozeschnik, “Modelling of kinetics in multi-component multi-phase systems with spherical precipitates II: Numerical solution and application,” *Mater. Sci. Eng. A*, vol. 385, no. 1–2, pp. 166–174, 2004.

[38] L. Onsager, “Reciprocal Relations in Irreversible Processes. I.,” *Phys. Rev.*, vol. 37, pp. 405–426, 1931.

[39] N. Saunders and A. P. Miodownik, *CALPHAD (Calculation of Phase Diagrams): A Comprehensive Guide*. 1998.

[40] D. Zügner, S. Zamberger, N. Yigit, G. Rupprechter, and E. Kozeschnik, “Thermal Desorption Spectra of H in an Fe–C–Nb Alloy Evaluated by Diffusion Simulation,” *Steel Res. Int.*, vol. 91, no. 12, pp. 1–9, 2020.

[41] Y. V. Shan, M. Soliman, H. Palkowski, and E. Kozeschnik, “Modeling of Bake Hardening Kinetics and Carbon Redistribution in Dual-Phase Steels,” *Steel Res. Int.*, vol. 92, no. 1, 2021.

[42] F. Mas, Doctoral Thesis, University Grenoble Alpes, 2015.

[43] F. G. Caballero and H. K. D. H. Bhadeshia, “Very strong bainite,” *Curr. Opin. Solid State Mater. Sci.*, vol. 8, no. 3–4, pp. 251–257, 2004.

[44] F. G. Caballero, M. K. Miller, and C. Garcia-Mateo, “Slow bainite: An opportunity to determine the carbon content of the bainitic ferrite during growth,” *Solid State Phenom.*, vol. 172–174, pp. 111–116, 2011.

[45] G. Speich, “Tempering of low-carbon martensite,” *Trans Met Soc AIME*, vol. 245, no. 12, pp. 2553–2564, 1969.

[46] M. Peet, S. S. Babu, M. K. Miller, and H. K. D. H. Bhadeshia, “Three-dimensional atom probe analysis of carbon distribution in low-temperature bainite,” *Scr. Mater.*, vol. 50, no. 10, pp. 1277–1281, 2004.

[47] J. Svoboda, Y. V. Shan, E. Kozeschnik, and F. D. Fischer, “Determination of depths of traps for interstitials from thermodynamic data: A new view on carbon trapping and diffusion,” *Model. Simul. Mater. Sci. Eng.*, vol. 21, no. 6, 2013.

[48] J. Svoboda and F. D. Fischer, “Modelling for hydrogen diffusion in metals with traps revisited,” *Acta Mater.*, vol. 60, no. 3, pp. 1211–1220, 2012.

[49] F. D. Fischer, J. Svoboda, and E. Kozeschnik, “Interstitial diffusion in systems with multiple sorts of traps,” *Model. Simul. Mater. Sci. Eng.*, vol. 21, no. 2, 2013.

[50] J. Svoboda, G. A. Zickler, E. Kozeschnik, and F. D. Fischer, “Kinetics of interstitial segregation in Cottrell atmospheres and grain boundaries,” *Philos. Mag. Lett.*, vol. 95, no. 9, pp. 458–465, 2015.

[51] W. Mayer, S. Sackl, Y. V. Shan, S. Primig, and E. Kozeschnik, “Evolution of precipitates and martensite substructure during continuous heat treatment,” *Mater. Today Proc.*, vol. 2, no. 1, pp. S619–S622, 2014.

[52] F. G. Caballero, C. Garcia-Mateo, M. J. Santofimia, M. K. Miller, and C. García de Andrés, “New experimental evidence on the incomplete transformation phenomenon in steel,” *Acta Mater.*, vol. 57, no. 1, pp. 8–17, 2009.

[53] M. Azuma, N. Fujita, M. Takahashi, and T. Lung, “Modelling upper and lower bainite trasformation in steels,” *Mater. Sci. Forum*, vol. 45, no. 2, pp. 221–228, 2003.

[54] L. Guo, H. Roelofs, M. I. Lembke, and H. K. D. H. Bhadeshia, “Modelling of transition from upper to lower bainite in multi-component system,” *Mater. Sci. Technol. (United Kingdom)*, vol. 33, no. 4, pp. 430–437, 2017.

Section B

Paper I

Simulation of Carbo-Nitride Precipitation in the Multi-Phase Microstructure of Micro-Alloyed Transformation-Induced Plasticity Steel

Philipp Retzl, Walter Mayer, Daniel Krizan and Ernst Kozeschnik

Steel research international

Volume 92, Issue 1, Year 2021, 202000197

Simulation of carbo-nitride precipitation in the multi-phase microstructure of micro-alloyed TRIP steel

Philipp Retzl[a,b], Walter Mayer[c], Daniel Krizan[d], Ernst Kozeschnik[a]

[a]Institute of Materials Science and Technology, TU Wien Getreidemarkt 9, 1060 Vienna, Austria

[b]Materials Center Leoben Forschung GmbH, Roseggerstraße 12, 8700 Leoben, Austria

[c]Christian Doppler Laboratory "Early Stages of Precipitation", Institute of Materials Science and Technology, TU Wien, Getreidemarkt 9, 1060 Vienna, Austria

[d]R&D Dept., Business Unit Coil, voestalpine Stahl GmbH, Linz, Austria

Keywords: thermo-kinetic simulations, carbo-nitride precipitation, multi-phase microstructures, micro-alloyed TRIP steel

Abstract

During the thermo-mechanical treatment of low-carbon TRIP steel, precipitation of micro-alloying carbo-nitrides occurs in a complex microstructure consisting of various phases and mixtures of these, such as, austenite, ferrite, pearlite, bainite, and/or martensite. In addition, the precipitation process is commonly stimulated and accelerated by plastic deformation that is induced by hot and warm rolling. In the present contribution, a method is suggested, which allows for a thermokinetics-based simulation of the amount as well as the type and distribution of secondary precipitates depending on the local chemical and crystal environment of the polymorph microstructure. As basis of the present study serves the thermokinetic software package MatCalc, which is used to simulate the evolution of precipitates during the entire steel processing route. It is demonstrated that this approach represents a simple, yet versatile tool for a computationally efficient analysis of precipitation in multi-phase microstructures. According to the present simulation results, the distribution

of C among individual precipitation domains, i.e. phases, is the most important factor governing the precipitate evolution in the system. In addition, the simulations show that NbC and VC precipitates differ in their nucleation and growth behaviour during the thermo-mechanical treatment. While NbC nucleates mainly during the hot rolling process in a purely austenitic matrix, VC predominantly forms at lower temperatures in ferrite.

1. Introduction

The current strong demand for materials supporting weight reduction of vehicles challenges steel manufacturers to develop new advanced grades capable of fulfilling the increasingly stringent technical requirements of this market. Advanced high strength steels (AHSS) include many standard and proprietary grades designed to provide specific desirable combinations of properties, such as, high tensile strength levels between 600 and 780 MPa, sufficient formability and appropriate weldability. AHSS of the first generation include dual phase (DP), complex phase (CP) and transformation-induced plasticity (TRIP) steels, commonly used in crash-relevant parts, such as, door beams and windshield pillars.[1,2,3]

TRIP steels exhibit the highest combination of strength and formability, resulting from the strain-induced transformation of retained austenite to martensite, designated as the TRIP effect.[4,5,6,7] To reduce thickness of safety related vehicle components even further, TRIP steels with strength levels higher than 780 MPa are therefore of a paramount importance.

On basis of the micro-alloying concept, an increase in strength can be initiated by precipitation strengthening and grain refinement in order to achieve 1 GPa in tensile strength, while weldability is not deteriorated as it would be in the case of an increased C content. Previous experiments showed a differing behaviour of MC (M=Nb, V) precipitates in ferrite and in austenite due to their different solubility in these two microstructural

constituents and the differences in diffusion coefficients.[8] In order to monitor mechanical properties in relation to the microstructure, precise knowledge of the precipitation state at the end of a thermo-mechanical treatment is of prime importance.

For this purpose, various computer models have been developed in the past allowing for a prediction of the influence of process parameters on microstructure, carbon distribution between different phases and the state of precipitation.[9,10,11,12] In the present work, the software package MatCalc [13] is utilized throughout, since it provides a thermodynamic engine based on CALPHAD-type databases as well as a multi-component multi-phase precipitation kinetics engine, which is particularly suitable for application to complex technical alloys with several alloying elements and various types of precipitates. Application of this software and details on the underlying simulation models have been described in, e.g., [11,14,15,16]. The study of micro-alloying effects in TRIP steels is a relatively recent topic of research due to their more complex physical metallurgy compared to conventional high strength low alloyed (HSLA) steels. The higher C content of TRIP steels (up to ~0.25 wt-%) accelerates the kinetics of carbide precipitation during processing.

In micro-alloyed TRIP steel, the precipitates are present in a complex triple-phase microstructure, consisting typically of ferrite, bainite and retained austenite. The microstructure is formed after intercritical annealing (IA) and a subsequent isothermal annealing in the bainitic transformation region, denoted as overaging (OA). The C content in austenite is increased, both, during IA and during OA. The C enrichment during OA is the result of the suppression of the formation of carbides during the bainitic transformation, due to the presence of alloying elements, such as, Al and Si. The enrichment of C increases the thermodynamic stability of the austenite and, consequently, makes it possible that austenite is retained upon cooling to room temperature.[17,18]

The aim of the present study is to characterise and quantify the precipitation state in the multi-phase microstructure of the investigated TRIP steel during processing by means of computational thermokinetics. In the analysis, mean radii, phase fractions and number densities of precipitates are calculated and compared to experimental results. The precipitation state is presented at different stages of the thermo-mechanical treatment, i.e. before coiling, after reheating to IA temperature and in the OA step.

2. Experimental

2.1 Investigated material

The chemical composition of the investigated TRIP steel is summarized in **Table 1**. The C content of this steel grade is kept low at 0.22 wt-% due to the requirement of good weldability, while the Si content is limited to 0.6 wt-% in order to guarantee suitable galvanisability. The addition of 0.8 wt-% Al supports Si in suppressing cementite formation in bainite, which consequently produces an adequate TRIP effect. In order to investigate the influence of micro-alloying in TRIP steels, 0.04 wt-% Nb and 0.1 wt-% V are simultaneously added to the final composition.

Table 1. Nominal chemical composition of the micro-alloyed TRIP steel in wt-%

Element	C	N	Si	Mn	Al	V	Nb
Content in wt-%	0.22	0.004	0.60	2.26	0.82	0.10	0.04

2.2 Thermo-mechanical treatment

The investigated steel is industrially cast and processed as shown in **Figure 1**. After continuous casting, the cut slabs are homogenized in a reheating furnace at 1200°C for

about 2 h and subsequently hot rolled to a thickness of 3.4 mm using an industrial hot rolling mill. The finishing and coiling temperatures are 900°C and 650°C, respectively. After hot rolling, the sheets are pickled and cold rolled to a final thickness of 1.5 mm. The cold rolled sheets are annealed in a continuous annealing line (CAL) with an IA temperature of 820°C followed by OA in the bainitic region at approximately 425°C in order to obtain the final TRIP microstructure.

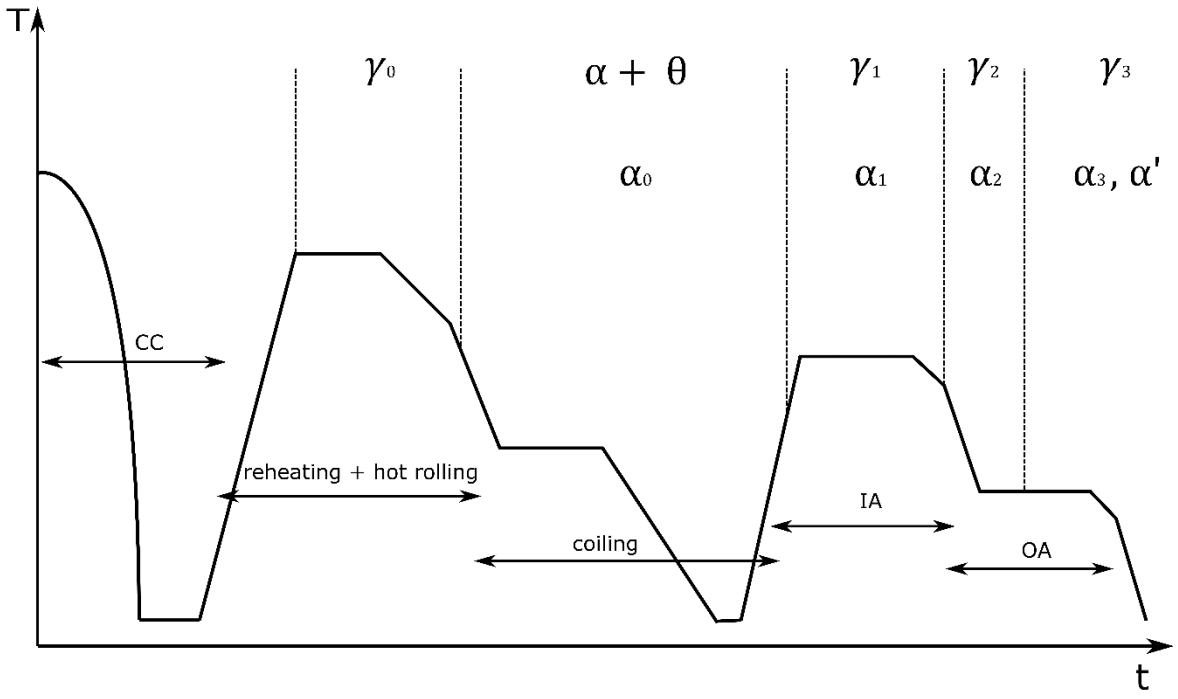

Figure 1. Schematic representation of the thermo-mechanical treatment in the present investigation (CC…Continuous Casting, IA…Intercritical Annealing; OA...Overaging)

A schematic representation of the heat treatment with the active matrix phases during the process is shown in Figure 1. Starting from pure austenite (γ_0) after reheating, the steel decomposes into ferrite (α_0) and pearlite ($\alpha_0+\theta$). The continuous casting step is neglected in the present analysis because the reheating step leads to a fully austenitic microstructure with all precipitates dissolved. During the later stages of the industrial heat treatment, the

steel evolves into ferrite (α_1) with a different C content than α_0, pro-eutectoid ferrite (α_2), carbide-free bainite (α_3), retained austenite (γ_3), and martensite (α'). Each of these constituents has particular microstructural features with a distinct chemical composition, which impacts the precipitation state. γ_1 and γ_2 denote intermediate austenitic microstructural states during the evolution into the final multi-phase microstructure.

2.3 Microstructural characterization

The steel microstructure is revealed by LePera colour etching [19], where ferrite appears in blue color, bainite is dark and retained austenite/martensite islands can vary from white (a higher C content) to brownish (a lower C content).. The grain sizes of ferrite and retained austenite are determined by the mean intercept method[20]. The length of test lines with a defined distance from each other are measured per particle in three directions: 0, 45 and 90°. The mean intercept length is the arithmetic average of all measured lines. The analysis involves the measurement of 25 ferrite and 25 retained austenite grains, respectively.

In order to determine the volume fraction of ferrite, image analysis is employed on 15 colour etched micrographs.

The fraction of bainitic ferrite in the investigated steel is characterized by means of dilatometric experiments using a Bähr dilatometer DIL 805A/D with the sample dimensions of 1.5x3.1x10 mm^3 prepared from the as cold rolled initial state. To evaluate the fraction of bainitic ferrite, the normalized length of the dilatometer Δl_{norm} (%) is used:

$$\Delta l_{norm} = \frac{l - l_0}{l_{max}} 100 \qquad (1)$$

where l is the instantaneous length (µm), l_0 (µm) is the initial length at the beginning of the overaging and l_{max} (µm) represents the total length after quenching to room temperature.

The amount of retained austenite is measured by X-ray diffraction (XRD), whereas the C content of retained austenite is calculated from the XRD data using the equation proposed by Dyson and Holmes[21].

Thin foils were produced for high-resolution scanning transmission electron microscopy (HR STEM) observations by mechanical grinding of disks of 3mm diameter followed by electro-polishing in acetic acid containing 5-10% perchlorid acid. A Philips CM20 with an acceleration voltage of 200kV is used for TEM analysis.

The equivalent circle diameter (ECD) of 120 to 150 precipitate particles is determined separately in ferrite and austenite from the TEM images. The precipitates are identified by Selected Area Diffraction (SAD) and Energy Dispersive X-ray (EDAX) analysis. Further information on mechanical properties and experimental details related to the investigated Nb-V micro-alloyed TRIP steel is described elsewhere.[8]

3. Results and discussion

3.1 Microstructural observation

Figure 2 shows the light optical microscopy (LOM) image of the microstructure with LePera colour etchant. The microstructure of the steel in the as-produced state consists of a ferritic matrix surrounded by bainitic and retained austenitic/martensitic islands. The grain size of ferrite and retained austenite/martensite determined by the mean intercept method is (3.9±0.6) µm and (1.65±0.1) µm, respectively.

Figure 3 illustrates the scanning electron microscopy image (SEM) representing the detail of the final microstructure with the emphasis on the location and morphology of the bainitic ferrite. This microstructural compound has a globular morphology and is exclusively located

between the retained austenite/martensite islands. The globular morphology indicates a nucleation mode from the existing precipitates rather than the typical nucleation mode from the grain boundaries as known in the case of lamellar bainite.

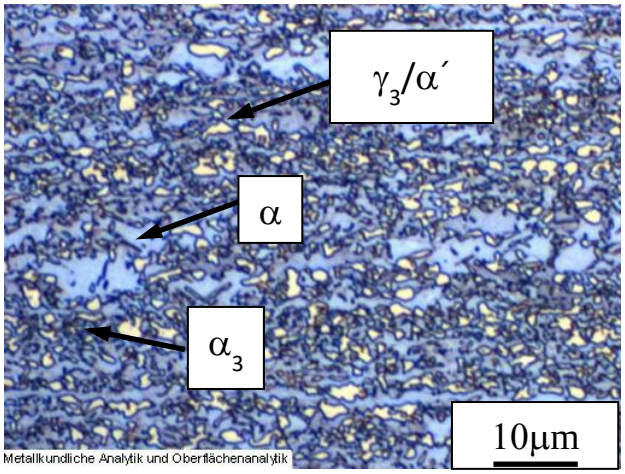

Figure 2. LOM of the final steel microstructure; ferrite (α)…blue; retained austenite (γ3)/martensite (α´)…white to brownish; bainitic ferrite (α3)…dark

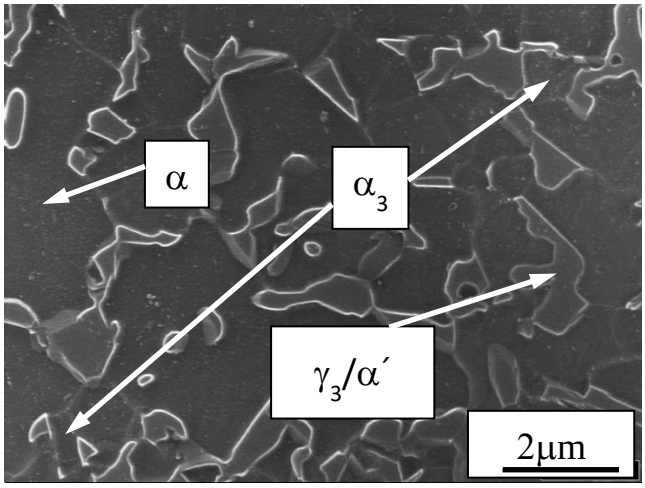

Figure 3. SEM image depicting the areas of globular bainitic ferrite in the final steel microstructure

3.2 Precipitation state

TEM micrographs, representing the precipitation state in ferrite and retained austenite, are shown in **Figure 4**. Ferrite and retained austenite contain numerous small precipitates identified by SAD and EDAX as mostly pure carbides, i.e., Nb-rich precipitates with small amounts of V, as well as V-rich precipitates with minor amount of Nb. Co-precipitation and formation of complex solution phases, i.e., Nb+V containing precipitates, are observed to a very limited extent. The diameter of precipitates in the ferrite and retained austenite is determined with 13.5 ± 5.4 nm and 9.8 ± 4.2 nm, respectively. The density of precipitates is higher in ferrite compared to all low temperature transformation products, i.e. bainite, retained austenite and martensite. The precipitate density in ferrite is observed with 120 ± 46 particles per μm^2 and in retained austenite with 90 ± 38 particles per μm^2.

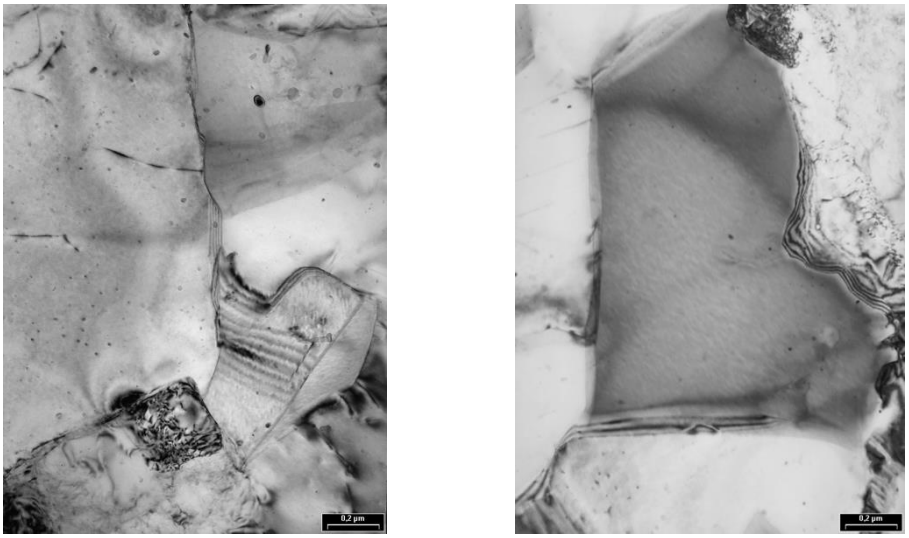

Figure 4. TEM micrograph including precipitates in ferrite (left) and austenite (right)

3.3 Phase fraction

Table 2 summarizes the experimental results for the volume fraction of individual microstructural constituents during the final CAL heat treatment and the C content of retained austenite after cooling to room temperature. At T_{AN} of 820°C, 50 vol.-% of ferrite

and 50 vol.-% of austenite is measured by means of image analysis. During cooling from IA to OA, an additional 5 vol.-% of pro-eutectoid ferrite is formed. In the OA section, ~20 vol.-% of carbide-free bainite is formed. 15.5 vol.-% of austenite persist after final cooling to room temperature. The retained austenite contains 0.87 wt-% of carbon as determined indirectly by XRD. It is important to note that this value is a mean value of C in the austenite that is formed during IA, which is only slightly enriched in carbon during the bainitic transformation, and austenite films that are trapped between the bainitic ferrite plates or sheaves.[22,23] The latter are supposed to be more enriched in C, however, no measurement has been performed to obtain corresponding information. Some fresh martensite (9.5 vol.-%) forms upon final cooling due to the partially insufficient stabilization of retained austenite.

Table 2. Measured matrix volume fractions (vol %) at distinct points during the HT and carbon content in retained austenite (wt-%). TAN, tAN... annealing temperature/time, TOA, tOA ... overaging temperature/time

Heat treatment $T_{AN}/t_{AN}+T_{OA}/t_{OA}$	$\alpha_{1,2}$	α_3	γ_{1-3}	C in γ_3	α'
820°C/60s	50	-	50		-
820°C/60s + 425°C/0s	55	-	45		-
820°C/60s + 425°C/360s +RT	55	20	15.5	0.87	9.5

4. Simulation/Modelling

4.1 General considerations

To simulate the entire production process of a material with a complex multiphase microstructure, the effect of different matrix phases, e.g., ferrite and austenite, on the precipitation kinetics must be considered. Therefore, the simulation performed in MatCalc utilizes different precipitation domains with certain thermodynamic matrix phases and C levels. These are domains for pure ferrite, austenite and marteniste, as well as domains

representing complex structures, such as, pearlite and bainite. To take primary precipitates into account, which can form in the course of the continuous casting process in the liquid state, a Scheil-Gulliver calculation is carried out beforehand. The primary precipitates observed in these simulations are transferred into the kinetics simulation in the form of Gaussian-distributed precipitates with a mean radius of 2 µm. The number density of primary precipitates is determined from the size distribution as well as the phase fraction of primaries at 3% residual liquid from the Scheil-Gulliver simulation. Generation of the primary precipitate distribution with appropriate chemical composition of the particles is performed automatically through the MatCalc software.

In additional preliminary simulations, it is observed that the smaller non-primary precipitates that appear after the solidification process and during the reheating step, dissolve again during holding at the reheating temperature. Consequently, the simulations start with the reheating step including the primary precipitates. This is done because primary precipitates are usually of several µm size and they are not significantly altered in the course of any heat treatment step following solidification. The phase transformations that occur before this heating step are neglected, as well as the secondary precipitates, since these are fully dissolved again, in contrast to the primary precipitates.

When the material is held at the reheating temperature, homogeneous austenite with primary precipitates persists, being the starting point for the precipitation kinetics simulation. To get an overview of the simulation steps, the general structure, and the precipitation domains that are active during each step see **Figure 5**. **Figure 6** shows the course of the thermo mechanical treatment. The precipitation state at the end of each simulation step is used as starting condition for the next part of the simulation. The

thermokinetic setup that is used and a detailed description of the simulation steps are given subsequently.

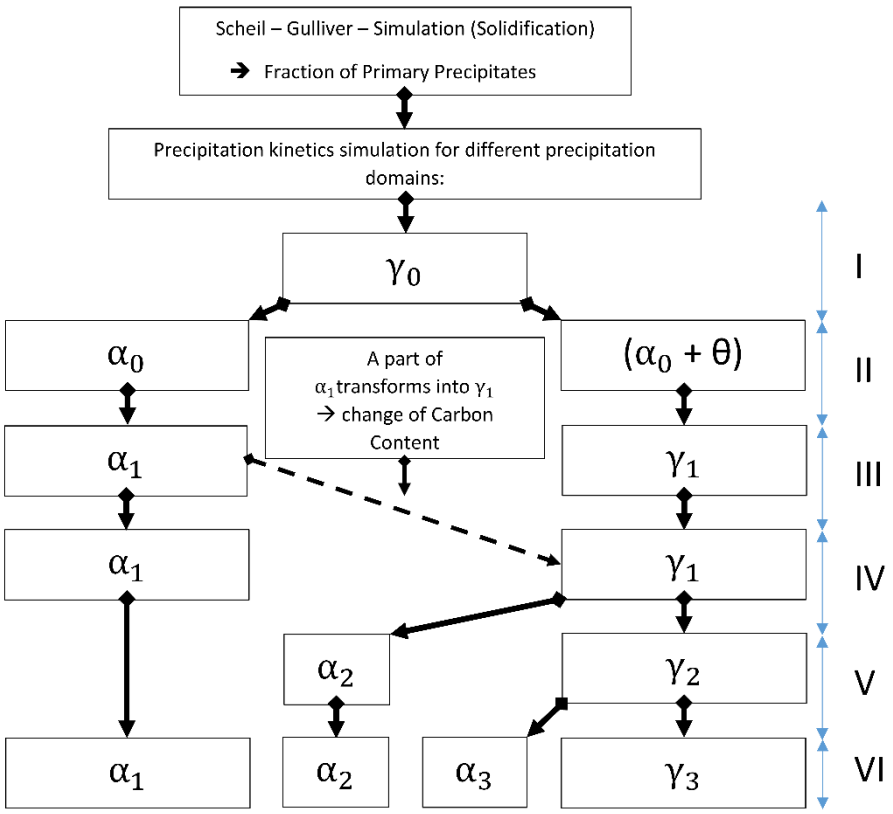

Figure 5. Flowchart showing the individual simulation steps. Boxes designated with α_i represent precipitation domains with a bcc/ferrite matrix, while γ_i marks fcc/austenite domains.

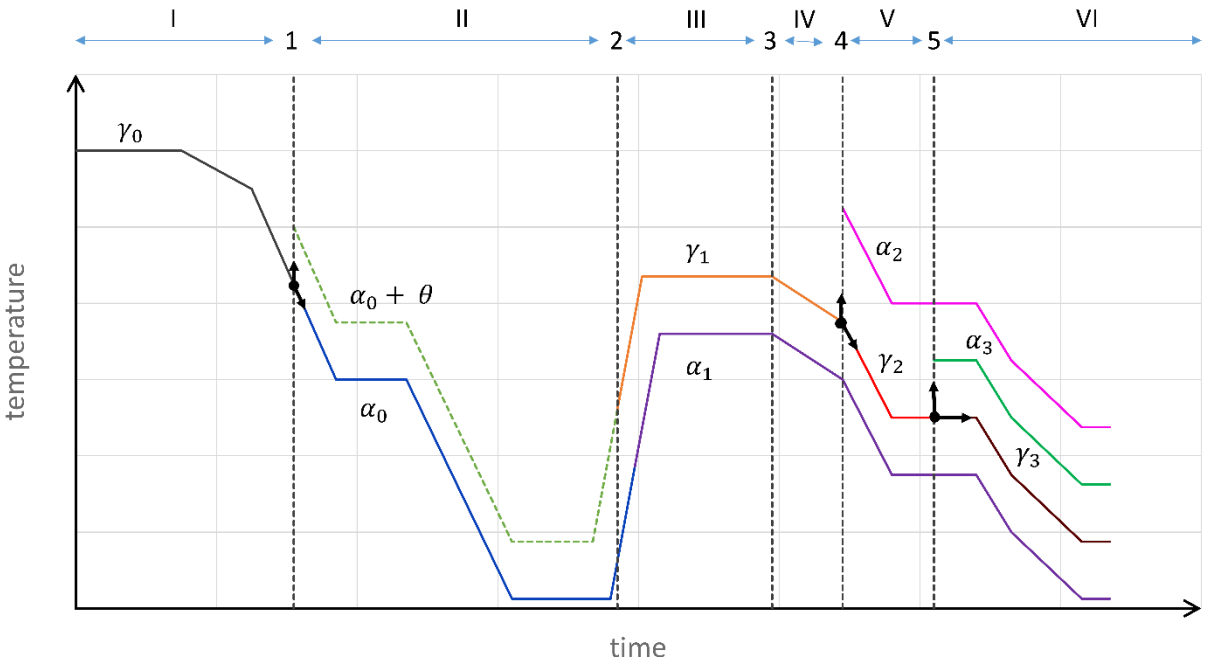

Figure 6. Schematic illustration of the active precipitation domains during simulation of the thermo-mechanical treatment.

4.2 Thermokinetic setup

For the numerical simulation of precipitation during processing of the TRIP steel, the software package MatCalc [13], version 6.03.1000, in combination with the thermodynamic database mc_fe.tdb (v2.060) and the diffusion database mc_fe.ddb (v2.012) is used. The phases LIQUID, FCC_A1 (austenite and MX-type carbides, with M … Ti, Nb, V, and X … C, N), BCC_A2 (ferrite/martensite), ALN, and CEMENTITE are included in the calculations. The selected properties are summarized in **Table 3** for the thermokinetic matrix phases (austenite, ferrite) and in **Table 4** for the precipitate populations together with further information on the parameters used in the dislocation density evolution model (ABC-model) [11][24] and the diffuse interface energy model [12] with the regular solution critical temperature, T_{crit}, as relevant input parameter.

Table 3. Summary of matrix properties

	MC Phase	Equilibrium Disl. Dens. (DD) [m/m^3]	Grain size [µm]	DD Evolution [-]		
				A	B	C
Austenite	FCC_A1	10^{11}	1.65	50	1	10^{-4}
Ferrite	BCC_A2	10^{12}	4	50	2	10^{-3}

Table 4. Summary of precipitate properties (d…dislocations, g…grain boundaries, m… minimum nucleation-barrier, o…ortho-equilibrium, Tcrit…regular solution critical temperature in austenite and ferrite, respectively)

Phase (MatCalc Alias)	Nucleation Site	Nucleation model	Major constituents	Volumetric misfit [-]	T_{crit}^{aust} [K]	T_{crit}^{ferr} [K]
Fe_3C (CEMENTITE)	d	m	Fe, C	-	-	-
AlN (ALN)	d + g	o	Al, N	0.27	-	-
NbC (FCC_A1#01)	d [25]	m	Nb,C	0.1	2900	3800
VC (FCC_A1#02)	d [14]	m	V, C	-	1900	2200

A conventional precipitation kinetic simulation in MatCalc starts with the nominal composition of a homogeneous matrix as major input data, takes the prescribed thermo-mechanical treatment conditions and lets the system evolve in time through numerical integration of the evolution equations. In the preliminary simulation step, thermodynamic equilibrium calculations with the nominal composition are performed to determine the choice of composition sets for precipitates [26] in the subsequent precipitation kinetics simulation. Starting in the liquid one-phase phase field, the temperature is gradually lowered down to 400°C according to the prescribed heat treatment. In addition to the expected matrix phases, δ-ferrite, austenite, α-ferrite and cementite, various precipitate phases are observed, i.e., micro-alloying carbides (VC and NbC) and nitrides (AlN). For the two carbide phases, composition sets are generated on basis of the parent FCC_A1 phase with the major

constituent of C on the interstitial sublattice and V and Nb on the substitutional sublattice, respectively (Table 4). They are denoted by a hash (#) and indices 01 and 02. The abbreviations “m” and “o” for the nucleation-composition models in Table 4 refer to the nucleus composition models with minimum nucleation-barrier, ortho-equilibrium (maximum driving force)[26], respectively.

4.2.1 Primary precipitates

Since the models for kinetic calculations in MatCalc have been developed for solid-solid transformations [26], primary precipitates forming in the liquid state must be taken into account indirectly with the help of a Scheil-Gulliver simulation. Due to the fact that these first precipitates already pick up and bind alloying elements, they alter the overall chemical composition of the matrix phase (i.e. the precipitation domain) and, therefore, need to be taken into account in an accurate simulation. Primary precipitates nucleate and grow in the residual liquid pockets before final solidification during casting. Although primary precipitates are commonly not further involved in the evolution of precipitation reactions after solidification due to their large size and wide spacing, they can still potentially impact the secondary precipitation behaviour after solidification. With the help of the Scheil–Gulliver-simulation as integrated in MatCalc and described in Ref. [27], size distributions of primary precipitates with experimentally observed mean precipitate radius and volume fraction given from the Scheil-Gulliver simulation, can be calculated and set up for the kinetic simulation. For the TRIP steel under investigation, AlN and NbC are found as primary precipitates at 3% residual liquid.

4.2.2 Evolution of precipitation domains

The phase fractions found in the equilibrium and Scheil-Gulliver simulation are used in the precipitation calculation to account for a correct initial state, which serves as starting point for kinetic calculations in the fully solidified material (γ_0). The simulated heat treatment begins with the reheating step at 1200°C for about 2h after continuous casting followed by a hot rolling step with implemented dynamic dislocation density evolution [11] in the simulation.

After hot rolling, γ_0 decomposes into two phases, ferrite (α_0) and pearlite (α_0+θ). A time-temperature transformation (TTT) diagram calculated with the Mesplont tool [28] for the industrial process shows the first ferrite to be found at about 720°C. A supplementary thermodynamic equilibrium calculation with MatCalc delivers only austenite, ferrite and cementite as active phases, together with the precipitation phases set to dormant status. The latter means that the simulation accounts for all elements confined in the precipitates but does not alter their configuration (phase fraction and chemical composition) during (constraint) equilibrium calculation. The first cementite phase appears below approximately 700°C, with 33% austenite present before start of the eutectoid transformation.

In the course of this reaction, the austenite phase becomes significantly enriched in C (0.64 wt-%) and decomposes into pearlite on cooling below the eutectoid point. In our simulations, pearlite is represented as a mixture of ferrite and cementite phases. The chemical composition of the pro-eutectoid ferrite and pearlite domains are estimated from the thermodynamic equilibrium calculation at 700°C slightly above the eutectoid temperature (point 1 in Figure 6) with all precipitate phases in dormant state, again. After this transformation, each individual microstructure, i.e., α_0 (ferrite) and α_0+θ (pearlite), including the respective precipitates, are treated independently during the further industrial heat treatment (see scheme in Figure 6).

A most critical factor in the further precipitation simulation of intercritical annealing (IA) with the present approach is the estimation of the correct overall carbon content in each precipitation domain. To get appropriate quantities, back transformation of the α_0+θ pearlitic microstructure into austenite (γ_1) during reheating in the continuous annealing line (CAL) has to be accounted for. Quenching experiments (Table 2) show an approximately equal amount of austenite (γ_1) and ferrite (α_1) after 60s at the IA temperature. Taking this into account, the phase fractions in the simulation are adjusted such that the chemical compositions calculated at point 1 are correctly weighted mean values representing an equal distribution of the austenite and ferrite phase. Therefore, the carbon content in austenite (γ_1) precipitation domain at point 3 is set to 0.42 wt-% and that of the ferrite domain to 0.02 wt-%.

Experimental results in Table 2 show that the final microstructure consists of 55 vol.-% ferrite at room temperature. The additional 5 vol.-% ferrite are formed during cooling in the CAL, when γ_1 decomposes into pro-eutectoid ferrite (α_2) and a carbon enriched austenite (γ_2). When only looking at the austenite precipitation domain at this instance of the simulation, the point of next phase splitting is determined such as to get 10% ferrite in an equilibrium calculation as described above. The pro-eutectoid ferrite (α_2) line, starting at point 4, is considered as a closed system for the rest of the heat treatment and attached to the results of all ferrite domains in the end.

The carbon enriched austenite (γ_2) is cooled down further and held at the OA temperature where bainite forms. The experimental results in Table 2 suggest that the final product contains 20% bainite (α_3) at the last partitioning reaction of the precipitation domain. XRD measurements at room temperature, combined with the formula of Dyson and Holmes, [21] deliver 0.87 wt-% C in the retained austenite (γ_3). Since the bainitic transformation takes

place at relatively low temperature, the diffusivity of the substitutional elements is many orders of magnitudes lower than that of the interstitial alloying elements, in our simulation, C and N [29]. As nearly all nitrogen is bound in AlN, the N content in the matrix is very low, such that it is held constant in the simulation. Starting from point 4 in Figure 6, one has to deal with only 45% of the whole microstructure, which decomposes further into carbide free bainite (CBF) and retained austenite in a ratio of 4:5. In literature, the carbon content in CBF is given with approximately 0.05 wt-% C [30]. With a starting value of 0.42 wt-% in γ_2, one, therefore, obtains 0.81 wt-% C in austenite (γ_3) after the transformation. **Table 5** shows the active precipitation domains for each simulation step and their corresponding C concentrations and volume fractions.

Table 5. Precipitation domains and the corresponding carbon contents and volume fractions for every simulation step

	Precipitation domains	
Simulation step	Carbon content [wt-%]	Volume Fraction [%]
I	γ_0: 0.22	γ_0 … 100
II	α_0: 0.011 ; $\alpha_0 + \theta$: 0.64	α_0: 66.6 ; $\alpha_0 + \theta$: 33.3
III	γ_1: 0.62 ; α_1: 0.02	γ_1: 33.3 ; α_1: 66.6
IV	γ_1: 0.42 ; α_1: 0.02	γ_1: 50 ; α_1: 50
V	α_1: 0.02 ; γ_2: 0.47 ; α_2: 0.02	α_1: 50 ; γ_2: 45 ; α_2: 5
VI	α_1: 0.02 ; γ_3: 0.81 ; α_2: 0.02 ; α_3: 0.05	α_1: 50 ; α_2: 5 ; γ_3: 25 ; α_3: 20

4.2.3 Evolution of precipitates

In **Tables 6 and 7**, the mean radii of secondary precipitates are summarized during the thermo-mechanical treatment for each precipitation domain. The C content in the domain, in solid solution, and as percent of C in solid solution with respect to the total content are also indicated.

The simulation starts at 0.22 wt-% C in the fully solidified material composed of an austenitic precipitation domain with primary precipitates. The characteristic precipitation quantities,

mean radius, number density and phase fraction, of primary precipitates (AlN and NbC) do not change noticeably during the simulation. First secondary NbC precipitates occur at dislocations, introduced through hot rolling, and grain boundaries, respectively, during cooling down to 900°C. Secondary AlN precipitates together with the primary AlN leave nearly no nitrogen in solid solution. This indicates that there is no more nitrogen available for other precipitation reactions. The first VC forms at dislocations at about 750°C. At 700°C (point 1), the overall carbon content changes to 0.011 and 0.64 wt-% in the ferritic and pearlitic domains, respectively.

In the pearlite precipitation domain (α_0+θ), only few VC precipitates appear during coiling. At room temperature, most of the carbon is bound in cementite, with a phase fraction of 0.1. During reheating in the CAL, the pearlite transforms into austenite (point 2 in Figure 6) and cementite dissolves completely above 750°C. The size of NbC and VC in the austenitic precipitation domains increases only slightly from this simulation step on. After 60s of intercritical annealing at 820°C, the C content of the austenite precipitation domain is reduced to 0.42 wt-%, due to the transformation of ferrite to austenite (point 3 in Figure 6) and the corresponding volume increase of this domain. The increasing C content at points 4 and 5 does not conceivably stimulate the precipitates to continue growing. Overall, the simulation shows that approximately 99% of C remains in solid solution in all austenitic precipitation domains.

The ferrite precipitation domains show an entirely different behaviour regarding the carbon in solid solution, as outlined in Table 6. VC is the first precipitate to be found at 700°C, followed by tertiary cementite (650°C), although, both, with a rather small phase fraction and mean radius. At room temperature, VC has a mean radius of 3.6 nm. At 770°C, during reheating in the CAL, the entire cementite is dissolved again and C diffuses into VC and NbC.

From columns 2 and 3 in Table 6, it is apparent that the mean radius of VC increases considerably and does not stop growing until point 5 is reached in the simulation. The small decrease in size of VC from point 4 to 5 is due to the smaller precipitates from α_2, which, up to this point, grew in an austenitic matrix and, therefore, have remained smaller until then.

Table 6. Simulation results austenite; (α0+θ) represents the pearlitic structure at point 1; precipitation domains in column two represent the precipitation domain from the last simulation step before reaching the simulation point designated in column one.

Simulation point	1	2	3	4	5	final
Prec. domain	γ_0	$\alpha_0+\theta$	γ_1	γ_1	γ_2	γ_3
NbC [nm]	1.52	3.19	3.21	3.21	3.21	3.21
VC [nm]	0.45	4.91	4.92	4.92	5.01	5.01
C [wt-%] domain	0.22	0.64	0.62	0.42	0.47	0.81
C [wt-%] in solid solution	0.218	0.636	0,615	0.416	0.465	0.805
% C in solid solution	99.3%	99.3%	99.2%	99.0%	99.1%	99.4%

Table 7. Simulation results ferrite; results found from point 4 on are a weighted average of α1 and α2 with respect to the volume fraction (i.e. 9:1). precipitation domains in column two represent the precipitation domain from the last simulation step before reaching the simulation point designated in column one.

Simulation point	1	2	3	4	5	final
Prec. Domain	γ_0	α_0	α_1	α_1	$\alpha_1+\alpha_2$	$\alpha_1+\alpha_2$
NbC [nm]	1.52	3.05	3.27	3.28	3.28	3.28
VC [nm]	0.45	3.57	8.31	8.85	8.54	8.54
C [wt-%] in domain	0.22	0.011	0.02	0.02	0.02	0.02
C [wt-%] in solid solution	0.218	0.0064	0.0133	0.013	0.0123	0.0123
% C in solid solution	99.3%	58.2%	66.5%	56.5%	61.5%	61.5%

No experimental investigations concerning the precipitation state in bainite and martensite have been done. Yet, it can be assumed that precipitates in these constituents of the final microstructure do not differ a lot from that in austenite at RT, since diffusivities of microalloying elements are very low at temperatures below 500°C. The simulation results support this assumption because there is no change in size distribution or volume fraction of NbC and VC observed between point 5 and the final states in austenite γ_3 and bainite α_3. According to this observation, an inhomogeneous C distribution in austenite, which could arise during bainitic transformation, should have limited impact on the final state of precipitation, thus reasoning the simplification of a homogenous C distribution in austenite during the last simulation. Secondary AlN precipitation is fully accounted for in the simulation. These precipitates have a rather small mean radius and number density, which is not in disagreement with the experimental data, where they could not be identified due to their small size.

The calculated precipitate diameters in ferrite and retained austenite are finally compared with the experimental data obtained by HR-TEM. In ferrite, the calculated diameters of the large VC (2 x 8.54 nm = 17.08 nm) and smaller NbC (2 x 3.28 nm = 6.6 nm) correlate well with the experimental value (13.5 ± 5.4 nm). In the retained austenite, the calculated precipitate diameters are (2 x 3.21 nm = 6.4 nm) for NbC and (2 x 5.01 nm = 10.0nm) for VC, which again matches with the experimental data (9.8 ± 4.2nm).

The mean radius for NbC, which is approximately 3 nm in the simulations for all precipitation domains of the final microstructure, is difficult to compare with experimental data, since the smaller part of this distribution with very small radii (< 2 nm) is difficult to measure even with HR-TEM. If only precipitates with a radius larger than 2 nm are considered in the evaluation of the mean radius, the radius would be approximately 4.0 nm (diameter of 8 nm)

for all precipitation domains present at the end of the simulation, thus being in fair agreement with experimental data.

Under the assumption that the TEM sample is approximately 100 nm thick, the experimentally obtained precipitate densities of 120 ± 46 particles per μm^2 in ferrite and of 90 ± 38 particles per μm^2 in retained austenite correspond to $(1.2\pm0.46)\cdot10^{21}$ and $(9.0\pm0.38)\cdot10^{20}$ particles per m^3. If all precipitates from the simulation with a radius exceeding 2nm are considered, the calculated number densities are $1.9\cdot10^{21}$ and $1.5\cdot10^{21}$ per m^3 for ferrite (α_1+ α_2) and retained austenite γ_3, respectively, which are in the same order of magnitude as experimental data. The experimentally observed tendency of a higher number density of precipitates in ferrite when compared to austenite is also observed in the simulation.

5. Conclusion

The present work introduces a comprehensive approach to predict the precipitation kinetics in a multi-component multi-phase microstructure in each processing step of micro-alloyed TRIP steel using the thermo-kinetic software MatCalc. The results of the computer simulation are critically compared to the experimental data. The following conclusions are made:

1. A correct and predictive estimation of the C distribution among individual precipitation domains is the most important factor governing the precipitate evolution in the present system. The C distribution is strongly dependent on the phase fractions and C solubility in the individual microstructural components (austenite, ferrite, pearlite, bainite and martensite).

2. NbC predominantly nucleates during hot rolling and grows during the coiling process in ferrite and pearlite. Only minor NbC coarsening is predicted to take place during IA in CAL for the intercritical ferrite and austenite.
3. VC precipitates to a smaller extent during the hot rolling process when compared to NbC due to their higher solubility. The VC precipitates grow to their final size in the CAL. Due to a lower solubility of VC in ferrite compared to austenite, VC precipitates form predominantly in the ferritic phase. This is confirmed by the experimental data using HR-TEM.
4. Good agreement with experimental data is achieved by the model calculations in terms of mean precipitate size.
5. Calculated precipitation densities are in qualitative agreement with experimental data. The tendency of a higher number density of precipitates in ferrite when compared to austenite, indicated by experimental data, is also observed in the simulation.
6. A simulation approach to simulate precipitation evolution in a complex microstructure is applied to the production procedure of a micro-alloyed TRIP steel. This simple, yet versatile method to simulate precipitation kinetics in multi-phase steels can likewise be applied to a variety of production processes in order to obtain insights on factors that influence the evolution of precipitates and, therefore, mechanical properties of the final product.

Acknowledgements

The authors would like to acknowledge the Austrian Research Promotion Agency (FFG) in Vienna for the financial support related to the project No. 810275 “TRIP steels with Rm > 1000 MPa”. Financial support by the Christian Doppler Forschungsgesellschaft (CDG) in the framework of the CD Lab “Early stages of Precipitation” is gratefully acknowledged, Dr. Spiradek-Hahn from University of Leoben is acknowledged for her TEM work.

References

[1] H. Fountain, *New York Times*. **2009**, D1.

[2] J.R. Davis, *Alloying: Understanding the Basics*, ASM International, Ohio, USA, **2001**, 193.

[3] C. Scott, S. Allain, M. Faral, N. Guelton, *Rev. Métallurgie*. **2006**, 103, 293.

[4] B.C. De Cooman, *Curr. Opin. Solid State Mater. Sci.* **2004**, 8, 285.

[5] D. Krizan, in: *Proc. Int. Conf. on 'COM-MAT-TECH',* TRNAVA, **2006**, 659.

[6] S. Traint, A. Pichler, R. Sierlinger, H. Pauli, E.A. Werner, *Steel Res. Int.* **2006** ,77, 641.

[7] D. Krizan, S. Traint, R. Sierlinger, H. Pauli, M. Blaimschein, A. Pichler in: *Proc. 2nd Int. Conf. 'Steels Cars Truck'.*, Wiesbaden, **2008**, 26.

[8] D. Krizan, K. Spiradek-Hahn, A. Pichler, *Mater. Sci. Technol.* **2015**, 31 ,661

[9] M. Santofimia, S. VanBohemen, J. Sietsma, *Journal of the Southern African Institute of Mining and Metallurgy* **2013**, 113, 15.

[10] J. Speer, D.K. Matlock, B.C. De Cooman, J.G. Schroth, *Acta Mater.* **2003**, 51, 2611.

[11] P. Sherstnev, P. Lang, E. Kozeschnik, in: *ECCOMAS Proceedings*, Vienna, **2012,** 5331

[12] B. Sonderegger, E. Kozeschnik, *Metall. Mater. Trans. A Phys. Metall. Mater. Sci.* **2010**, 41, 3262

[13] MatCalc - The Materials Calculator, http://matcalc.at, accessed: 02/2020

[14] R. Radis, E. Kozeschnik, *Model. Simul. Mater. Sci. Eng.*, **2010** ,98, 826.

[15] S. Zamberger, M. Pudar, K. Spiradek-Hahn, M. Reischl, E. Kozeschnik, *Int. J. Mater. Res.*, **2012**, 103, 680

[16] R. Radis, E. Kozeschnik, *Model. Simul. Mater. Sci. Eng.*, **2012**, 20, 055010

[17] L. Zhao, N.H. van Dijk, E. Brück, J. Sietsma, S. van der Zwaag, *Mater. Sci. Eng. A*. **2001** , 313, 145

[18] D. Krizan and B. C. De Cooman, *Metall. Mater. Trans. A Phys. Metall. Mater. Sci.* **2014**, 45, 3481

[19] F.S. LePera, *Metallography*. **1979** ,12, 263

[20] H. Abrams, *Metallography*, 4, **1971**, 59

[21] D. DYSON, B. Holmes, *J. Iron Steel Inst.* **1970** ,208, 469.

[22] H.K.D.H. Bhadeshia, D. V. Edmonds, *Acta Metall.* **1980** ,28, 1265.

[23] A.S. Podder, I. Lonardelli, A. Molinari, H.K.D.H. Bhadeshia, *Proc. R. Soc. A Math. Phys. Eng. Sci.* **2011** ,467, 3141.

[24] H. Buken, E. Kozeschnik, *Metall. Mater. Trans. A Phys. Metall. Mater. Sci.* **2017** ,48, 2812.

[25] R. Radis, *Doctoral Thesis*, TU Graz, June, 2010.

[26] E. Kozeschnik, *Modeling Solid-State Precipitation*, Momentum Press, New York, USA, **2012**.

[27] E. Kozeschnik, W. Rindler, B. Buchmayr, *Int. J. Mater. Res.* **2007** ,98, 826.

[28] C. Mesplont, *Doctoral Thesis,* Ghent University, **2002**.

[29] D. Simonovic, C.K. Ande, A.I. Duff, F. Syahputra, M.H.F. Sluiter, *Phys. Rev. B - Condens. Matter Mater. Phys.* **2010** , 81, 1.

[30] I. Timokhina, P. Hodgson, S.P. Ringer, R.K. Zheng, E.V. Pereloma, in: *Proc. Int. Conf. Microalloyed Steels: Processing, Microstructure, Properties and Performance*, (Eds: R.E. Ashburn, C.P. Brown, C.A. Davis, L.C. Oldham), Pittsburgh, Pennsylvania, **2007**, 305.

Paper II

Computational analysis of austenite film thickness and C-redistribution in carbide-free bainite

Philipp Retzl, Sabine Zamberger and Ernst Kozeschnik

Materials Research Express

Volume 8, Year 2021, 076502

Computational analysis of austenite film thickness and C-redistribution in carbide-free bainite

P. Retzl[1,3], S. Zamberger[2], E. Kozeschnik[1]

1 TU Wien, Institute of Material Science and Technology, Getreidemarkt 9, 1060 Wien, Austria

2 MatCalc Engineering GmbH, Gumpendorferstraße 21, 1060 Wien, Austria

3 Materials Center Leoben Forschung GmbH, Roseggerstraße 12, 8700 Leoben, Austria

Corresponding authors:

philipp.retzl@tuwien.ac.at

Abstract

In this work, a methodology for the computational analysis of some essential microstructural features of a bainitic microstructure is developed. The focus lies in the accurate prediction of the ferritic subunit size, the thickness of the residual austenite films, their corresponding C-enrichment and the accompanying stabilization of the residual austenite. Basis of the approach is the T_0-temperature concept in combination with the numerical simulation of C-diffusion profiles utilizing the cell diffusion module of the thermokinetic software package MatCalc. This methodology gives the opportunity to predict the C-distribution under consideration of consecutively forming subunits, which is necessary to estimate the C-content of austenite films. The simulations also take into account the effect of C trapping at the dislocations formed inside the ferritic platelets due to plastic deformation and its influence on the chemical potentials. Good agreement is achieved between measured and predicted retained austenite layer thickness and the C-enrichment of the layers accompanying the C redistribution process.

Introduction

Steels with a bainitic matrix have recently regained focus of steel-producing companies. Their special properties, on the one hand, and lean alloying concepts, on the other hand, which are in the region of low alloyed steel, make this material grade particularly interesting. However, bainite is probably the one steel microstructure where the discussion about the underlying phase transformation

mechanisms, i.e., the nucleation and growth of the ferritic subunits and the lengthening and thickening of the bainitic sheaves, is still very controversial [1].

The variants of bainitic microstructures are manifold and they depend on the combination of chemical composition and temperature in a complex manner. Knowledge about the geometry of the bainitic ferrite platelets, the thickness of the retained austenite films and their C-content as well as possible Fe-carbide precipitation in either the ferritic platelet or the retained austenite are of great importance in the development of new steel grades and the choice of adequate heat treatment parameters.

Since cost saving is a major aspect for steel industry, the aspired bainitic microstructure should be achievable by an overall chemical composition, which corresponds to that of a low alloyed steel grade. These alloys provide good weldability, which is an important factor for further processing of bainitic steel products [2][3]. In particular, the focus is on Transformation-Induced-Plasticity (TRIP)-aided steel. The TRIP-effect denotes the stress or strain-induced transformation of (residual) austenite to martensite and the accompanying plastic deformability.

TRIP steels achieve a superior combination of strength and formability [4][5]. Their microstructure consists of bainitic ferrite platelets (subunits) with C-enriched, thin austenitic films in between. A conglomerate of these subunits with the same orientation is called a bainite sheaf. Eventually, a certain amount of residual (blocky) austenite is also present in these microstructures, which does not transform into bainite during austempering [6]. Figure 1 shows schematically the structure of the described microstructure. The enrichment of carbon is generally higher in the film-like austenite due to its location between two bainitic ferrite platelets. Since the blocky austenite has a lower level of C-content and, therefore, less mechanical stabilization compared to the austenite films that are trapped between ferrite plates, it is more likely to transform to martensite at relatively small stresses or strains or during cooling to room temperature [7].

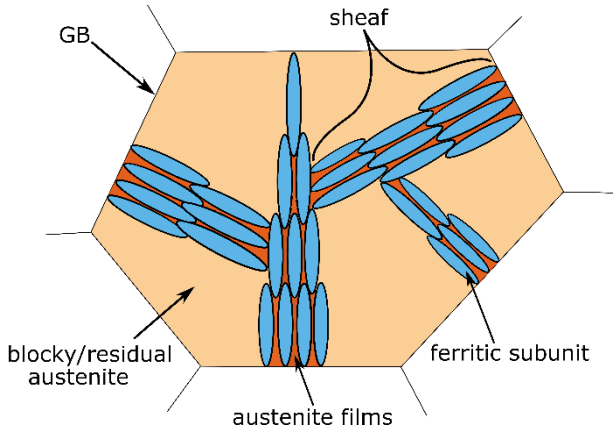

Figure 1: Schematic illustration of a carbide-free bainitic microstructure consisting of ferritic subunits, which build up sheaves, film-like austenite and areas of blocky/residual (=untransformed) austenite. Size scale is not accurate, since

austenite films are often some orders of magnitude smaller than blocky austenite areas. GB denotes austenite grain boundaries.

The brittle high-carbon martensite that forms at early stages of straining from blocky retained austenite can have negative effects on mechanical properties [8][9][10]. Films of retained austenite, which are more stable because of their higher carbon content and geometry, are potential microstructural features that improve toughness through the TRIP-effect [11][12][13][14]. Since the film-like retained austenite is a crucial part of the microstructure of many steels, which utilize the TRIP effect, it is important to understand the influence of temperature and composition on the properties of these features.

Chang and Bhadeshia [15] introduced a model that describes the thickness of austenite films based on the C diffusion profiles around the ferritic subunits. This approach was adopted by Li et al. [16] and further improved by adding a second subunit. While these models already deliver important insights into the distribution of C within a bainitic microstructure, they do not take into account important factors, which affect the C diffusion in this complex environment. In these models, the C diffusion is described with an analytical approach that does not consider factors, such as, the influence of C concentration on C diffusivity. Additionally other mechanisms, which influence the diffusion of C, like dislocation density and trapping of C, can be considered with the approach of this work as will be shown in the following sections. Especially at low temperatures, the effect of C trapping can have a major impact on the resulting C distribution. A better understanding of the evolution of C distribution in bainitic microstructures can help to improve mean field models, which describe the overall transformation kinetics of bainite. Mean field models often assume that the diffusion of carbon from supersaturated subunits into the surrounding austenite happens instantaneous or only describe it based on simple analytical approximations [17][18][19][20]. It is shown in Ref. [21] that a mean field approach that describes the effect of C diffusion within the bainitic microstructure with an empirical relation improves its ability to predict the bainite transformation kinetics. The approach proposed in this work therefore aims, among other things, to provide insights into the C distribution during bainitic transformations, which can be used to identify possible improvements in mean-field models.

The present work introduces a versatile modeling and simulation concept for carbide-free bainite, which is produced via an isothermal heat treatment at the so-called austempering temperature. The target is to simulate the metallurgical processes involved in the formation of the bainitic microstructure utilizing the T_0-concept as suggested by Bhadeshia [22] with thermodynamic and kinetic data from CALPHAD-type databases [23][24] as well as the diffusion module of the thermokinetic software package MatCalc [25], which is used for the numerical solution of the

diffusional C-redistribution between ferritic subunits and residual austenite films accompanying the formation of the bainitic microstructure. Trapping of C atoms at dislocations inside the ferritic platelets is fully taken into account in the simulations on basis of the model developed recently by Svoboda et al. [26][27][28] as well as utilized in the discussion of C-diffusion in the plastically deformed austenite surrounding the platelets.

Structure and thermodynamics of bainite

T_0-concept

The first step in the computational analysis of bainite formation is the estimation of the bainite start temperature during cooling from austenitization temperature. Although controversial hypotheses on the mechanism of bainite formation exist [1], the present authors assume that bainite formation is mostly a partitionless displacive transformation with the formation of a ferritic subunit in the first step, in accordance with the model suggested by Bhadeshia and Edmonds [6]. Any diffusional redistribution of C-atoms between ferritic platelet and residual austenite occurs only in a subsequent step, after the platelet formation has completed. For a comprehensive description of this topic, reference is made to Bhadeshia [22].

For the description of bainite nucleation, the T_0-concept is adopted. T_0 denotes the particular temperature where the transformation parent and product phases, i.e., austenite and ferrite, have identical free energy at identical chemical composition. Consequently, any partitionless phase transformation can occur only below this characteristic temperature [22]. Since the partitionless transformation from austenite to ferrite involves shear forces and a change in molar volume, a certain amount of mechanical energy must be expended to make the transformation commence. The corresponding amount of energy has been estimated to be in the order of 400 J/mol in an Fe-Ni-Si-C steel [29]. Depending on chemistry and the inherent strength of the parent austenite, this value can change and it is generally higher in higher strength alloys.

If this excess energy is taken into account in the T_0-concept, the actual transformation start temperature becomes T_0'. Figure 2 shows examples for calculated T_0 and T_0' curves for a steel with a classical TRIP-steel composition of 1.5 wt% of Si and Mn utilizing MatCalc with the corresponding thermodynamic and mobility databases [23].

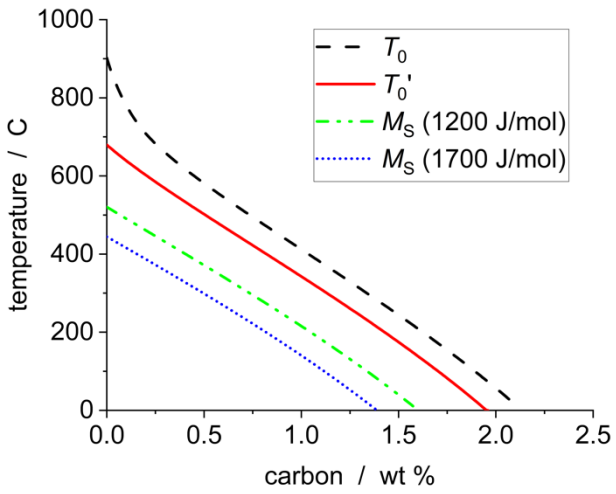

Figure 2: Calculated T_0, T_0' (400 J/mol) and martensite start (M_S) temperatures. Composition is 1.5 wt% Si and 1.5% Mn, balance is Fe.

In addition to predictions of the bainite start temperature, the T_0-concept also allows for some estimation of the bainite transformation stop conditions. Under certain circumstances, the growing bainitic sheaves, which represent groups of subunits with intermediate austenite layers, lead to a C-enrichment of the remaining untransformed austenite. According to this concept, Fig. 1 shows that the T_0'-temperature decreases with increasing C-enrichment in the austenite and, eventually, the bainite reaction comes to a stop before all parent austenite has transformed. This effect is often referred to as the "incomplete reaction phenomenon" [6][30][31].

In order to determine the stability of the residual austenite against a martensitic transformation during cooling to room temperature, it is important to have information also on the martensite start (M_S) temperature. Likewise the B_S temperature, which is given by the T_0' temperature, the value of M_S can also be estimated on basis of the T_0-concept. The major difference between the bainite and martensite transformations is that the latter is an entirely athermal reaction, i.e., it is independent of the cooling rate and it involves higher driving forces to initiate the transformation. Typical values for martensite driving forces in low alloy steels are in the order of 1200 to 1700 J/mol [32]. In higher alloyed steels, the necessary driving forces to initiate the martensite transformation can exceed these values substantially, however.

In Figure 3, M_S-temperatures are calculated via the T_0-concept and compared to different empirical equations for M_S-temperatures from literature [33][34][35][36]. Accordingly, a C-content between 1.3 and 1.4 wt% stabilizes austenite down to room temperature. For the bainite transformation, this

observation means that a minimum C level of approximately these values is necessary to stabilize the retained austenite films between the ferritic subunits.

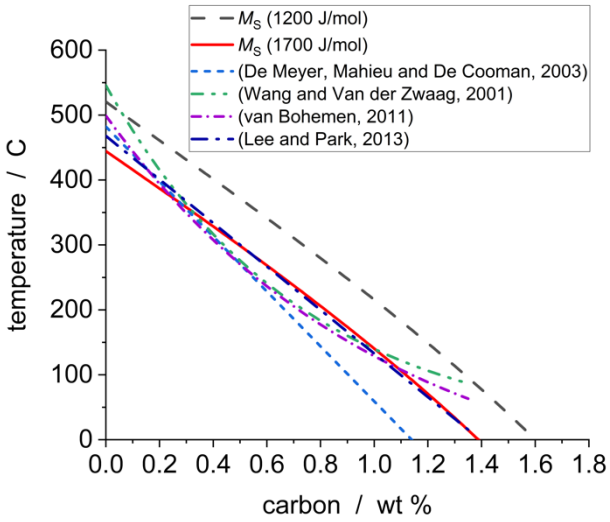

Figure 3: Comparison of M_S-temperatures calculated via the T_0-concept and empirical equations from literature (Composition: 1.5 wt% Si, 1.5 wt% Mn, balance Fe). Grain size for equation from Lee and Park, 2013, is chosen as 50 µm; [33][34][35][36].

The numerical model

In this section, the concepts of the numerical simulation strategy are outlined. According to Chang and Bhadeshia [15], the austenite film thickness is controlled by the diffusion field of C around a bainitic ferrite platelet into the surrounding residual austenite. This assumption has also been adopted by Li et al. [16] to calculate the C-enrichment between two bainite subunits.

In this manner, the present model is based on the assumption of a displacive formation mechanism of the bainitic ferrite plates (=subunits), with subsequent partitioning of the excess C from bainitic ferrite into the surrounding austenite as described by Bhadeshia [22]. According to this mechanism, C starts to diffuse out of the ferrite platelet, having a rather low solubility for C, into the austenite, having a comparably high C solubility. As a consequence, a C diffusion profile develops from the ferritic platelet into the residual austenite. Since C-diffusion is a thermally activated mechanism, this process takes time depending on the transformation temperature. The main feature of this concept is now that the austenite attached to the ferrite platelet develops a more or less steep concentration profile with the maximum being located at the ferrite/austenite interface (Figure 4).

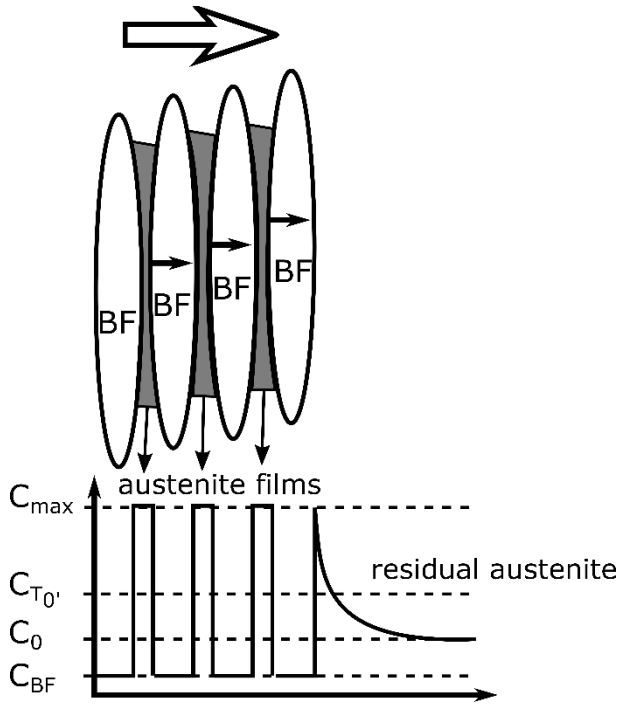

Figure 4: Sketch of the C-profile across retained austenite films and into the residual austenite.

According to the T_0'-concept, newly formed parallel subunits, which originate from the same sheaf, can approach the initial subunit during transformation only so close until the C-concentration of the residual austenite reaches the value given by the T_0'-temperature. Once the displacive transformation has stopped, the retained austenite film between the original and the new ferritic platelet absorbs C also from the new platelet (Figure 4). According to Chang and Bhadeshia [15] and Li et al. [16], the following assumptions can be employed:

i) C diffusion is only taken into account in the thickening direction of the bainitic subunits. Due to the significant lengthening of the bainite plates, other directions can be neglected.

ii) Subunits parallel to the initial subunit form as soon as the initial subunit is decarburized. This implies that the time between subunit formation is equal or higher than the time needed for decarburization of the initial plate.

iii) The adjacent subunit has the same size as the initial subunit.

iv) The time needed for a subunit to grow to its final size is comparably fast and can be neglected, i.e. subunits reach their final size almost instantaneously.

v) Precipitation of carbides in austenite and bainitic ferrite can be neglected (carbide-free bainite).

To apply the present model, the T_0' curve is first calculated to obtain the C content up to which a bainite platelet can form. Figure 5 shows an example of a T_0'-curve for a 0.4C-1.5Si-1.5Mn steel, where the critical carbon content at 400°C is marked.

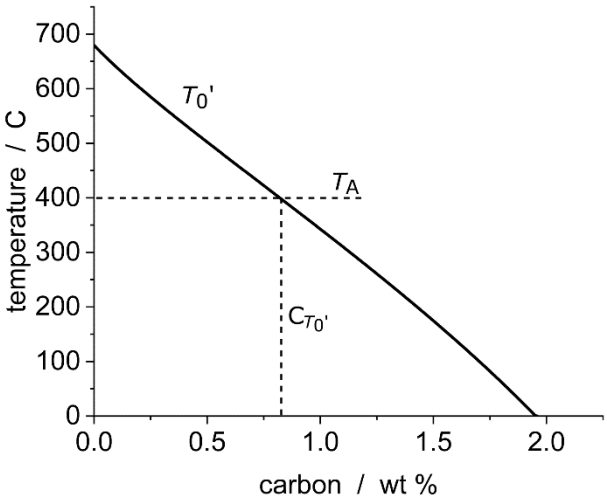

Figure 5: Calculated T_0'-curve for a 0.4C-1.5Si-1.5Mn (wt%) steel. T_A is the austempering temperature (400 C) and C_{T0}' is the C-content up to which an adjacent bainite platelet can grow.

The diffusion calculation is performed in a planar 1-D geometrical setup in the cell simulation module of MatCalc, which utilizes a finite differences scheme to calculate transient multi-component diffusion profiles. The evolution of carbon content in the individual cells after solving Fick´s law of diffusion implicitly is given by,

$$\left[1+\frac{D_{i,i+1}\Delta t}{(\Delta x)^2}+\frac{D_{i,i-1}\Delta t}{(\Delta x)^2}\right]c_i^{t+}-\frac{\Delta t}{(\Delta x)^2}\left[D_{i,i+1}c_{i+1}^{t+}+D_{i,i-1}c_{i-1}^{t+}\right]=c_i^t, \tag{1}$$

where c_i^t is the carbon content of cell i at the time t, and c_i^{t+} at the time $t+\Delta t$. $D_{i,i+1}$ is the mean diffusion coefficient of the cells i and $i+1$ and $D_{i,i-1}$ is the mean diffusion coefficient of the cells i and $i-1$. A system with N cells therefore is a linear equation system of N equations in N variables.

At phase boundaries, additionally a flux J due to differences in chemical potential μ is considered. This flux is given by,

$$J=\frac{Dc}{R_gT}\frac{\partial\mu}{dx}, \tag{2}$$

with D being the diffusion coefficient, c the concentration, x a 1D planar spatial coordinate and R_g the gas constant. In discretized form, the flux $J_{i,i+1}$ for cell i if a phase boundary exists between cell i and $i+1$ is then calculated by,

$$J_{i,i+1}=-\frac{D_{i,i+1}c_{i,i+1}}{R_gT}\frac{\mu_i-\mu_{i+1}}{|x_i-x_{i+1}|}, \tag{3}$$

where $D_{i,i+1}$ and $c_{i,i+1}$ are the arithmetic mean values of diffusion and carbon concentration of the cells i and $i+1$, $c_{i,i+1}$. The change of C concentration in cell i is then calculated with

$$\Delta c_i = \frac{J_{i,i+1} A_{i,i+1}}{V_i} \Delta t, \tag{4}$$

with $A_{i,i+1}$ being the area between cells i and $i+1$ and V_i being the volume of cell i. In our 1D simulation, the factor $A_{i,i+1}/V_i$ can be reduced to a division by the thickness of the cell. The change in concentration is added to equation 1 on the right hand side if a cell is located next to a phase boundary, i.e. if a neighboring cell has a different matrix phase. The diffusion coefficients for each cell are taken from the diffusion database mentioned earlier [23]. More details and use cases with this approach can be found in Ref. [37] and [38]. The effect of dislocation density and other factors on the diffusion coefficients of C will be described in later sections of this work.

A main advantage of this numerical cell diffusion approach over analytic approximations is that the C diffusivity in each cell is evaluated as a function of the current chemical composition, the dislocation density and temperature. Different geometrical configurations with a number of bainitic subunits can be studied easily and, finally, each cell can perform a fully coupled precipitation kinetics calculation to evaluate the simultaneous long-range diffusion of C and precipitation kinetics of carbides inside the ferritic platelet. The latter is not carried out in the present analysis since it is assumed that the investigated alloys are carbide-free, however, it will be in the focus of follow-up future work.

In the simulation, initially, the FCC_A1 (austenite) phase with a chemical composition corresponding to the nominal composition of the investigated alloy is assigned to each cell (t_0). In the process of formation of a ferritic platelet, the status of the transforming cells is instantaneously switched to the BCC_A2 (ferrite) phase. The interface between the two phases is assumed to be mechanically arrested and it remains stationary throughout the further simulations. The assigned phase and its composition define the chemical potential and diffusional mobilities of elements within each cell and, thus, the multi-component diffusion kinetics in the course of the elemental redistribution process. Additional microstructural properties, such as, the dislocation density, are likewise assigned and impact the simulation results. The size of the one-dimensional diffusion simulation box is chosen as 500 nm, which corresponds to the necessary size for representation of an entire C-profile over several ferritic platelets and the remaining residual austenite.

When the simulation is started, a certain number of cells, corresponding to the half-thickness of a bainite subunit, is switched from FCC to BCC on the left side of the simulation box. This choice is done due to symmetric boundary conditions on the left end. The simulation then runs until the ferrite platelet is depleted from C, but without equilibrating the carbon content of the austenite (t_1). At this moment, the simulation is interrupted, and the thickness of the austenite film is read from the

C-profile plot at the critical C-content as shown in Figure 6. The data in Figure 6 are taken from an example simulation for a 0.4 C - 1.5 Mn - 1.5 Si wt% steel.

Starting with this cell, additional right-neighboring cells, representing the full thickness of a new bainitic subunit, are changed from FCC to BCC and the diffusion simulation continues. The simulation is again interrupted, when the new ferrite platelet is depleted from C (t_2). The C-content of the layer between the two ferrite platelets is taken as calculated C-concentration of retained austenite films of the corresponding alloy at a given temperature. The described simulation steps and an example of the corresponding C-concentration profile is given in Figure 6. The temperature in this simulation is 400 C.

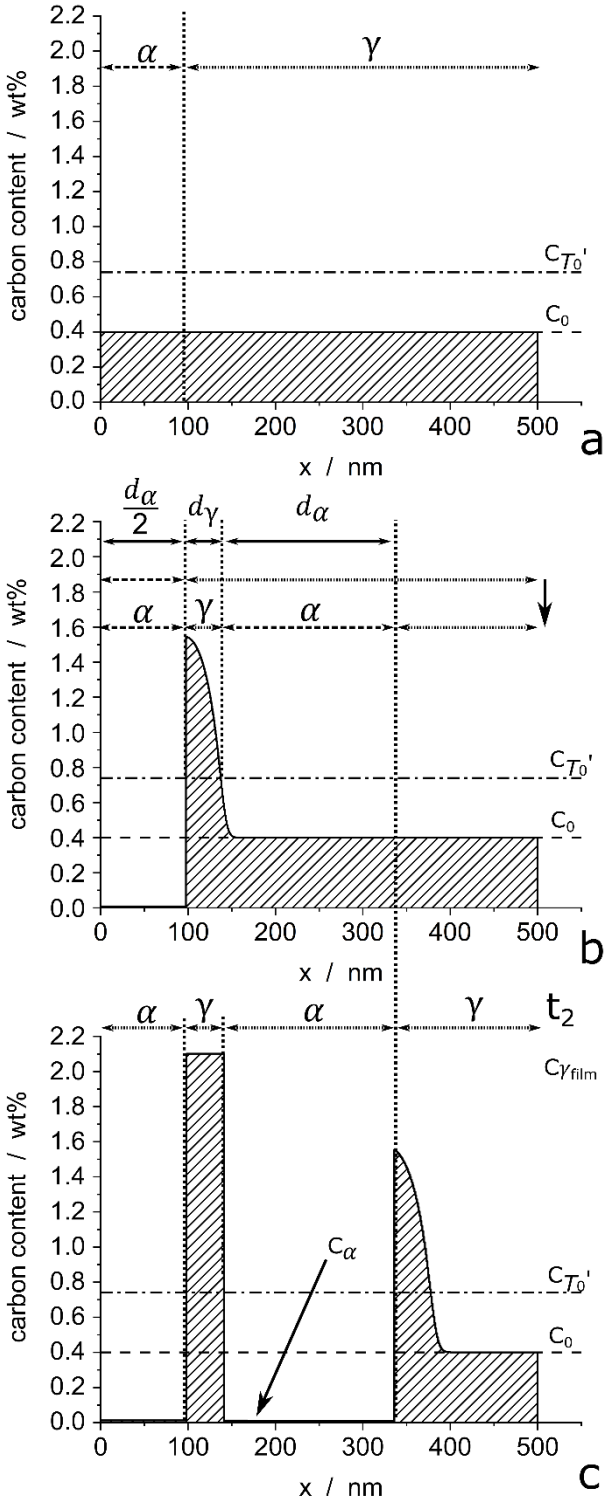

Figure 6: Scheme of the simulation steps for the cell diffusion calculation. a: t_0, initial state with nominal C-content, C_0, in all cells; b: t_1, carbon profile after decarburization of the ferritic bainite platelet (=subunit), another bainite platelet is inserted into the simulation; c: t_2, second bainite subunit has reached its equilibrium C-content; thickness of the austenite film d_γ, thickness of a bainite subunit d_α. C_α is the C-content of the ferritic subunits in equilibrium (~0.02)

Results

Austenite film thickness

The capabilities of the present model to predict the thickness of austenite films is first challenged on experimental data from Refs. [15] and [39]. Chang and Bhadeshia [15] have used these data in order to show that the austenite film thickness depends on the diffusion of C out of the ferritic bainite plates into the surrounding austenite. For these alloys, a full set of experimental data consisting of composition, bainite plate thickness, austenite film thickness and temperature are reported. Table 1 summarizes the composition of the investigated alloys. Composition, bainite plate thickness and temperature are used in the following as input parameters for the cell diffusion simulation, which delivers the austenite film thickness as a result.

Table 1: Composition of reference alloys [wt%]

Alloy	C	Si	Mn	Cr	Ni
A	0.27	1.98	2.18	1.9	0
C	0.46	2.1	2.15	0	0
E	0.1	1.77	2.12	0	2
H	0.1	1.63	1.99	1.97	0

Figure 7 compares the austenite film thicknesses as predicted by the present model and using the assumptions (i) to (v) made in the “Numerical model” section with measured values from the aforementioned references. Interestingly, the measured film thickness is systematically larger than the calculated one. A comparable trend has been observed in the original analysis by Chang and Bhadeshia [15], where a similar modelling approach has been used. According to these authors, this underestimation of film thickness could stem from the assumption that successive parallel bainitic subunits form as soon as the existing platelets reach their equilibrium C-content. This assumption is, in its nature, intuition-based rather than founded on sound metallurgical basis and it is further investigated, next.

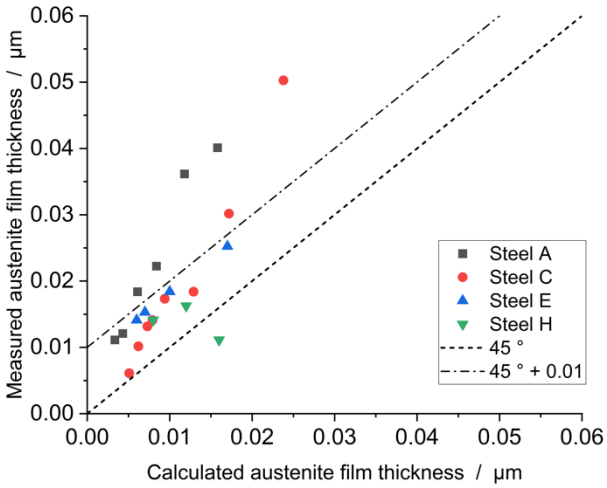

Figure 7: Measured and calculated austenite film thickness assuming nucleation of successive subunits to commence as soon as the first platelet has become depleted from C. Experimental data from ref. [15].

The present numerical simulations indicate that the depletion of a bainite subunit from C is a rather fast process, which is typically finished within the range of roughly 0.01 to 0.2 seconds, depending on temperature and thickness of the subunit. However, the time, which is required to progress the point of critical C content far enough into the remaining austenite to be in accordance with the experimental results for the austenite film thickness, is up to one order of magnitude longer. To analyze this observation in more detail, the diffusion simulations are run for extended times without the addition of a second bainite subunit to identify the point where the simulated film thickness is as close to the experimentally measured values as possible. Figure 8 illustrates the process of shift of the critical C-content with time and the resulting increase in austenite film thickness based on composition profiles of C for various isothermal holding times, exemplarily, for a 0.4C-1.5Si-1.5Mn (wt%) steel.

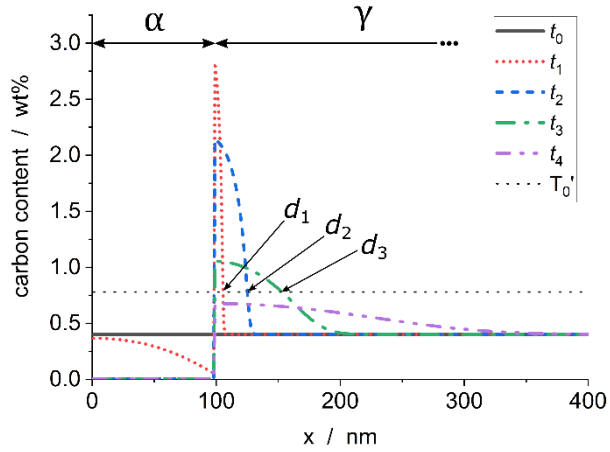

Figure 8: Calculated evolution of C-concentration profiles in the vicinity of a subunit. The locations of the critical carbon content (horizontal dashed line), d_i, correspond to the simulation times, t_i. While the predicted film thickness increases from t_0 to t_3, it decreases afterwards and, eventually, reaches zero again after longer simulation times.

In the beginning of the transformation, a sharp concentration peak for C is observed and the distance where the C-content corresponds to the calculated T_0'-temperature gradually moves into the parent austenite starting at the initial phase boundary. After a certain time, the peak of the C-distribution falls back below the critical C-content and a maximum possible film thickness exists for every alloy composition and temperature. To illustrate this behavior, the evolution of predicted film thickness for steels C and A, as determined by the T_0'-temperature, is exemplarily shown in Figure 9. For steel C, this distance moves into the parent austenite, reaches a maximum at roughly 70 nm at 430 C and then moves back to zero. Since the experimentally observed thickness is at around 50 nm, the "optimum" time corresponding to this particular thickness can be read straightforwardly from the diagram. The same is performed for a temperature of 260 C, where the experimentally measured value is roughly 6 nm and the maximum calculated thickness is around 10 nm. For steel A, however, the predicted maximum thicknesses of roughly 6nm and 28 nm never reach the experimentally ones of 11 nm and 40 nm, neither at 400 C nor at 300 C.

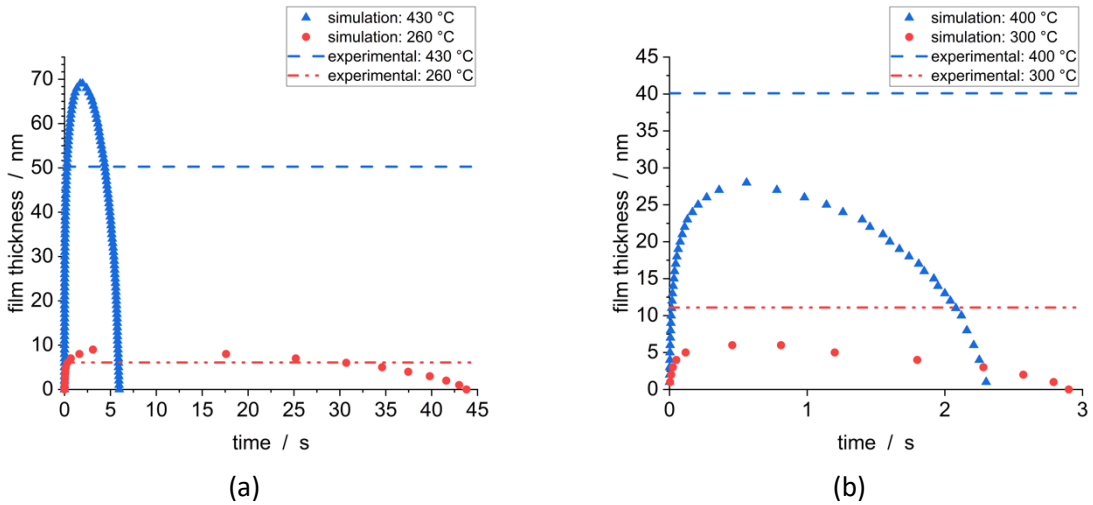

Figure 9: Evolution of austenite film thickness with time, illustrated as position of the T_0' limit during C-redistribution from the ferritic platelet into the austenite film. (a) Steel C; (b) Steel A. Horizontal lines represent experimentally measured austenite film thicknesses.

Figure 10 compares calculated austenite film thicknesses with literature data based on these "optimum" times for the formation of the next parallel subunit (t_{nsu}). Apparently, only for steel C, the calculations can match the experimental values exactly. For all other experimental data, the agreement can be made better but not perfect. One source for this discrepancy might be sought in the assumptions (i) to (v) defined earlier. Another source might be the possible enrichment of untransformed austenite regions that can become enriched in C. Consequently, bainite subunits that form in the beginning of the reaction can experience lower C-contents compared to subunits formed towards the later stages of the bainite transformation. The simulations, however, always refer to the

initial C-content of the austenite. And, finally, another source might be present in simulation input parameters, which govern the evolution of C-profile in the residual austenite and, therefore, also the austenite film thickness. The most relevant parameter, in this context, is the diffusivity of C as a function of the microstructural state parameters stress, defect concentration (i.e. dislocation density) and C-content of the austenite. These factors are discussed in the following section.

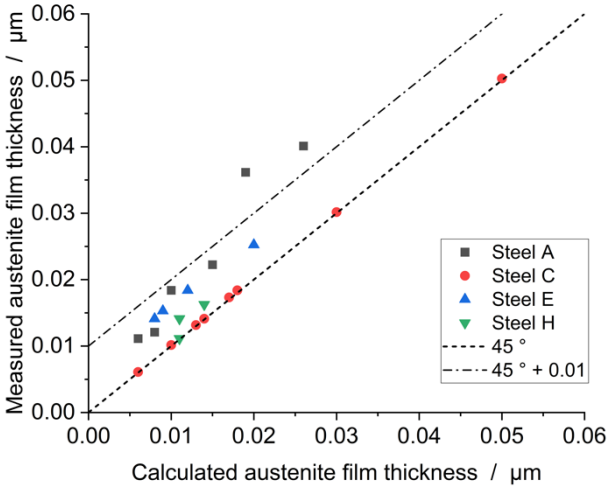

Figure 10: Comparison of measured and calculated austenite film thickness, with "optimized" times for formation of the second bainitic subunit. Experimental data from ref. [15]

Influence of elastic lattice stress on diffusivity

When a ferritic platelet forms, the molar volume of the new phase is larger than the molar volume of the surrounding parent austenite by roughly 1 % [40]. Following the analysis of the deformation and stress state of a spherical inclusion in Ref. [41], a positive volumetric misfit between ferritic platelet and austenite matrix shall cause compressive stress in normal direction and tensile stress in tangential direction to the surface of the inclusion. In a first approximation, this observation should also hold for an ellipsoidal inclusion and a tensile stress field should prevail around a subunit normal to the C diffusion direction. This expansion of the austenite lattice leads to an enhancement of C diffusion in the normal of the subunit surface, which is quantified next.

In Ref. [42], the influence of the C-content on the diffusivity of C is analyzed and it is concluded that the effect of increasing diffusivity with increasing C content can be most accurately described with Asimow's model [43]. This approach assumes that the faster C diffusion is induced by a lattice parameter expansion caused by interstitially dissolved C. To approximate the effect of stress on the diffusivity, in a rough estimation, it is assumed that the increase of the lattice parameter due to elastic stress has a comparable impact on the C-diffusivity as an increase of the lattice spacings due to dissolved C in the austenite matrix.

Due to the volumetric misfit, during transformation, both, the ferritic platelet and the surrounding austenite, are plastically deformed [44] and the amount of stress in the austenitic matrix corresponds roughly to its yield strength. This value, σ_y, can be estimated by the empirical equation proposed by Eres-Castellanos et al. [45] as

$$\sigma_y = (52.3 + 47.0X_C + 31.3X_{Si} + 1.0X_{Mn} + 1.0X_{Cr} + 31.3X_{Mo} + 1.3X_{Ni} + 10.7X_V + 3.8X_{Al} + 16.8X_{Cu} + 15.2X_{Ti} + 53)\left(1 + 0.001\ln\left(\frac{\dot{\varepsilon}}{0.001}\right)\right) * \left(1 - \left(\frac{T_r}{1487-25}\right)^{0.658}\right), \quad (5)$$

with X_i being the concentration of element i in at-%, $\dot{\varepsilon}$ the strain rate and T_r the temperature difference to room temperature (25 °C). The experimental data that was used to derive this empirical relation covers composition and temperature ranges of the reference steels that are investigated. Therefore, a reasonable approximation of the yield strength in the context of the presented approach should be possible. A comparison of calculated and experimental values for the yield strength of various steels at different temperatures and other empirical equations are extensively discussed by Eres-Castellanos et al. in Ref. [45]. The strain rate is approximated with 1000 s^{-1} and the Youngs modulus is taken as the one used in the MatCalc simulations for the FCC_A1 phase with $E = (193000 - 73.33 \cdot T) \cdot 10^6$ and T inserted in °C. The resulting average expansion of the lattice $\varepsilon_{lattice}$ can be calculated using Hooke's law $\sigma_y = E\varepsilon$ with roughly 0.13 to 0.16 %.

The equation describing the lattice parameter of austenite depending on carbon concentration from Dyson and Holmes [46] is

$$a_\gamma = 3.5780 + 0.033w_C \quad (6)$$

with a_γ being the lattice parameter of austenite and w_C being the C-content in wt-%. According to equation 6, about 0.14 to 0.17 wt-% of C are necessary for the same lattice expansion as calculated above. This carbon equivalent is used to evaluate the effect of stress on the diffusion of carbon. The dependence of diffusivity on carbon concentration is taken from Agren et al. [47], who provided a corresponding equation as

$$D_C = 4.53 \cdot 10^{-7}\left(1 + y_c(1 - y_c)\frac{8339.9}{T}\right)\exp\left(-\left(\frac{1}{T} - 2.221 \cdot 10^{-4}\right)(17767 - 26436y_c)\right) \quad (7)$$

, with the composition variable $y_c = X_C/(1 - X_C)$, where X_C is the mole fraction of carbon. According to the results of this approximation, the diffusivity of C in the austenite matrix is increased by a factor depending on temperature and composition. Figure 11 shows the factor by which the C diffusion is increased depending on temperature for the reference steels.

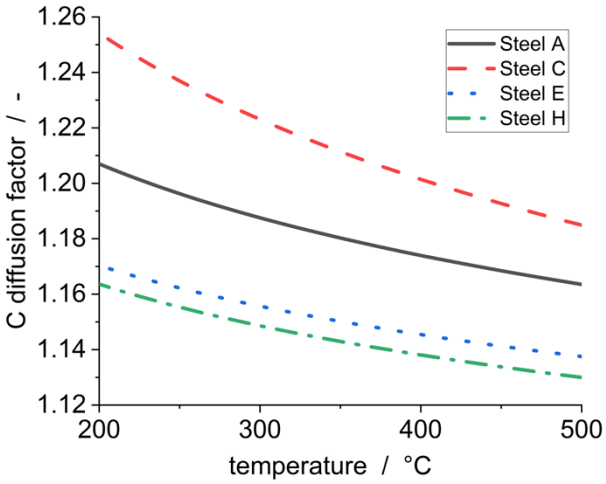

Figure 11: Factor by which the C diffusion is enhanced for Steels A, C, E and H depending on temperature according to the approach described in this section.

Influence of dislocation density on diffusivity

The plastic deformation of the austenite surrounding the ferritic subunit induces an increased dislocation density and, thus, increases the effective C diffusion kinetics through the mechanism of pipe diffusion. This effect is fully taken into account in the current simulations as [48]

$$D_{\mathrm{eff}} = D_0 \cdot (1 - \alpha_{\mathrm{disl}}) + D_{\mathrm{p}} \cdot \alpha_{\mathrm{disl}} \tag{8}$$

with the effective diffusion coefficient, D_{eff} , D_0 being the diffusion coefficient in the undisturbed crystal, D_{p} being the diffusion coefficient along the dislocation core and α_{disl} being the volume fraction of dislocation cores, which is calculated as,

$$a_{\mathrm{disl}} = \pi R_{\mathrm{core}}^2 \cdot \rho, \tag{9}$$

with R_{core} being the radius of the dislocation core, which is assumed to be 0.5 nm, and ρ being the dislocation density. The equation describing the diffusion of C along a dislocation core is,

$$D_{\mathrm{p}} = D_0 \cdot \exp\left(\frac{Q_{\mathrm{DC}}}{R_{\mathrm{g}} T}\right), \tag{10}$$

where Q_{DC} is 29.2 kJ/mol [48] and R_{g} is the Universal Gas Constant.

Measurements from Cornide et al. [49] suggest that the dislocation density in austenite surrounding a ferritic subunit is similar to the dislocation density within the subunit. Therefore, it is reasonable to utilize data on the number of dislocations within the subunit to estimate, or at least give an upper boundary for, the amount in austenite. Takahashi and Bhadeshia [50] propose an empirical equation for the upper limit of dislocations in bainite in the temperature range of 473-942 K as

$$\log_{10}\rho_{\mathrm{d}} = 9.28480 + \frac{6880.73}{T} - \frac{1780360}{T^2}, \tag{11}$$

with ρ_{d} being the dislocation density per m^2 and T being the temperature in Kelvin. This equation is describing the experimental data, which was used to develop it quite well, but due to its mathematical structure it predicts a decrease in dislocation density below 245 °C without physical evidence for this effect according to the underlying experimental data. Therefore, an alternative equation is proposed in order to reproduce the same experimental data, but with monotonically decreasing behavior in the relevant temperature region. After fitting several equation types to the experimental data by the method of least squares an equation with the structure of the probability density of a normal distribution was chosen. It achieved the best results, i.e. least mean square errors, while ensuring that there is no decrease of calculated dislocation density down to 0 °C. The resulting empirical equation is,

$$\rho_{\mathrm{d}} = 7 \cdot 10^{15} \cdot \frac{1}{0.28\sqrt{2\pi}} \cdot e^{-\frac{1}{2}\left(\frac{T_{\mathrm{C}}}{280}\right)^2}, \tag{12}$$

with T_{C} being the temperature in °C. This equation is compared to the experimental data and equation 11 from Ref. [50] in Figure 12.

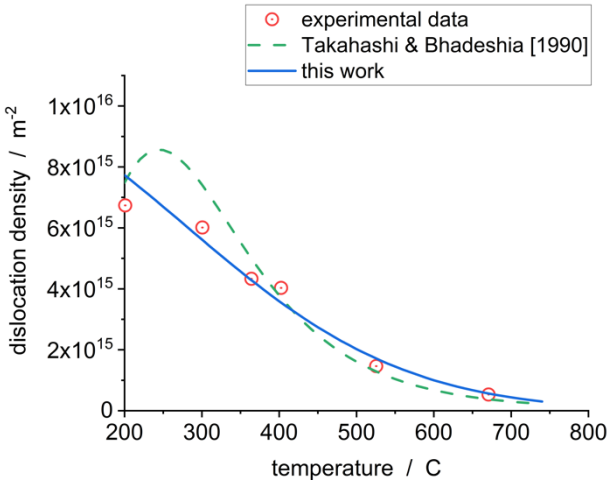

Figure 12: Empirical equations (11) and (12) together with experimental data from Ref. [50].

Impact of carbon diffusivity

The time for the second ferritic subunit to from in order to obtain “optimum” simulation results strongly depends on the diffusivity of C. Different aspects influencing C diffusion are discussed in the previous sections. The optimized times until the next subunit forms (t_{nsu}), for different approaches for the effective C diffusion coefficient, are illustrated in Figure 13. The approach designated as “low dislocation density” assumes a fixed dislocation density of 10^{13} m^{-2} in austenite, which results in relatively low ‘excess’ C diffusivity and, therefore, longer times until the calculated film thickness is as

close as possible to the experimentally obtained values. The points named “with lattice stress” represent simulations, which take into account the effect of stress in the lattice, while still the fixed dislocation density of 10^{13} m^{-2} is applied. “High dislocation density” designates the simulations where the dislocation density in austenite is approximated by equation 12, resulting in the highest C diffusivity. Exponential functions are fitted to the corresponding data points, which can be used as input parameters for further simulation studies with the present approach.

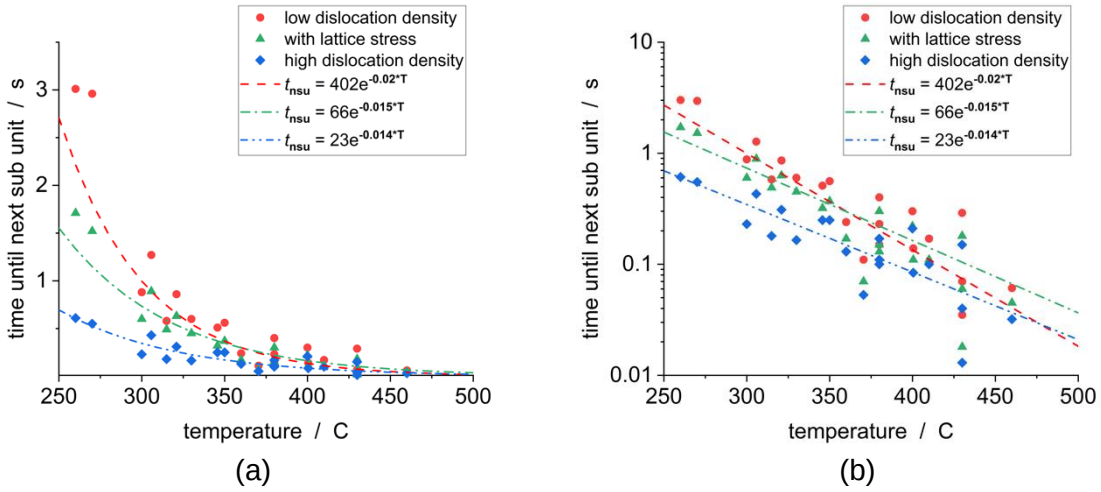

Figure 13: Time until an adjacent bainite subunit forms in order to get best agreement between calculated and measured austenite film thicknesses; a: linear y-scale; b: log y-scale

One implication of these empirical relations is that the nucleation/formation of an adjacent subunit needs more time at lower temperatures. This does not necessarily mean that the overall reaction kinetics become slower with decreasing temperature, but only that the thickening rate of single sheaves decreases with decreasing temperature. The phenomenon of longer times for the formation of the second subunit becomes less pronounced when effects that increase the carbon diffusivity are considered. Especially, the influence of dislocations decreases the increase in t_{nsu}, since the dislocation density increases with decreasing temperature.

For the following simulation studies, the “high dislocation density” model is used, since there exists the aforementioned evidence of high dislocation densities in austenite around ferritic bainite subunits and a smaller increase in t_{nsu} when compared to the other models. Since the effect of stress is much less pronounced than the effect of dislocation density, only the latter effect is considered. The function that is used in the following simulation studies for the time until the next ferrite plate forms is

$$t_{\mathrm{nsu}} = 23\ \exp^{-0.014*T}, \tag{13}$$

with *T* inserted in °C.

General predictions of the model

To derive general trends from the present model, an example composition of 1.5 Mn-1.5 Si (wt%) with varying C concentrations is chosen because it represents a standard alloying concept for TRIP-assisted bainitic steels. To the knowledge of the authors, small changes in the composition of substitutional elements should not change the overall behavior to a decisive degree and the derived trends should, therefore, be valid for a broader selection of alloys, which undergo the bainite transformation as long as the formation of carbides in austenite is sufficiently suppressed.

The size of the bainitic ferrite plates is calculated by the formula given in ref. [51]. It was originally developed by Parker [52], who empirically modelled the subunit thickness, d_{b}. Parker assessed the data of steels with C-contents between 0.095 and 0.5 wt% in a temperature range between 523 and 773 K and obtained

$$d_{\mathrm{b}} = 2 \cdot 10^{-7} \cdot \frac{T-528}{150}\ [m]. \tag{14}$$

Figure 14 illustrates the trends for thickness and C-content of austenite films for the aforementioned composition with 0.2 and 0.4 wt% of C as predicted by the present simulations. The film thickness increases with increasing temperature and C content in the austenite matrix, whereas the C-concentration in the retained austenite varies only to a rather limited degree. According to the calculated and empirical martensite start temperatures in Figure 3, the amount of C in the austenite films of both alloys is sufficient to stabilize them at room temperature against martensitic transformation.

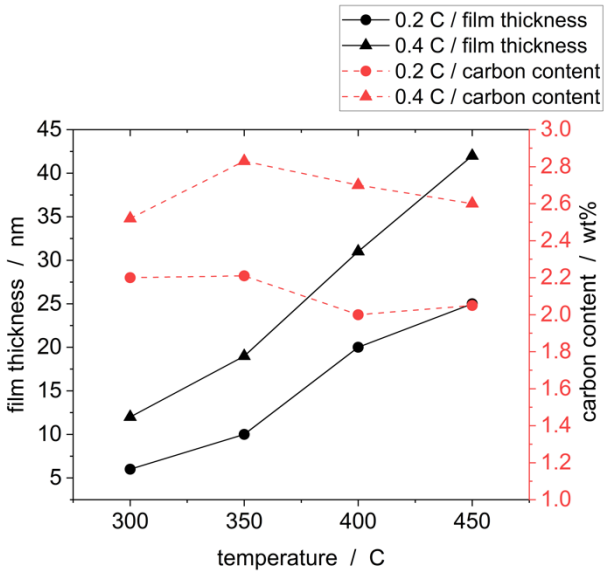

Figure 14: Predicted austenite film thickness and C-concentration within the austenite films for 0.2 wt% and 0.4 wt% matrix carbon concentration, respectively.

Due to the lack of data available in literature, it is difficult to put the predicted trends of the present simulations into a quantitative context. Data from reference [53] show a C content of ~1.8-2.2 wt% in austenite films for a 0.39C - 4.09Ni - 2.05Si wt% alloy a at a transformation temperature of 400 °C. For an initial C content of 0.4 wt% the current model predicts C levels in the films of ~2.6 wt%. The simulation gives the C content of films at the moment of their formation. It is possible that C diffuses out of the films and into the surrounding blocky austenite areas over time. This can happen, albeit slowly, because the austenite films can be connected to the blocky austenite on their narrow sides. Since in experimental setups the C concentration in films is measured at a point where a lot of films already exist for some time, lower values are expected when compared to this kind of simulation.

Austenite films at low temperatures

At low bainite transformation temperatures, trapping of C atoms at defects becomes an important effect, which needs to be accounted for in the diffusion simulation. For instance, in “nano-scale” bainite, which forms at approximately 200 °C and below [54][55], the strongly deformed ferrite platelets can bind substantial amount of C in stable solid solution at the dislocations. This C is unavailable for diffusion into and stabilization of the austenite films. The C-content of fresh martensite at 200 °C can be as high as 0.2 wt%, depending on the actual dislocation density [56], the trapping of C in bainitic ferrite is experimentally confirmed by X-ray and atom probe measurements [54] [57].

The effect of trapping is incorporated in the present simulations with the approach introduced by Svoboda et al. [26][27][28]. The trapping enthalpy, ΔE, and coordination number, *c*, are the main input parameters for this model. These are chosen as ΔE= 75000 – 20*T [J/mol] and $c=A/T^2$, with the coefficient $A=10^6$, as suggested by Mayer et al. [58].

In ref. [55], atom probe measurements of a bainitic microstructure consisting of ferritic bainite plates and austenite films, which formed at 200 °C, are reported. The bainite subunit thickness and location in the simulation is taken from the original source [55]. It is assumed that the thicker subunit formed first and the thinner one afterwards. Due to the smaller overall dimensions of the transformation observed experimentally, the size of the simulation box is defined with 140 nm. The dislocation density is taken as $3 \cdot 10^{15}$ m^{-2}, based on measurements in the range between 200 and 350 °C for this steel [59].

Figure 15 compares the measured and calculated carbon profiles over two ferrite platelets. The calculated thickness and carbon content of the austenite film between the bainitic ferrite plates is in good agreement with the APT measurements. The C content within the ferritic part of the microstructure seems to be slightly overestimated by the current trapping model, although some areas in the second subunit even exceed the carbon concentration as predicted by the model. The areas to the left of the initial subunit and to the right of the second one cannot be compared to the experimental results since the information about the surroundings, i.e., where is the next ferritic platelet is located, is missing in the simulation.

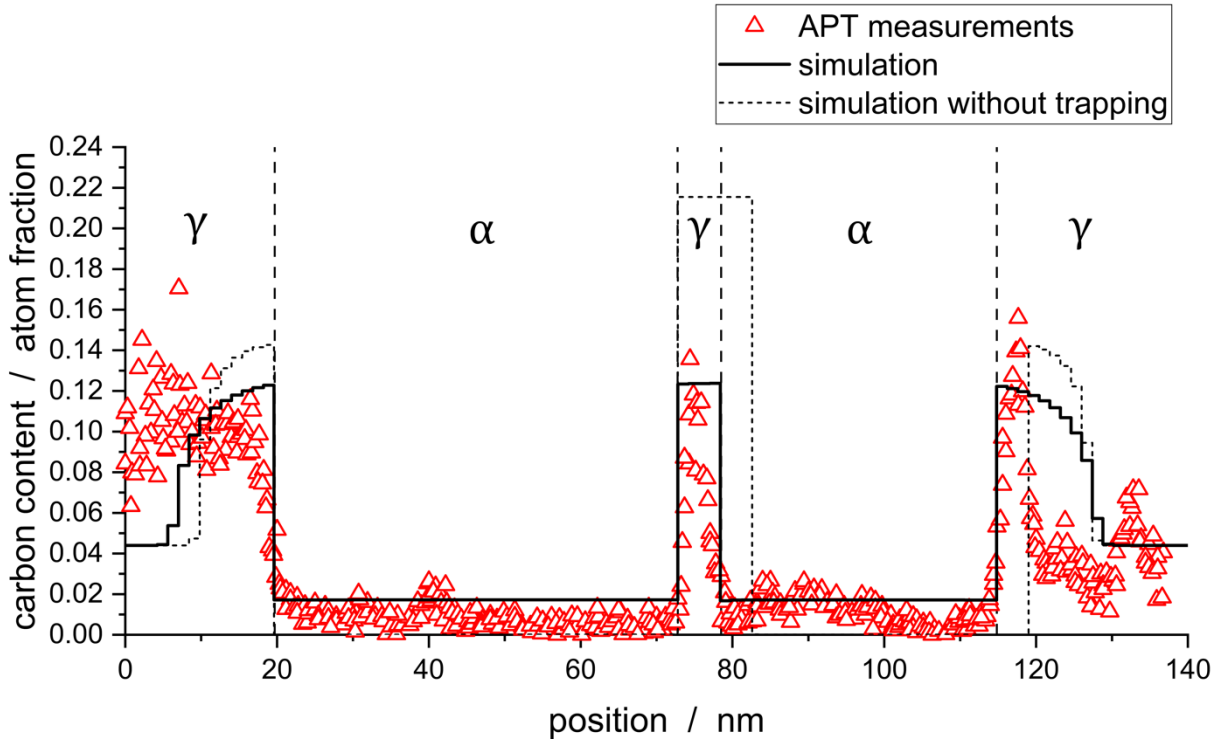

Figure 15: Simulation of bainite formation at 200 °C, with and without trapping taken into account. APT measurements from ref. [55]

Bainite, which forms at temperatures as low as 200 °C, commonly occurs in the form of lower bainite, where carbide particles form within the bainitic ferrite subunits in competition with the C diffusion into the surrounding austenite [50]. According to Caballero and Bhadeshia [54], however, practically no carbides were found in similar steels although extensive TEM (transmission electron microscopy) investigations were performed. On the other hand, atom probe investigations from Ref. [59] reveal, that very small carbide particles may exist in the investigated steel. However, according to Ref. [59], the influence of carbide precipitates on the carbon distribution in the microstructure is extremely small. Therefore, neglecting them should have only a minor influence on the results of the simulations presented. It should be noted that for other compositions, carbide precipitation reactions could have a more pronounced effect and, therefore, should be considered in these cases. Corresponding modeling and simulation work is in process, however, will be reported elsewhere because carbide precipitation introduces additional complexity, which is exceeding the scope of the present manuscript.

Summary and conclusions

In the present work, a model for the simulation of austenite film thickness and carbon distribution in a bainitic microstructure is introduced. It is based on Chang and Bhadeshia's [15] idea that the austenite film thickness depends on the carbon diffusion profile around the bainitic ferrite plates. The ability to describe the evolution of carbon concentration profiles in the presence of multiple subunits is one of the main features of our model. Consequently, this approach provides a more complete description of diffusion processes within bainite sheafs compared to simple analytical approaches because these often neglect important factors, such as, the influence of C concentration on C diffusivity. Furthermore, it is shown that the effects of stress and dislocation density on the diffusion of C can be considered with this method. Carbon trapping at dislocations, which plays an increasing role at decreasing transformation temperature, is accounted for by the presented model. Thus, carbon concentration profiles for bainitic microstructures that form at low temperatures (nanoscale bainite) can be consistently reproduced. Therefore, the presented model can be used to study trends in carbon concentration and size of retained austenite films for a broad variety of steels and over a wide range of temperatures.

Acknowledgement:

The authors gratefully acknowledge the financial support under the scope of the COMET program within the K2 Center “Integrated Computational Material, Process and Product Engineering (IC-MPPE)” (Project No 859480). This program is supported by the Austrian Federal Ministries for Climate Action, Environment, Energy, Mobility, Innovation and Technology (BMK) and for Digital and Economic Affairs (BMDW), represented by the Austrian research funding association (FFG), and the federal states of Styria, Upper Austria and Tyrol.

References

[1] L. C. D. Fielding 2014 The Bainite Controversy *Mater. Sci. Technol.* **29** 383–399

[2] N. Yurioka 2001 Physical Metallurgy Of Steel Weldability *ISIJ Int.* **41** 566–570

[3] Ş. Talaş 2010 The assessment of carbon equivalent formulas in predicting the properties of steel weld metalsn*Mater. Des* **31** 2649–2653

[4] B. C. De Cooman 2004 Structure-properties relationship in TRIP steels containing carbide-free bainite *Curr. Opin. Solid State Mater. Sci.* **8** 285–303

[5] D. Krizan 2006 TRIP STEELS: ADVANCED HIGH STRENGTH MULTIPHASE STEELS FOR AUTOMOTIVE APPLICATIONS *14th International Scientific Conference CO-MAT-TECH*

[6] H. K. D. H. Bhadeshia and D. V. Edmonds 1980 Mechanism of Bainite Formation in Steels *Acta Metall.* **28** 1265–1273

[7] H. K. D. H. Bhadeshia and D. V. Edmonds 1983 Bainite in silicon steels: new composition–property approach Part 1 *Met. Sci.* **17** 411–424

[8] T. George, E. R. Parker, and R. O. Ritchie 2014 Susceptibility to hydrogen attack of a thick-section 3Cr–1 Mo–1 Ni pressure-vessel steel-role of cooling rate *Mater. Sci. Technol.* **1** 198–208

[9] R. M. Horn and R. O. Ritchie 1978 Mechanisms of tempered martensite embrittlement in low alloy steels *Metall. Trans. A* **9**1039–1053

[10] H. K. D. H. Bhadeshia and D. V. Edmonds 1983 Bainite in silicon steels: new composition–property approach Part 2 *Met. Sci.* **17** 420–425

[11] X. D. Wang, B. X. Huang, Y. H. Rong, and L. Wang 2006 Microstructures and stability of retained austenite in TRIP steels *Mater. Sci. Eng. A* **438–440** 300–305

[12] M. Y. Sherif, C. G. Mateo, T. Sourmail, and H. K. D. H. Bhadeshia 2004 Stability of retained austenite in TRIP-assisted steels *Mater. Sci. Technol.* **20** 319–322

[13] K. Sugimoto, M. Misu, M. Kobayashi, and H. Shirasawa 1993 Effects of Second Phase Morphology on RetainedAustenite Morphology and Tensile Properties in a TRIP-aided Dual-phase Steel Sheet *ISIJ Int.* **33** 775–782

[14] A. Z. Hanzaki, P. D. Hodgson, and S. Yue 1997 Retained austenite characteristics in thermomechanically processed Si-Mn transformation-induced plasticity steels *Metall. Mater. Trans. A*, **28A** 2405–2414

[15] L. C. Chang and H. K. D. H. Bhadeshia 1995 Austenite films in bainitic microstructures *Mater. Sci. Technol.* **11** 874–882

[16] S. Li, R. Zhu, I. Karaman, and R. Arróyave 2013 Development of a kinetic model for bainitic isothermal transformation in transformation-induced plasticity steels *Acta Mater.* **61** 2884–2894

[17] A. M. Ravi, J. Sietsma, and M. J. Santofimia 2016 Exploring bainite formation kinetics distinguishing grain-boundary and autocatalytic nucleation in high and low-Si steels *Acta Mater.* **105** 155–164

[18] S. M. C. Van Bohemen and D. N. Hanlon 2012 A physically based approach to model the incomplete bainitic transformation in high-Si steels *Int. J. Mater. Res.* **103** 987–991

[19] M. J. Santofimia, F. G. Caballero, C. Capdevila, C. García-Mateo, and C. G. De Andrés 2006 New

model for the overall transformation kinetics of bainite. Part 1: The model *Mater. Trans.* **47** 2465–2472

[20] M. Azuma, N. Fujita, M. Takahashi, and T. Lung 2003 Modelling upper and lower bainite trasformation in steels *Mater. Sci. Forum* **45** 221-228

[21] W. Wei, P. Retzl, E. Kozeschnik, and E. Povoden-karadeniz 2021 A semi-physical α-β model on bainite transformation kinetics and carbon partitioning *Acta Mater.* **207** 116701

[22] H. K. D. H. Bhadeshia 2015 *Bainite in Steels, 3rd ed*. Leeds Maney Publishing

[23] Erwin Povoden-Karadeniz 2020 *mc_fe.tdb (version 2.060) and mc_fe.ddb (version 2.012)* Institute of Materials Science and Technology TU Wien Austria

[24] H. L. Lukas, S. G. Fries, and B. Sundman 2007 *Computational thermodynamics: The Calphad method* Cambridge Cambridge University Press

[25] MatCalc, The Materials Calculator, http://www.matcalc.at (accessed: February 2021)

[26] J. Svoboda, Y. V. Shan, E. Kozeschnik, and F. D. Fischer 2013 Determination of depths of traps for interstitials from thermodynamic data: A new view on carbon trapping and diffusion *Model. Simul. Mater. Sci. Eng.* **21** 065012

[27] J. Svoboda and F. D. Fischer 2012 Modelling for hydrogen diffusion in metals with traps revisited *Acta Mater.* **60** 1211–1220

[28] F. D. Fischer, J. Svoboda, and E. Kozeschnik 2013 Interstitial diffusion in systems with multiple sorts of traps *Model. Simul. Mater. Sci. Eng.* **21** 025008

[22] H. K. D. H. Bhadeshia 1981 A rationalisation of shear transformations in steels *Acta Metall.* **29** 1117–1130

[30] H. K. D. H. Bhadeshia and J. W. Christian 1990 Bainite in Steels *Met. Trans. A* **21A** 767-797

[31] H. K. D. H. Bhadeshia and A. R. Waugh 1982 Bainite: An atom-probe study of the incomplete reaction phenomenon *Acta Metall.* **30** 775–784

[32] Z. Jicheng and Z. Jin 1990 THERMODYNAMICS OF THE MASSIVE, BAINITIC AND MARTENSITIC TRANSFORMATIONS IN Fe-C, Fe-Ni, Fe-Cr AND Fe-Cu ALLOYS," *Acta Met. Mater.* **38** 425–431

[33] S. M. C. van Bohemen 2011 Bainite and martensite start temperature calculated with exponential carbon dependence *Mater. Sci. Technol.* **28** 487–495

[34] S. J. Lee and K. S. Park 2013 Prediction of martensite start temperature in alloy steels with different grain sizes *Metall. Mater. Trans. A* **44** 3423–3427

[35] J. Wang and S. Van der Zwaag 2001 Stabilization mechanisms of retained austenite in transformation-induced plasticity steel *Metall. Mater. Trans. A* **32** 1527–1539

[36] M. De Meyer, J. Mahieu, and B. C. De Cooman 2003 Empirical microstructure prediction method for combined intercritical annealing and bainitic transformation of TRIP steel *Mater. Sci. Technol.* **18** 1121–1132

[37] Y. V. Shan, M. Soliman, H. Palkowski, and E. Kozeschnik 2021 Modeling of Bake Hardening Kinetics and Carbon Redistribution in Dual-Phase Steels *Steel Res. Int.* **92** 2000307

[38] Mas F. 2015 Doctoral thesis University Grenoble Alpes

[39] S. B. Singh and H. K. D. H. Bhadeshia 1998 Estimation of bainite plate-thickness in low-alloy steels *Mater. Sci. Eng. A* **245** 72–79

[40] H. K. D. H. Bhadeshia, S. A. David, J. M. Vitek, and R. W. Reed 1991 Stress induced transformation to bainite in pressure vessel steel *Mater. Sci. Technol.* **7** 686–698

[41] F. D. Fischer and E. R. Oberaigner 2000 Deformation, Stress State, and Thermodynamic Force for a Transforming Spherical Inclusion in an Elastic-Plastic Material *Int. J. Plast.* **67** 793–796

[42] X. Gu, G. M. Michal, F. Ernst, H. Kahn, and A. H. Heuer 2014 Concentration-dependent carbon diffusivity in austenite *Metall. Mater. Trans. A* **45** 3790–3799

[43] R. M. Asimow 1964 Analysis of variation of the diffusion constant of carbon in austenite with concentration *Trans. AIME* **230** 611–613

[44] H. K. D. H. Bhadeshia and D. V. Edmonds 1979 The bainite transformation in a silicon steel," *Metall. Trans. A* **10** 895–907

[45] A. Eres-Castellanos, I. Toda-Caraballo, A. Latz, F. G. Caballero, and C. Garcia-Mateo 2020 An integrated-model for austenite yield strength considering the influence of temperature and strain rate in lean steels *Mater. Des.* **188** 108435

[46] D. DYSON and B. Holmes 1970 Effect of Alloying Additions on the Lattice Parameter of Austenite *J. Iron Steel Inst.* **208** 469–474

[47] J. Ågren 1986 A revised expression for the diffusivity of carbon in binary FeC austenite *Scr. Metall.* **20** 1507–1510

[48] G. Stechauner and E. Kozeschnik 2014 Assessment of substitutional self-diffusion along short-circuit paths in Al, Fe and Ni *Calphad Comput. Coupling Phase Diagrams Thermochem.* **47** 92–99

[49] J. Cornide, G. Miyamoto, F. G. Caballero, T. Furuhara, M. K. Miller, and C. Garcia-Mateo 2011 Distribution of dislocations in nanostructured bainite," *Solid State Phenom.* **172–174** 117–122

[50] M. Takahashi and H. K. D. H. Bhadeshia 1990 Model for transition from upper to lower bainite *Mater. Sci. Technol.* **6** 592–603

[51] H. Matsuda and H. K. D. H. Bhadeshia 2004 Kinetics of the bainite transformation *Proc. R. Soc. A Math. Phys. Eng. Sci.* **460** 1707–1722

[52] Parker S. V. 1998 Doctoral thesis University of Cambridge

[53] A. S. Podder, I. Lonardelli, A. Molinari, and H. K. D. H. Bhadeshia 2011 Thermal stability of retained austenite in bainitic steel: An in situ study *Proc. R. Soc. A Math. Phys. Eng. Sci.* **467** 3141–3156

[54] F. G. Caballero and H. K. D. H. Bhadeshia 2004 Very strong bainite *Curr. Opin. Solid State Mater. Sci.* **8** 251–257

[55] F. G. Caballero, M. K. Miller, and C. Garcia-Mateo 2011 Slow bainite: An opportunity to determine the carbon content of the bainitic ferrite during growth *Solid State Phenom.* **172–174** 111–116

[56] G. Speich 1969 Tempering of low-carbon martensite *Trans Met Soc AIME* **245** 2553–2564

[57] M. Peet, S. S. Babu, M. K. Miller, and H. K. D. H. Bhadeshia 2004 Three-dimensional atom probe analysis of carbon distribution in low-temperature bainite *Scr. Mater.* **50** 1277–1281

[58] W. Mayer, S. Sackl, Y. V. Shan, S. Primig, and E. Kozeschnik 2014 Evolution of precipitates and martensite substructure during continuous heat treatment *Mater. Today Proc.* **2** 619–622

[59] F. G. Caballero, C. Garcia-Mateo, M. J. Santofimia, M. K. Miller, and C. García de Andrés 2009

New experimental evidence on the incomplete transformation phenomenon in steel *Acta Mater.* **57** 8–17

Paper III

The tale of upper and lower bainite: A computational analysis of concurrent C-diffusion and precipitation

Philipp Retzl and Ernst Kozeschnik

Scripta Materialia

Volume 248, Year 2024, 116146

The tale of upper and lower bainite: A computational analysis of concurrent C-diffusion and precipitation

P. Retzl[a,b], E. Kozeschnik[a]

a TU Wien, Institute of Material Science and Technology, Getreidemarkt 9, 1060 Wien, Austria

b MatCalc Engineering GmbH, Gumpendorferstraße 21, 1060 Wien, Austria

Abstract

Carbon partitioning in bainite is a central mechanism controlling this transformation. Depending on whether C atoms form precipitates in the ferrite platelets or remain dissolved in a solid solution, the resulting microstructure is denoted as either lower or upper bainite. In the present analysis, a simulation study is conducted with long-range diffusion of C and simultaneous precipitation of carbides. The computational analysis suggests that carbides always form within the ferritic subunits before carbon redistribution into the surrounding austenite commences, independent of temperature. Since these carbides can rapidly dissolve again at higher bainite transformation temperatures, they are commonly not experimentally observed in upper bainite. At lower temperatures, carbide re-dissolution takes significantly more time, and carbides are, therefore, commonly identified, with the corresponding microstructure denoted as lower-bainite. Since carbides shall always form in the ferrite platelets, a classification of upper and lower bainite based on the existence of carbides should be reconsidered.

Main Body

Bainite forms by the nucleation of ferritic subunits in austenite and their subsequent growth. The subunits can nucleate either at grain boundaries or autocatalytically at other subunits. An aggregate of subunits with the same crystallographic orientation is called a sheaf. Ferritic subunits grow via a displacive mechanism, i.e., with the speed of sound after their nucleation [1]. Therefore, they are supersaturated in carbon since the solubility of carbon is much lower in ferrite than in austenite. If the excess carbon diffuses into the surrounding austenite before carbides form within the ferritic subunits, the common classification of the resulting microstructure is upper bainite. Otherwise, when carbide precipitates are observed within the ferrite, the microstructure is referred to as lower bainite [2,3]. The carbon, which is ejected by the ferritic subunits, enriches the surrounding austenite, which can then decompose into ferrite and cementite. If carbide formation in austenite is retarded by

alloying elements, such as Si or Al, carbide-free bainite is formed, in which the ferritic subunits are surrounded by austenite films [2,4].

Regardless of the assumed mechanism leading to its formation, the presently applied distinction between upper and lower bainite is mostly related to the presence of carbides in the ferritic subunits [5-9].

To predict the type of bainitic microstructure that forms at a given temperature, models have been developed that compare the time required for the decarburization of the ferritic plates with the time necessary to form a certain amount of carbides within the platelets [10,11]. These models can predict the transition temperature from upper to lower bainite in a way that achieves a reasonable agreement with the experimental data. However, there are still some discrepancies between simulation and experiment, the cause of which may lie in different aspects of the standard approach to upper and lower bainite. To define a transition temperature from upper to lower bainite (the so-called lower bainite start temperature), the assumption of a limiting carbide phase fraction in the ferritic bainite is necessary since a minimal number of carbides may always form. It seems difficult, though, to pinpoint the exact amount of cementite required to label a bainitic microstructure as lower bainite. In contrast to the models described in references [10,11], the simulation approach presented in the next section couples the C-diffusion between austenite and ferrite directly with the precipitation kinetics. This is a crucial feature, as both processes are strongly coupled and occur as competing microstructural processes.

To describe the mechanisms that govern the formation of a bainitic microstructure, a 1-D cell diffusion simulation is set up with coupled precipitation kinetics calculations. This simulation is performed with the thermokinetic software package MatCalc, version 6.04.0140 [12]. Applications of this software to precipitation kinetics simulations have been described in previous studies [13-15]. The thermodynamic database mc_fe.tdb (v2.060) and the diffusion database mc_fe.ddb (v2.012) are used. The cell-diffusion simulation utilizes a finite differences scheme to calculate transient multi-component diffusion profiles. A detailed description of this simulation aspect is reported in Refs. [16,17].

For the current modeling, it is assumed that the ferritic subunits form rapidly via a displacive transformation mechanism. Although other hypotheses concerning bainite formation exist, this mechanism seems to be the most evidenced in literature [3,6]. At the beginning of the simulation, several simulation cells corresponding to the subunit half-thickness are assigned to the ferritic phase (BCC_A2). Only a half thickness is considered in the calculations due to symmetric boundary conditions at the left end of the simulation box. The remaining cells are initially assigned to the

austenite phase (FCC_A1). The interface between the two phases remains stationary during the simulation. This method is developed and described in Ref. [17] when simulating the C-redistribution between ferrite and austenite films accompanying the bainite transformation.

The composition and assigned thermodynamic phase of a cell define the chemical potential and diffusional mobility of elements within it. Likewise, microstructural properties that affect diffusion, such as the dislocation density, are assigned according to Ref. [17]. The size of the one-dimensional diffusion simulation box is chosen between 300 and 500 nm. A single cell has a length of 1 nm in our setup, which provides a sufficient spatial resolution while sustaining feasible calculation times. This setup resembles a single isolated subunit in an austenite matrix, i.e., no constraint of carbon diffusion by neighboring subunits. The thickness of the ferritic subunits is calculated on a phenomenological basis according to Ref. [18], which was initially developed by Parker [19]. The subunit thickness, d_{b}, based on data of steels with C-contents between 0.095 and 0.5 wt% in a temperature range between 523 and 773 K, is approximated as

$$d_{\mathrm{b}} = 2 \cdot 10^{-7} \cdot \frac{T-528}{150}\ [m]. \tag{1}$$

Cementite is chosen as the carbide precipitation phase in the ferritic regions. Although a sequence of metastable carbides can form in a bainitic microstructure, this simplification is made because cementite represents the most common carbide occurring in bainite [3]. Other carbides of interest could easily be implemented into the simulation setup, however, without altering the fundamental findings of the present work. They have, therefore, been omitted for the benefit of straightforward interpretation of the results. Dislocations are selected as the nucleation site for these carbides, and a para-equilibrium approach is used to calculate the nucleus's chemical composition [20].

The dislocation density within the ferritic subunits is calculated with an empirical relation from Retzl et al. [17], which reads as

$$\rho_{\mathrm{d}} = 7 \cdot 10^{15} \cdot \frac{1}{0.28\sqrt{2\pi}} \cdot e^{-\frac{1}{2}\left(\frac{T_{\mathrm{C}}}{280}\right)^2}, \tag{2}$$

with T_{C} being the temperature in °C.

The lower the bainite transformation temperature, the more critical becomes the impact of C atoms being trapped at defects. It is essential to consider the trapping of C at dislocations since trapped C

atoms are not available for precipitation processes. For example, due to this effect, fresh martensite formed at 200 °C can dissolve up to 0.2 wt% of C in thermodynamic equilibrium [21]. The trapping of C in bainitic ferrite is experimentally confirmed by X-ray and atom probe measurements [22,23]. The effect of trapping is incorporated in the present simulations with the approach developed by Svoboda and Fischer et al. [24-26]. The main input parameters, i.e., trapping enthalpy, ΔE, and coordination number, *c*, are used with $\Delta E = 75000 - 20 \cdot T$ [J/mol] and $c = A/T^2$, with the coefficient $A = 10^6$, as suggested by Mayer et al. [27].

The model described in the former section is applied to two bainitic alloys with 0.05 wt% and 0.45 wt% C in the temperature range of 300 to 500 °C. The simulations are run for up to 3000 s. The C-concentrations are chosen because, for high temperatures and low C content, i.e., 0.05 wt%, an upper bainite structure with no carbides in the ferritic subunits can be expected, and, for low temperatures and higher C contents, a lower bainite structure with carbides in the subunits will emerge [11].

Figure 1 shows the evolution of C concentration (a) and phase fraction of carbides (b) for an alloy with 0.05 wt% C at 500 °C directly after the ferrite subunit has formed. The phase boundary between austenite and ferrite is visible in Figure 1.a in the C concentration jump at roughly 165 nm distance from the subunit center. According to the standard description in the literature, at this low C concentration, no carbides should form within the subunit since the diffusion of C into the surrounding austenite should be faster than the precipitation of carbides. However, according to our simulations, as shown in Figure 1.b, a significant amount of carbides forms rapidly after the start of the simulation (~1/1000s). During the simulation, these particles only reach a maximum diameter of 3-4 nm and completely dissolve again after approximately 0.4 s. The precipitates dissolve because the C level in the BCC (ferritic) area decreases due to C diffusion into the austenitic regions and the accompanying destabilization of the carbides. At first glance, it may seem of no great interest that very small carbides form and dissolve again within half a second, but it has a significant impact on the partitioning process of C. The time necessary for C to diffuse out of the subunit increases severely because the carbon, which is bound in the form of carbides, is not readily available for diffusion. Therefore, simple assumptions that consider the evacuation of C from the subunit and carbide precipitation as separate processes underestimate the time that it takes for the C concentration in the ferritic bainite plates to reach equilibrium.

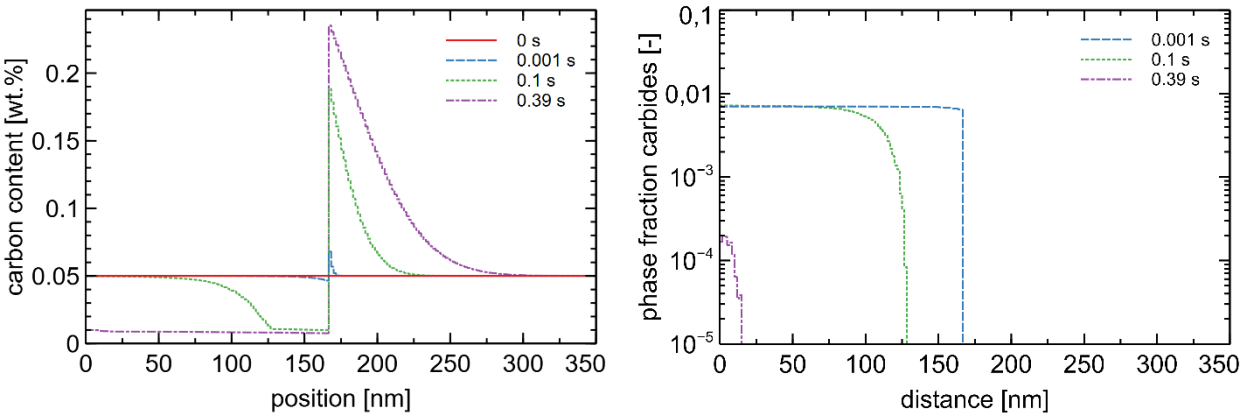

(a) (b)

Figure 1: Precipitation and long-range diffusion simulation at 500 °C with 0.05 wt% C (a) evolution of C concentration profile (b) carbide volume fraction profile

A different behavior occurs if a C content of 0.45 wt% at 300 °C is investigated. Similar to the low-C high-temperature case, carbides form rapidly in the subunit (~0.01 s until the maximum phase fraction is reached). These precipitates bind nearly all C in the ferritic region, and, in combination with the slow diffusion at 300 °C, almost no C redistribution occurs within 3000 seconds. The evolution of the C profile is shown in Figure 2.a. The carbides reach a maximum mean diameter of 12 nm, and their phase fraction stays nearly the same throughout the simulation. Only after about 3000 s, as shown in Figure 2.b, does the carbide volume fraction start to decrease at the edge of the ferrite region. When investigating bainite after 3000 s of transformation, many carbides are still present in the ferritic subunits, thus resembling the lower bainite microstructure. On prolonged aging at this temperature, the carbides will still dissolve. The lower bainite microstructure is thus, in principle, the same as upper bainite. However, it is looked at before sufficient time has passed to dissolve the carbides again and let the C atoms diffuse into the austenite films and blocks.

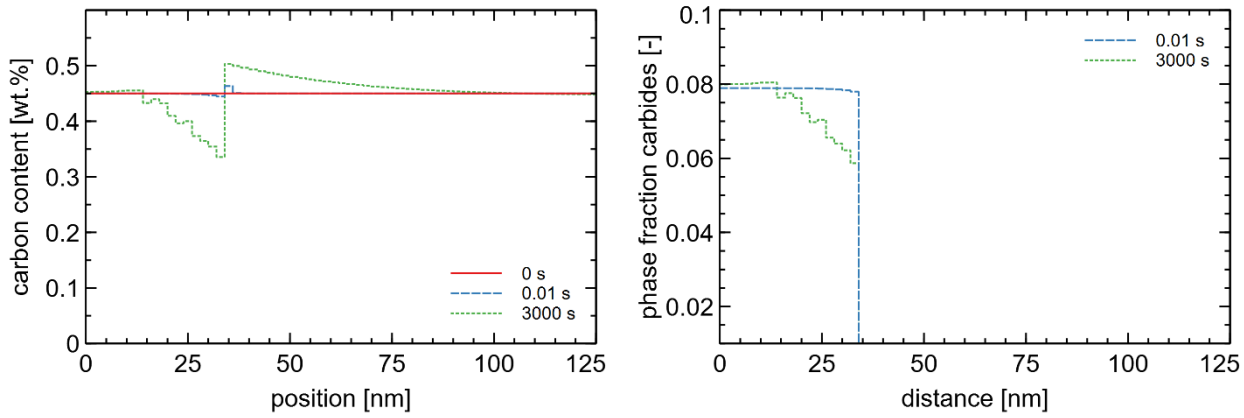

(a) (b)

Figure 2: Simulation at 300 °C with 0,45 C (a) evolution of C concentration profile (b) carbide volume fraction profile

Since carbides always precipitate during the simulation and a dissolution process takes place in all environments examined, it is essential to know how long this process takes to understand the

implications for the microstructure evolution of bainite. Figure 3 shows the necessary time for the carbide phase fraction to reach a maximum and be reduced to zero for different temperatures and the two investigated C contents. While, for the low C content (0.05 wt%), even at 300 °C, the dissolution process takes place within 200 s, for the higher C content (0.45 wt%), nearly no carbides have dissolved even after 3000 s. Since the bainite transformation process takes some hundreds of seconds at conventional production conditions [28], the commonly and practically observed microstructure under these conditions will generally be denoted as lower bainite.

In essence, our simulations suggest that upper and lower bainite share the same formation processes. Subunits always go through the stages of C supersaturation, carbide formation within the subunit, carbon partitioning to the surrounding austenite, and, given enough time, dissolution of the carbides within the subunit. It only takes fractions of a second for low-C alloys at high temperatures to go through this process but several thousand seconds for the high-C and low-temperatures cases. Depending on when an observer looks at the microstructure, either upper or lower bainite is diagnosed.

Observing the rapid formation and dissolution process of carbides at higher temperatures is rather challenging due to the short time and small size scale. However, the dissolution of carbides in a high-C low-temperature case could be observed if the bainite is tempered for much longer than necessary for complete transformation. The onset of this dissolution process would manifest itself in the formation of carbide-free zones at the border of a subunit, according to Figure 2.b. Experimental evidence for the formation of carbide-free zones in subunits has been reported in Ref. [29]. These carbide-free zones are found in subunits located at the border of sheaves. This corresponds to our simulation setup of a single subunit surrounded only by austenite and no other subunits close to it.

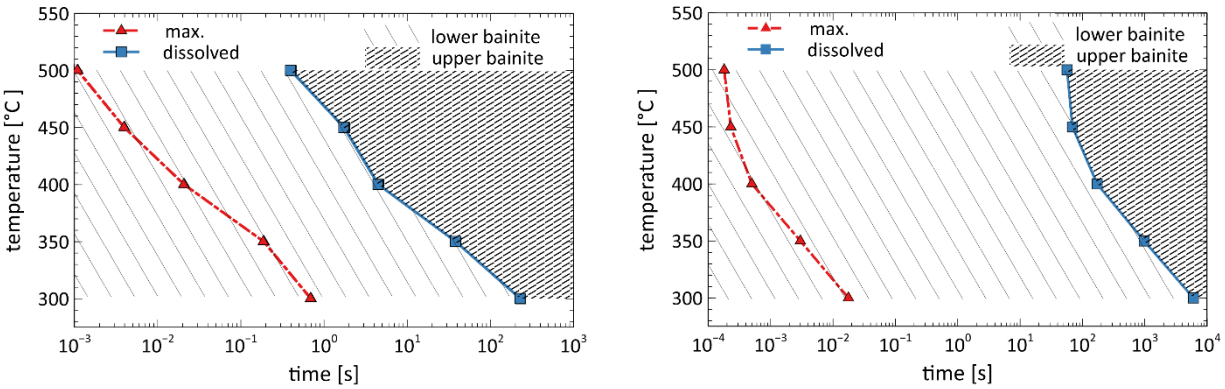

Figure 3: Simulation results of the presented model. Time until maximum phase fraction of carbides is formed within the ferritic bainite subunits (red triangles) and time until all carbides are dissolved (blue squares) as a function of temperature for C content of 0.05 wt%(a) and 0,45 wt% (b). Differently, shaded areas indicate if upper or lower bainite will be observed.

A model capable of simultaneously describing the long-range diffusion of C and the precipitation of carbides within and around a bainite subunit is used to study the redistribution of C and the concurrent precipitation of carbides in bainitic microstructures. The simulations show that, even at low C concentrations and high temperatures, where the final microstructure is commonly denominated as upper bainite, carbide precipitates form within a subunit shortly after its formation. These carbides dissolve again rapidly, however, due to C diffusion into the surrounding austenite. Since the analysis demonstrates that carbide precipitation always occurs, the denomination of the observed microstructure apparently depends on the particular moment when the microstructure is looked at and, in particular, whether the carbides have had sufficient time to dissolve again. With this in mind, the classification of upper and lower bainite solely based on the presence or absence of carbides should be reconsidered.

References

[1] H.K.D.H. Bhadeshia, D. V. Edmonds, Mechanism of Bainite Formation in Steels., Acta Metall. 28 (1980) 1265–1273.

[2] M. Takahashi, H.K.D.H. Bhadeshia, Model for transition from upper to lower bainite, Mater. Sci. Technol. 6 (1990) 592–603.

[3] H.K.D.H. Bhadeshia, BAINITE IN STEELS, 3rd ed., 2015.

[4] L.C. Chang, Microstructures and reaction kinetics of bainite transformation in Si-rich steels , Mater. Sci. Eng. A 368 (2004) 175–182.

[5] G. Spanos, H.S. Fang, H.I. Aaronson, A mechanism for the formation of lower bainite, Metall. Trans. A 21 (1990) 1381–1390.

[6] L.C.D. Fielding, The Bainite Controversy, Mater. Sci. Technol. 29 (2013) 383–399.

[7] F.G. Caballero, M.K. Miller, C. Garcia-Mateo, Influence of transformation temperature on carbide precipitation sequence during lower bainite formation, Mater. Chem. Phys. 146 (2014) 50–57.

[8] S.A. Sajjadi, S.M. Zebarjad, Isothermal transformation of austenite to bainite in high carbon steels, J. Mater. Process. Technol. 189 (2007) 107–113.

[9] H. Ohtani, S. Okaguchi, Y. Fujishiro, Y. Ohmori, Morphology and properties of low-carbon bainite, Metall. Trans. A 21 (1990) 877–888.

[10] M. Azuma, N. Fujita, M. Takahashi, T. Lung, Modelling upper and lower bainite trasformation in steels, Mater. Sci. Forum 45 (2003) 221–228.

[11] L. Guo, H. Roelofs, M.I. Lembke, H.K.D.H. Bhadeshia, Modelling of transition from upper to lower bainite in multi-component system, Mater. Sci. Technol. (United Kingdom) 33 (2017) 430–437.

[12] E. Kozeschnik, Mean-Field Microstructure Kinetics Modeling, Encycl. Mater. Met. Alloy. 4 (2021) 521–526.

[13] R. Radis, E. Kozeschnik, Numerical simulation of NbC precipitation in microalloyed steel, Model. Simul. Mater. Sci. Eng. 20 (2012).

[14] S. Zamberger, M. Pudar, K. Spiradek-Hahn, M. Reischl, E. Kozeschnik, Numerical simulation of the evolution of primary and secondary Nb(CN), Ti(CN) and AlN in Nb-microalloyed steel during continuous casting, Int. J. Mater. Res. 103 (2012) 680–687.

[15] S. Zamberger, L. Whitmore, S. Krisam, T. Wojcik, E. Kozeschnik, Experimental and computational study of cementite precipitation in tempered martensite, Model. Simul. Mater. Sci. Eng. 23 (2015).

[16] Y. V. Shan, M. Soliman, H. Palkowski, E. Kozeschnik, Modeling of Bake Hardening Kinetics and Carbon Redistribution in Dual-Phase Steels, Steel Res. Int. 92 (2021).

[17] P. Retzl, S. Zamberger, E. Kozeschnik, Computational analysis of austenite film thickness and C-redistribution in carbide-free bainite, Mater. Res. Express 8 (2021).

[18] H. Matsuda, H.K.D.H. Bhadeshia, Kinetics of the bainite transformation, Proc. R. Soc. A Math. Phys. Eng. Sci. 460 (2004) 1707–1722.

[19] S.V. Parker, Modelling of Phase Transformations in Hot-Rolled Steels, Doctoral Thesis

University of Cambridge (1998)

[20] E. Kozeschnik, H.K.D.H. Bhadeshia, Influence of silicon on cementite precipitation in steels, Mater. Sci. Technol. 24 (2008) 343–347.

[21] G. Speich, Tempering of low-carbon martensite, Trans Met Soc AIME 245 (1969) 2553–2564.

[22] F.G. Caballero, H.K.D.H. Bhadeshia, Very strong bainite, Curr. Opin. Solid State Mater. Sci. 8 (2004) 251–257.

[23] M. Peet, S.S. Babu, M.K. Miller, H.K.D.H. Bhadeshia, Three-dimensional atom probe analysis of carbon distribution in low-temperature bainite, Scr. Mater. 50 (2004) 1277–1281.

[24] J. Svoboda, Y. V. Shan, E. Kozeschnik, F.D. Fischer, Determination of depths of traps for interstitials from thermodynamic data: A new view on carbon trapping and diffusion, Model. Simul. Mater. Sci. Eng. 21 (2013) 065012.

[25] J. Svoboda, F.D. Fischer, Modelling for hydrogen diffusion in metals with traps revisited, Acta Mater. 60 (2012) 1211–1220.

[26] F.D. Fischer, J. Svoboda, E. Kozeschnik, Interstitial diffusion in systems with multiple sorts of traps, Model. Simul. Mater. Sci. Eng. 21 (2013) 025008.

[27] W. Mayer, S. Sackl, Y. V. Shan, S. Primig, E. Kozeschnik, Evolution of precipitates and martensite substructure during continuous heat treatment, Mater. Today Proc. 2 (2014) S619–S622.

[28] D. Quidort, Y.J.M. Brechet, A Model of Isothermal and Non Isothermal Transformation, ISIJ Int. 42 (2002) 1010–1017.

[29] T. Klein, C. Hofer, M. Lukas, T. Wojcik, R. Schnitzer, M. Galler, G. Ressel, Formation of “carbide-free zones” resulting from the interplay of C redistribution and carbide precipitation during bainitic transformation, Materialia 7 (2019) 100380.